Doctoral Dissertation
Doctoral Program in Electrical, Electronics and Communications Engineering
(31^{st} cycle)

DSP-based RF waveform aggregation for next generation mobile fronthauling

Befekadu Debebe Mengesha

* * * * * *

Supervisors
Prof. Roberto Gaudino
Prof. Vittorio Curri

Politecnico di Torino
2019

I hereby declare that, the contents and organization of this dissertation constitute my own original work and does not compromise in any way the rights of third parties, including those relating to the security of personal data.

. . . . . .

Befekadu Debebe Mengesha

Turin, 2019

Summary

The exponential traffic increase demands faster, high capacity, and quality of service (QoS) guaranteed services. Cloud radio access network (C-RAN) has become an emerging enabling technology introduced into 5G networks, and proposed to support the upcoming next generation mobile technologies and provide high spectral efficiency and low energy consumption with a reduced capital expenditure and operational expenditure. Nevertheless, the current C-RAN imposes stringent requirements on the fronthaul link for seamless connectivity. Digital radio over fiber (D-RoF) based on common public radio interface (CPRI) is the most widely used means of distributing baseband samples in C-RAN fronthaul. However, the signal transmission of quantized IQ (In phase and quadrature) via CPRI requires very high aggregated bit rate on the optical link and flexibility limitation. Therefore, these make them impractical to be realized for massive MIMO, millimeter wave (mm-wave) and 5G applications.

Analogue radio over fiber (A-RoF) is currently being studied for mitigation of the huge bandwidth provisioning of D-RoF based on CPRI. It is a technique of aggregating massive amount of native radio waveforms through a more traditional analogue radio over fiber approach. In this Thesis, the numerical analysis, simulation and experimental demonstration of A-RoF on intensity modulated and direct detected (IM-DD) is studied based on a novel frequency division multiple access (FDMA) and time division multiple access (TDMA) digital signal processing (DSP) radio waveform aggregation techniques. These alternatives aims to transport in parallel many fourth generation long term evolution (4G LTE) or fifth generation new radio (5G NR) waveforms on the same fiber.

The transport of up to 96 20-MHz LTE waveforms is experimentally demonstrated over IM-DD optical link based on off-line DSP aggregation using FDMA and TDMA approaches. Furthermore, a simulative analysis of 5G NR uplink IM-DD optical channels with scalable bandwidth is performed, exploiting a numerical model implemented in MATLAB and considering both aggregation techniques FDMA and TDMA.

Finally, the bottom-line physical layer performance of two approaches is investigated. Particularly, which of the two gives the lowest error vector magnitude(EVM), better spectral efficiency (since bandwidth become the bottleneck in 4G and 5G

systems) and less DSP complexity for a given set of aggregated waveforms on the same optoelectronic transceiver.

Acknowledgements

First and foremost, i would like to express my sincere gratitude to my supervisor Prof. Roberto Gaudino and Prof. Vittorio Curri for their kind support and guidance throughout my PhD study and research. Indeed, i really appreciate their patience and immense knowledge contributing towards the successful completion of my degree.

I would also like to acknowledge Dr. Pablo-torres Ferrera Post-Doc researcher in our OPTCOM group for his consistence support on the research discussion and guidance that counts a lot to achieve my PhD degree.

I would also like to thank Stefano Dr. Straullu senior researcher at Instituto Superiore Mario Boella (ISMB) for his prestigious contribution in taking care of the experimental activities and procedure that helped me a lot to reach the conclusion of the doctorate program.

Lastly, i would like to thank my family : my grandmother, my brothers, my relatives and my friends, for understanding me and your sacrifice in waiting me those years until i accomplish my degree.

I would like to exclusively dedicate this PhD to the memory of my ***mother***

Contents

List of Tables

List of Figures

Nomenclature

Acronyms / Abbreviations

A-RoF Analog RoF

AC Antenna Carrier

ADC Analog-to-Digital Converter

APD Avalanche PhotoDetector

ASE Amplified Spontaneous Emission

AWG Arrayed WaveGuide

AWGN Additive White Gaussian Noise

BBU BaseBand Unit

BCH Broadcast Channel

BER Bit Error Ratio

BS Base Station

C-RAN Cloud Radio Access Network

CAPEX CAPital EXpenditure

CD Chromatic Dispersion

CO Central Office

CoMP Coordinated Multi-Point

CP Cyclic Prefix

CPRI Common Public Radio Interface

CQI Channel Quality Indicator

CSI Channel State Information

CW Constant Wave

D-RoF Digital Radio over Fiber

D-SCH Downlink Shared Channel

DAC Digital-to-Analog Converter

DAS Distributed Antenna System

DC Data-Center

DCI Data Control Information

DD Direct Detection

DFB Distributed-FeedBack laser

DFT Discrete Fourier Transform

DSP Digital Signal Processing

DU Digital Unit

E/O Electrical to Optical

EAM Electro-Absorption Modulator

ECL External Cavity Laser

EDFA Erbium Doped Fiber Amplifier

eNodeB evolved Node B

ER Extinction Ratio

ETSI European Telecommunication Standard

EVM Error Vector Magnitude

FBG Fiber Bragg Grating

FDD Frequency Division Duplexing

FDMA Frequency Division Multiplexing Access

FEC Forward Error Correction

FFT Fast Fourier Transform

FIR Finite Impulse Response

FPR Free Propagation Region

FR Frequency Range

gNodeB Next-generation Node B

IF Intermidiate Frequency

IFFT Inverse FFT

IM Intensity Modulation

IMT International Mobile Telecommunication

IoT Internet of Things

IQ Inphase and Quadrature

ITU International Telecommunications Unioun

LAN Local Area Network

LDPC Low Density Parity Check Matrix

LMS Least Mean Squares

LTE Long Term Evolution

MAC Media Access Control

MIMO Multiple Input-Multiple Output

MuX MultipleXer

MZM Mach-Zehnder Modulator

NF Noise Figure

NR New Radio

O & M Operation and Mantainance

O/E Optical to Electrical

OBPF Optical Band-Pass Filter

OBSAI Open Base Stations Architecture Initiative

ODN Optical Distribution Network

OFDM Orthogonal Frequency Division Multiplexing

OPEX OPerational EXpenditure

ORI Open Radio Equipment Interface

OSNR Optical Signal-to-Noise Ratio

OTN Optical Transmission Network

PAPR Peak-to-Average Power Ratio

PBCH Pysical BCH

PD Photodiode

PDCCH Pysical Downlink Control Channel

PDF Probability Density Function

PDSCH Pysical Downlink Shared Channel

PHY Pysical layer

PIN Positive Intrinsic Negative

PON Passive Optical Network

PRACH Pysical Random Access Channel

PRB Pysical Resource Block

PUCCH Pysical Uplink Control Channel

PUSCH Pysical Uplink Shared Channel

QAM Quadrature Amplitude Modulation

QPSK Quadrature Phase Shift Keying

RAT Radio Access Technology

RF Radio Frequency

RIN Relative Intensity Noise

RLC Radio Link Control

RRH Remote Radio Head

RS Reference Signal

RTT Round Trip Time

RX Receiver

SC-FDMA Single Carrier FDMA

SDR Software Defined Radio

SFP Small Form-factor Pluggable transceiver

SMF Single-Mode Fiber

SNR Signal-to-Noise Ratio

SOI Silicon On Insulator

SR Signaling Request

TCO Total Cost of Ownership

TDMA Time Division Multiplexing Access

TTI Transmission Time Interval

TX Transmitter

UCI Uplink Conrtol Information

UE User Equipment

UTRA Universal Terrestrial Radio Access

VOA Variable Optical Attenuator

WDM Wavelength Division Multiplexing

Chapter 1

Fronthaul in Cloud-Radio Access Network(C-RAN)

1.1 Introduction

Centralized (Cloud) Radio Access Network (C-RAN) is an emerging enabling technology proposed for the first time in[67] to mitigate the potential challenges in the future next generation radio access technologies. In C-RAN architecture, the radio heads and the BS (Base Station) are geographically separated: Remote Radio Heads (RRHs) left at the antenna site and the Baseband Unit (BBU) processing is left at the central office. RRH is the radio frequency(RF) wireless transceiver circuitry which provides functionalities such as digital-to-analog conversion (DAC), analog-to-digital conversion (ADC), frequency up / down conversion at a distributed antenna location. In addition it provides also operation and management (O&M) processing and standardized fiber optics fronthaul interface that connects to the base station located at central station [63]. In C-RAN applications optical fiber is used as a fronthaul medium due to its large bandwidth, lower attenuation loss and less transmission delay. Hence most part of antenna sites will be connected by fiber. In BBU pool or centralization BBUs of different base stations are co-located in the same central office. Software defined radio (SDR) further enables all baseband processing based on an open Information Technology (IT) architecture [98]. C-RAN architecture has a potential to minimize the operation expenditure (OPEX) associated with simpler management and operation in addition reduced energy and power consumption as compared to the tradition RAN architecture. However, C-RAN has many challenges to be faced such as availability of low-cost transport service, deployment techniques on BBU co-operation, interconnection and clustering, efficient BBU visualization techniques and the development of reliable fronthaul network with required capacity and strict delay requirement. In the following subsection we survey the state-of-the-art literature on C-RAN architecture and the next generation fronthaul technologies.

1.2 C-RAN architecture

Mobile network has been considered as the most important component in radio access network (RAN), since the radio interface technology determines the service area coverage, the data rate and the capacity of the cellular network. Moreover, base stations (BSs) which are the main component of RAN, usually represent the largest monetary investment associated with mobile networks. The total cost of ownership (TCO) in mobile networks consists of CAPital EXpenditure (CAPEX) and Operating EXpenditure (OPEX). CAPEX refers to those expenses associated with feasibility study of the network site construction, baseband and RF equipments purchase and installation, software, system test and integration costs. While OPEX is intended for the overall operational cost of the network such as operation and maintenances, electricity and power consumption and extension cost. The growing demand in the mobile data traffic requires a considerable enhancement in the mobile network architectures and advanced cellular technologies. In the following the evolution of radio access network architecture and the concept of C-RAN for next generation mobile network is presented.

Traditional access network

In traditional wireless architecture, the base station (BS) is located close (couple of meters) to antenna tower and radio head (RH). The digital unit (DU) or baseband Unit (BBU) and the radio unit (RU) are integrated inside a base station. The BS functions such as interface with RU, baseband signal processing, control and management of BS are implemented by BBU. Furthermore, functions like power amplification, frequency filtering and conversion, analog-to-digital converter (ADC), digital-to-analog converter (DAC), RF modulation/demodulation and interface with BBU are managed by the RU. When the RU is connected to antenna by using coaxial cable feeder, power loss can become a significant impairment. Moreover, such kind of configuration requires large equipment footprints and development cost [14]. Links only exists between the base station and its access gateway, and there is no link between base stations. Therefore, BS can serve only those RF channels dedicated in the its physical cell, where the hardware resources can not be re allocated to handle varied instant communication throughput needs in different cells. This architecture was implemented mainly in 1G, 2G and 3G mobile network [23].

Distributed BS with RRH architecture

Distributed BS with a remote radio heads (RRH) architecture is an enhancement of traditional BS station system devised to efficiently manage the evolving complexity network standards. Unlike the traditional architecture, physically splits distributed BS and RRH [76]. The RRH consists of functional blocks which serves

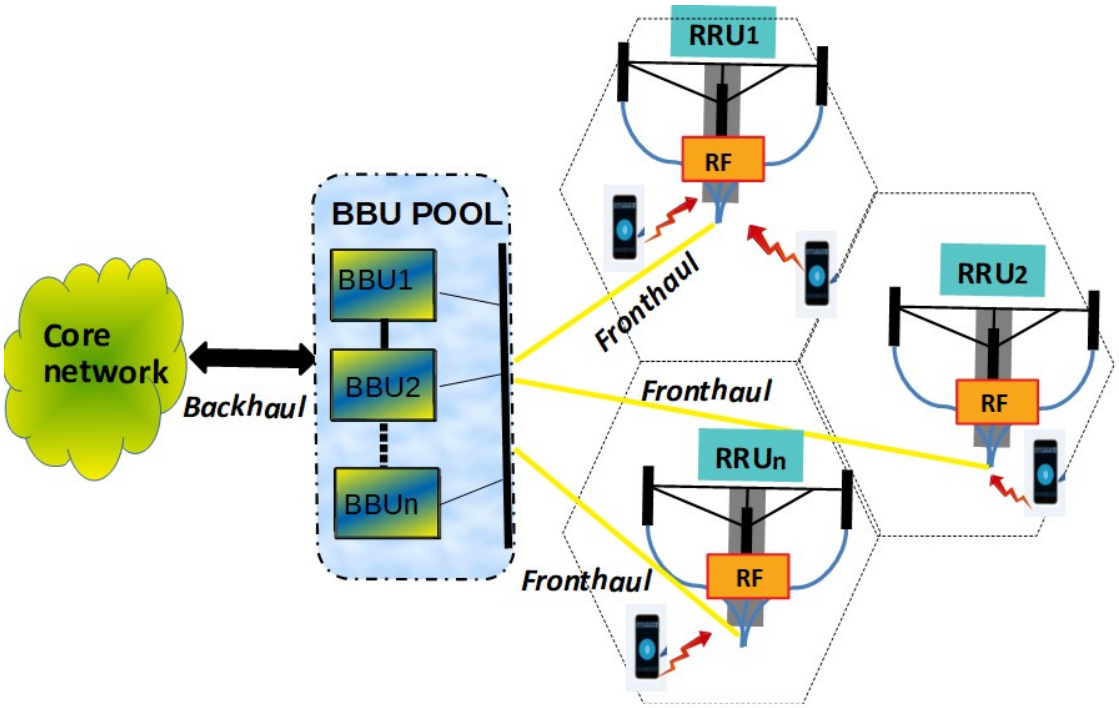

Figure 1.1: C-RAN architecture.

as analog RF power amplifier, diplexer, ADC/DAC, digital predistortion, sampling rate converter (SRC), digital upconversion (DUC), digital down conversion (DDU) and optical interface [62]. Due to its compactness in size, RRH can be mounted on the antenna tower. The BBU handles digital signal processing. The detail of BBU functions are elaborated in [31, Chapter 16]. The BBU is connected to the dedicated RRH by means of radio-over-fiber technology. The fiber span length can be tens of kilometers, which is constrained due to low round trip time delay. Hence BBU can be placed in desired convenient location and consumes less power.

C-RAN architecture

C-RAN advocates the separation of RRH from the centralized BBU pool that lead to the functional split between the two components. Fig. 1.1 shows a C-RAN architecture where unlike in Distributed BS with RRH architecture that RRHs are connected to their distributed BS, many RRHs are linked to Virtual BBU pool (cluster) in a centralized location through low latency and high bandwidth optical fiber links [23]. The backhaul then connects the high performance processor BBU pool which is capable of handling a large number of BBUs with mobile core networks.

In C-RAN, heavy and lightly loaded cellular networks can share the BBU cluster in optimized and efficient way. Moreover, Clustering enhances network coordination and management allowing to implement inter-cell interference cancellation that arises from coordinated multiple point (CoMP) transmission and reception from multiple BSs as well as massive Multiple-input and multiple-output (MIMO) technologies. Researches and efforts are undergoing by mobile network operators on how the spectral efficiency and performance can consequently increases , system coverage and capacity to enhance next-generation mobile network performance. It is expected that cloud computing embedded in wireless RAN can offer high spectral efficiency and network performance [14]. The letter C in C-RAN is interpreted in the traditional literature of this field as Cloud, Centralized processing, Cooperative radio, Collaborative or Clean. When C-RAN was proposed for the fist time by International Business Machines Corporation (IBM) [67], it was devised to support the drives described on the next subsection.

1.2.1 C-RAN rationale

C-RAN gains a great attraction towards mobile network operators due to its potentials that may enhance mobile communication system in different ways.

A first motive come from its prospective to lower the initial investment cost and reduction of time to market. In this application scenario, C-RAN is regarded as resource pool that can handle various kinds of wireless access networks. If an operator plans to build new access network, it can lease the required resources from other cloud service provider.

A second motive is related to centralized RAN as a site engineering solution especially on a rural area with difficulty to access the terrain and dense urban areas with increased roll out difficulties. As a matter of fact, the BBU is shifted to a central office and only RRHs mounted on RF antenna with simple power supply is left on a remote cell site. Therefore with such reduced footprint, C-RAN reduces the installation and maintenance cost. Furthermore, upgrading of radio access technology on the existing cell is realizable [86].

A third motive is linked to C-RAN adaptability to dynamic traffic. Due to the fact that mobile traffic is changing during day and night time in different areas. For instance, load on the base stations located close to residential area is low during day time, while the traffic load located to industrial area is heavy. In each cellular network the daily traffic distribution varies and the peak of the traffic occurs in different hours [84]. Due to the fact that the base band processing of different cell is carried out in a centralize BBU pool, the utilization of computational resource can be increased significantly.

A fourth motive drives from radio performance, and it is related to implement collaboration of multiple BS in the physical layer signal processing, that is expected to provide higher capacity and improved cell performance [1]. Moreover, the very

low latency between BBUs enables better performance in mobility [51].

A fifth motive arises from security point of view, in the conventional LTE deployment the backhaul is secured by IP platforms that adds some potential overheads such as Internet protocol security (IPsec). Indeed, in C-RAN the BBU is located in secured location, therefore IPsec is no more required .

Even though C-RAN demonstrate such advantages it bring up also some stakes which are mainly due to the fronthaul interface.

1.3 Fronthaul interface

Fronthaul interface is the crucial network element in C-RAN architecture that connects RRHs and BBU pool based on radio-over-fiber (RoF) concept and it is also the main focus of the Thesis. RoF is a well established technique for next-generation wireless transmission which integrates the advantages of both fiber and wireless networks. Besides C-RAN, it is also widely used in the distributed antenna system (DAS) that is a structure with high density of distributed antennas. Each antenna is equipped with a transceiver capable of converting radio frequency (RF) to intermediate frequency (IF) signals. The received IF signal is then is connected to the BBU through optical fiber fronthaul interface [111]. RoF techniques are used to connect central office (CO) containing BBUs with many RRHs providing low latency and high capacity coverage in short range communication systems [103]. Two categories of mobile fronthaul approaches are digitized-RoF (D-RoF) and analog-RoF (A-RoF).

1.3.1 Digitized-RoF

D-RoF is a technique for transmitting radio signals, using digitized RF/IF band subcarriers or digitized IQ baseband signals over fiber optic link. The basic architecture for transmitting digitized In-phase and quadrature (IQ) baseband bit stream is shown in Fig. 1.2 . It is assumed that the left side of the fiber optics link is processed in a centralized BBU location and the right part is located in the RRH unit. The connection between central office containing BBUs with many RRHs is normally realized by DRoF interface in which the signal is transmitted over short range fiber optics to provide low latency and high capacity system coverage. Moreover, when the advent of cooperative multi-point (CoMP) transmission and reception that can enhance the average spectral efficiency and consistency of performance at cell edge, centralized processing with RRH is realized by D-RoF links via optical fiber [34].

The system is basically composed of digital IQ modulator and demodulator, fiber optics link, a pair of optical transceiver, DAC, ADC, IQ to RF and RF to IQ converters, and reference frequency. Signal transmission in downlink direction that is from BBU towards RRH is explained as follows: the digital IQ modulator

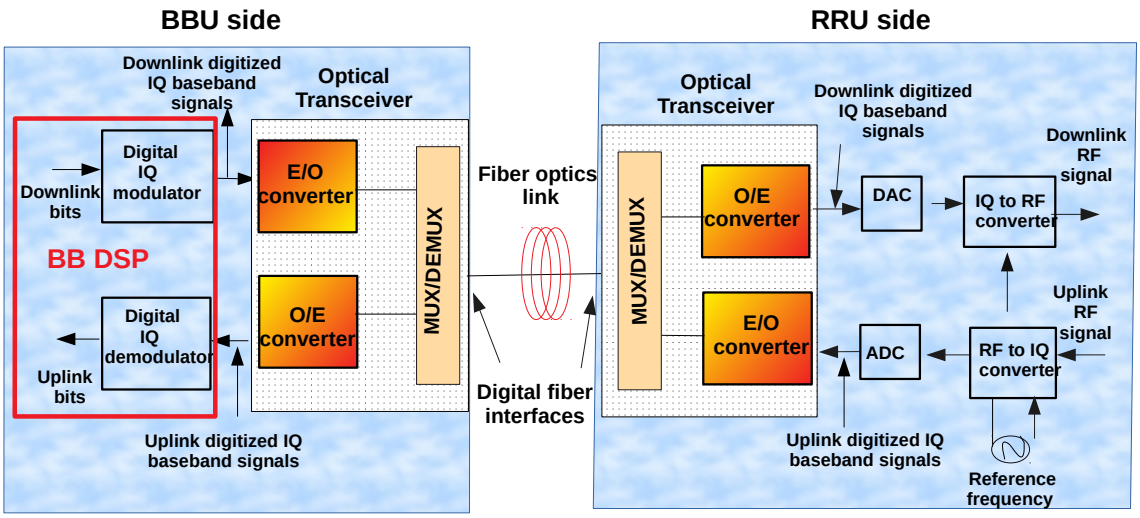

Figure 1.2: Digitized radio-over-fiber transmission.

generates digitized IQ baseband signals from the input downlink (payload) IQ data bits . The IQ baseband signal (digital stream of bits) is then modulates an optical carrier using electrical to optical (E/O) converter and multiplexed inside the optical transceiver. The generated baseband D-RoF signals are transmitted through fiber optics link. At the remote end, the received downlink D-RoF signals are demultiplexed and optically detected using optical to electrical (O/E) converter inside the optical transceiver. Digital-to-analog converter (DAC) converts the detected electrical signal to the desired analog baseband signal that is then up-converted in frequency by IQ to RF converter. The desired RF frequency is tuned by the reference frequency generator that is provided from central office and delivered to the antenna site. The signal transmission in the reverse uplink direction is explained as follows. The received RF uplink signal is down-converted in frequency by using RF to IQ converter and the desired frequency is tuned by reference frequency generator. The characteristics of the reference should be designed to satisfy with the frequency stability of the downlink RF signal. So that both direction of RF signal transmission are repeated through fiber optic link. The digitized IQ baseband signal is generated by the analog-to-digital converter (ADC) that is then used to modulate the optical carrier using an other E/O converter and multiplexed via fiber optics link. At the BBU end, the received uplink D-RoF signal is optically detected using O/E converter. The detected electrical signal is then digitally demodulated with the digital IQ demodulator that is used to recover the uplink payload data [100].

Radio equipment manufactures defined protocols for D-RoF for the transport of fronthaul traffic such as Common Public Radio Interface (CPRI) [28], Open Base Stations Architecture Initiative (OBSAI) [81] and Open Radio Equipment Interfaces(ORI) [82] as we shortly describes in the following subsections.

CPRI

Common Public Radio Interface (CPRI) is a radio interface protocol widely used for IQ data transmission. It is also used for the transmission of Control Word (CW) which are embedded for the control and management (C&M) of equipments. CPRI specifies the interface between BBU and RRH using physical (L1) and data link layer (L2) protocols in serial line transmission mode at Constant Bit Rate (CBR) data over a dedicated physical channel usually optical fiber based on Small Form Pluggable (SFP) connectivity [79], defining a frame that contains IQ samples resulting of radio signal transmission, synchronization information and CW for control and management information. CPRI supports a number of radio standards such as Third Generation Partnership Projects (3GPP), Universal Terrestrial Radio Access (UTRA) Frequency Division Duplex (FDD), Worldwide interoperability for Microwave Access (WiMax), 3GPP Global system for Mobile communication(GSM), 3GPP Evolved UTRA and 3GPP Long Term Evolution (LTE).

In most practical deployment CPRI is configured as a point to point link, the specification also allows different topology configurations like star, chain, tree, ring, and multiple hops [79]. In spite of its efficient mapping method, CPRI is by the most widely adopted specification by radio access network vendors. However, some parts are left vendors proprietary, therefore interoperability between vendors is not guaranteed.

OBSAI

Open Base Stations Architecture Initiative (OBSAI) is a radio interface protocol in DRoF fronthaul. It is a joint venture industry based initiative of BS vendors, modules and component manufacturers. The specification which defines internal BS modules allows the interoperability and system modularity. It also specifies the interface communication link between modules. Unlike CPRI based on serial line transmission, OBSAI is packet based interface. Furthermore, four protocol layers such as physical, data link, transport and application layer are supported in the specification. The specification also covers the area of Transport, Clock/Control, Radio and Baseband interface as well as conformance test. When OBSAI is first established in 2002, its aim was to create an open market for cellular BSs where the costs and developmental efforts related to manufacturing new BS products is substantially reduced [86], [1].

ORI

Open Radio Interface (ORI) is an Industry Specification Group (ISG) initiative latest radio interface protocol defined by European Telecommunication Standard Institute (ETSI) aimed at developing an interface interoperability between elements of BSs in a cellular mobile network equipment of multiple equipment vendors and

network operators. In order to reach the full interoperability, ORI interface is built on CPRI by rearranging some options [86].

Features common to CPRI, OBSAI and ORI

Even though there are some differences in the implementation of D-RoF fronthaul interfaces, they have common aspects such as :

- The most commonly deployed fronthaul physical layer is optical fiber link
- Small form pluggable (SFP) is commonly used fronthaul interface connector, that has a high flexibility in the choice of transceiver. Moreover, the fronthaul performance requirement is achieved by adopting SFP.
- The data rate imposed by the fronthaul interface is constant bit rate in both uplink and downlink directions

Since CPRI is by far the most widely deployed protocol by RAN vendors, the following subsection discuss about network requirements taking CPRI as a reference.

CPRI requirements and design features

Radio Access Technology (RAT) configuration

CPRI supports several RAT in different bands based on the specific cell site configuration. For instance macro cell design generally can have three to six sectors. For each sector different RAT can be present such as 2G, 3G at 1800 MHz and/or 2100 MHz bands and 4G LTE at 800 MHz and/or 2600 MHz for uplink and downlink direction in FDD.

Data Rate

CPRI is a constant bit-rate serial transmission where its line bit rate ranges from 614.4 Mbps (option 1) up to 24.33024 Gbps (option 10). For line bit rate options 1,2,3,4,5,6 and 7 the line coding of 8B/10B shall be used as per the IEEE 802.3 [15] clause 36, specified for physical layer serial data transmission. For bit rate option 7A, 8, 9 and 10 the line coding 64B/66B shall be used according to IEEE 802.3 [15], clause 36, specified for physical layer serial data transmission [28]. The CPRI data rate can be expressed [82] from Eq. 1.1

$$Data\_rate_{CPRI} = N_{AC} \times f_s \times M \times 2 \times Cw \times C \tag{1.1}$$

where N_{AC} is the number of antenna carriers per sector, f_s is the sampling rate used in digitization of samples for each of the in-phase (I) and quadrature-phase(Q) streams, M is the sample width (bits/samples), 2 is the multiplication factor of I and Q data, Cw represents an overhead due to CPRI control

word and C is the coding factor (10/8 for line coding 8B/10B or 66/64 for line coding 64B/66B). For example a transport of $8X8$ MIMO for one sector $20MHz$ LTE macro cell for line option 7 requires a CPRI data rate of $9.8304Gbps$ as shown in Eq. 1.2

$$Data\_rate_{CPRI} = 8 \times 30.72Mbps \times 15 \times 2 \times \frac{16}{15} \times \frac{10}{8} = 9.8304Gbps \quad (1.2)$$

Or (for coding gain 66/64)

$$Data\_rate_{CPRI} = 8 \times 30.72Mbps \times 15 \times 2 \times \frac{16}{15} \times \frac{66}{64} = 8.1101Gbps \quad (1.3)$$

Latency

The latency calculation dedicated to fronthaul is not defined by RAN standards because this network segment is included inside an implementation dependent evolved NodeB(eNb) which is a logical node handling transmission/reception in many cells commonly not always correspond to base station. Latency of RAN requirement has consider the round trip time (RTT) between BBU and RRH physical level, the propagation time of the transmission in the fronthaul, the signal processing time in the optical equipments, downlink/uplink (DL/UL) air propagation delay. In CPRI specifies different constraint on delay and jitter. For instance regardless of the delay caused by cable length, round-trip time of user plane data (IQ data) over CPRi/OBRI/ORI link shall not exceed $5\mu s$ with accuracy of round-trip latency on each link of hop should satisfy $\pm 16.276ns$[50][28].

Synchronization and jitter

CPRI requires strict synchronization and timing accuracy between BBU and RRHs. The clock information is provided to BBU either by Global Positioning System (GPS) or from the core network via the backhaul link. The central reference frequency generated in RRH shown in Fig. 1.2 shall be synchronized to the bit clock of the receiver CPRI signal from the DU. Accordingly, if some jitter (delay) alter the CPRI signal it could affect the precession of the central frequency generation [32]. The frequency accuracy requirement on the air interface for the case of FDD LTE is ±50 ppb (parts per billion) [2]. The requirement in CPRI specification is defined with the contribution of ±2 ppb of the total ±50 ppb of the fronthaul link. Furthermore, CPRI also specifies the maximum tolerated random, deterministic and sinusoidal jitter both at BBU transmitter for downlink direction and RRH receiver in downlink and vice versa. Such limit corresponds to Bit Error Ratio (BER) equal to 10^{-12} [28], [32].

Table 1.1: Modulation format Vs EVM peformance requirement for LTE

Modulation Formats	EVM %
256-QAM	3.5
64-QAM	8
16-QAM	12.5
QPSK	17.5

Data Rate Performance

Apart from bandwidth, the main requirements for CPRI transmission are BER and latency. According to CPRI specification, the maximum allowed BER on the fronthaul link should be 10^{-12}. Moreover, Error Vector Magnitude (EVM) is the most commonly used parameter for evaluating the quality of the physical radio link at the RRH output. From global point of view, the fronthaul segment should not degrade the radio performance that is typically quantified in terms of EVM. The EVM is defined as the difference between the ideal transmitted symbols vector (S_{Tx}) and the decoded (measured) symbols (S_{Rx}) after equalization in a complex plane. Moreover, it is defined by the root mean square of error(err) for a number of (L) transmitted symbols taking into consideration all (linear and nonlinear) impairments [91], according to the following expression.

$$EVMrms = \frac{err}{\mid S_{Tx,m} \mid}, err^2 = \frac{1}{L}\sum_{n=1}^{L} \mid S_{Rx,n} - S_{Tx,n} \mid^2 \tag{1.4}$$

The power of the longest ideal constellation $|S_{Tx,m}|$ can be used for normalization purpose that is dependent on the M symbols vector of specific modulation formats. For instance, 3GPP specifies the relation between the modulation format to be adopted and the corresponding link quality in terms of $EVMrms$ for LTE technology [2] as shown in Table 1.1.

Dimensioning CPRI Fronthaul

In this subsection a general guideline for dimensioning CPRI fronthaul interface is outlined. CPRI defines a logical connection between BBU and RRH with classification of user plane data, control and management and synchronization as shown in Fig. 1.3.

User plane data : The user information is carried in the form of IQ data flow. Each data flow represents the radio signal of one carrier which is digitized and sample at one antenna carrier (AxC).

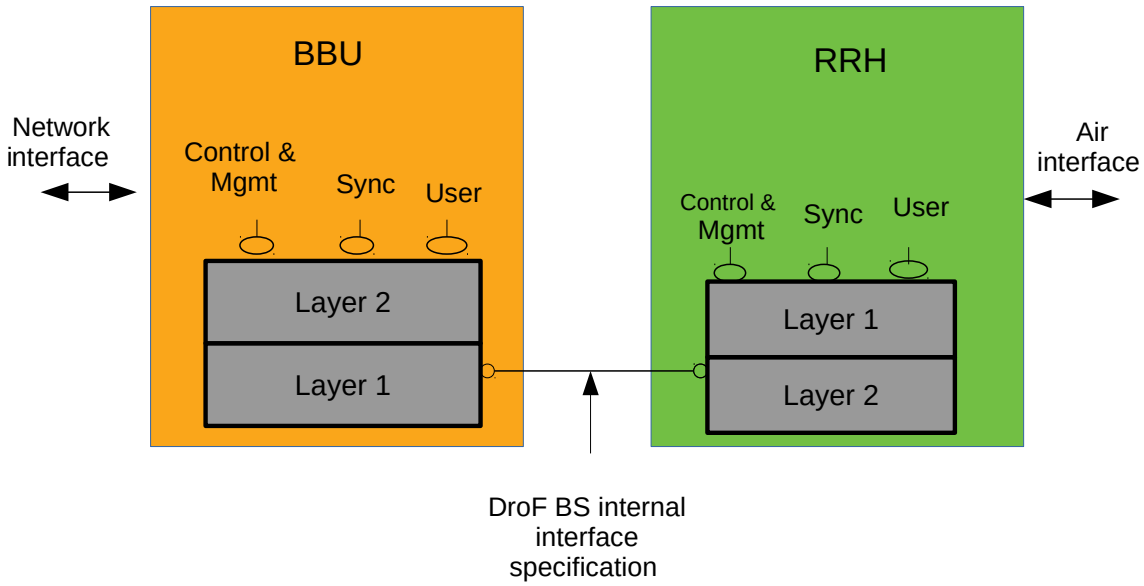

Figure 1.3: CPRI interface specification.

Control and Management : Control & Management data is transmitted in a control words (CW) by an in-band protocol. That is used in synchronization, timing and error detection/correction based on the line coding specified in[15] (line code 8B/10B and 64B/66B)[79].

Synchronization (Sync) : The synchronization data is used for time and frame alignment. The CPRI interface shall enable the RRH to obtain the frequency accuracy specified in [2]. The central frequency generation in the RRH shall be synchronized to the bit clock of the line coding ports which connects the BBU to the RRH. In order to allow efficient and simple synchronization and frequency generation, the bit clock interface shall be a multiple of 3.84 MHz. All CPRI line bit rates have been chosen in such a way that the basic Universal Mobile Telecommunication System (UMTS) chip rate of 3.84 Mbit/s can be recovered in a cost-efficient way from the line bit rate taking into account the line coding scheme mentioned on Table 1.2. For example, the 1228.8 Mbit/s correspond to an encoder rate of 122.88 MHz for the 8B/10B encoder and a subsequent frequency division by a factor of 32 provides the basic UMTS chip rate.

The length of a basic frame in CPRI protocol is $Tc = 1/3.84MHz = 260.41667ns$. A basic frame consists of 16 words with index $W = 0...15$. The length (T) bits of each of the words is depends on the CPRI line option as shown in 1.2. Out of 16 words, the first word $W = 0$ is used for one control word. The remaining words $W = 1...15$, 15/16 are dedicated to IQ data transport[28].

Taking into consideration LTE scenario. The transport capacity (the number of AxCs) of different bandwidth LTE signal can be obtained from Eq. 1.1 and CPRI line options. For instance the bit rate per AxC of 20MHz LTE is obtained as 1.2288

Table 1.2: CPRI dimensioning on LTE

Option	CPRI bit rate(mbps)	line coding	T (bit)	2.5MHz LTE bandwidth	20MHz LTE bandwidth
1	614.4	8B/10B	8	4	-
2	1228.8	8B/10B	16	8	1
3	2457.6	8B/10B	32	16	2
4	3072	8B/10B	40	20	2
5	4915.2	8B/10B	64	32	4
6	6144	8B/10B	80	40	5
7	9830.4	8B/10B	128	64	8
7A	8110.08	64B/66B	128	64	8
8	1037.6	64B/66B	160	80	10
9	12165.12	64B/66B	192	96	12
10	2433.02	64B/66B	384	192	24

Gbps from Eq. 1.2, and the option 7 CPRI line bit rate is specified in [28] to be 9.8304 *Gbps*. Therefore 20 MHz LTE on option 7 CPRI can support up to 5 AxCs. The transport capacity for LTE bandwidths of 2.5MHz and 20MHz is outlined in Table 1.2.

CPRI challenges towards next-generation mobile networks

Utmost extensive researches and studies are undergoing to meet the International Mobile Telecommunication (IMT)-2020 and beyond recommendation vision usually indicated as 5G[52]. Which recommends that by the year 2020, the mobile and wireless traffic volume is expected to reach up to 1000 times higher mobile data volume per area, and a 10-100 times higher typical data rate per user device, than in 2010[75]. Since CPRI needs very high bandwidth and strict latency, such 5G requirement are challenging to be implemented on the conventional CPRI interface at lower cost and complexity. However, recent studies such as a new digital interface that can replace the conventional CPRI interface by using delta sigma modulation for digital fronthaul[104], mobile fronthal architecture based on functional split and time division (TDM) multiplexing [112] and novel DSP based CPRI compatible waveform aggregation techniques which is the main target of this Thesis are being carried out extensively. Thus the huge bandwidth demand and strict latency requirement is the biggest challenge of the conventional CPRI implementation in the next generation (5G) mobile fronthaul.

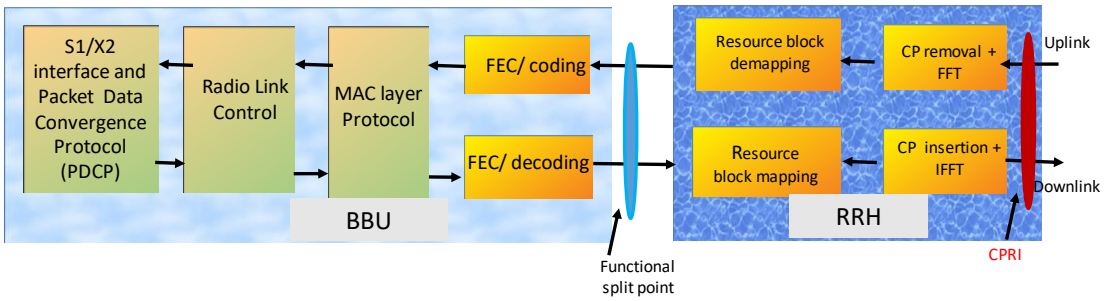

Figure 1.4: Physical layer functional split.

1.3.2 Physical Layer functional split

The conventional CPRI interface is claimed as weighted function split, due to the fact that most of the physical layer and the data link protocol functions are centralized at BBU and minimal signal processing is left at the RRH site. Though this architecture provides such advantages mentioned in section C-RAN rationale, it suffers from huge bandwidth requirement for radio access technologies like LTE and 5G NR networks with massive MIMO techniques. The fronthaul interface must provide constant data rate that is independent of the actual wireless data[112]. This is due to the fact that 15 bits are required per IQ sample thus the IQ data transmission can be as much as 30 times more than the actual data throughput[112]. For instance the transmission of LTE $20MHz$ with sample rate $30.72MSample/s$ requires a CPRI data rate of $122.88MSample/s$ for $8B/10B$ encoder. Even if the wireless data traffic is not fully loaded, RRU needs to always upload to the BBU at a peak rate [33].

The Physical layer functional split is one of the architectural options proposed to relax the huge bandwidth requirement of CPRI protocol. Fig. 1.4 shows the physical layer functional split scheme where the entire Media Access Control (MAC) layer protocol, radio link control (RLC), X2 interface a protocol allowing to interconnect eNodeBs with each other [7], S1 interface responsible to connect eNodeB with core networks [8], packet data convergent protocol (PDCP) and some physical layer functions like FEC are implemented inside the centralized BBU. Where as PHY layer functions such as resource mapping/demapping, cyclic prefix (CP) insertion/removal and IFFT/FFT are handled in RRH[87]. The fronthaul bandwidth requirement using physical layer functional split scheme significantly reduce the bandwidth requirement due to the minimized quantization resolution. In addition, it increases the transmission efficiency since the resource mapping transmits only loaded wireless resource blocks (RBs).

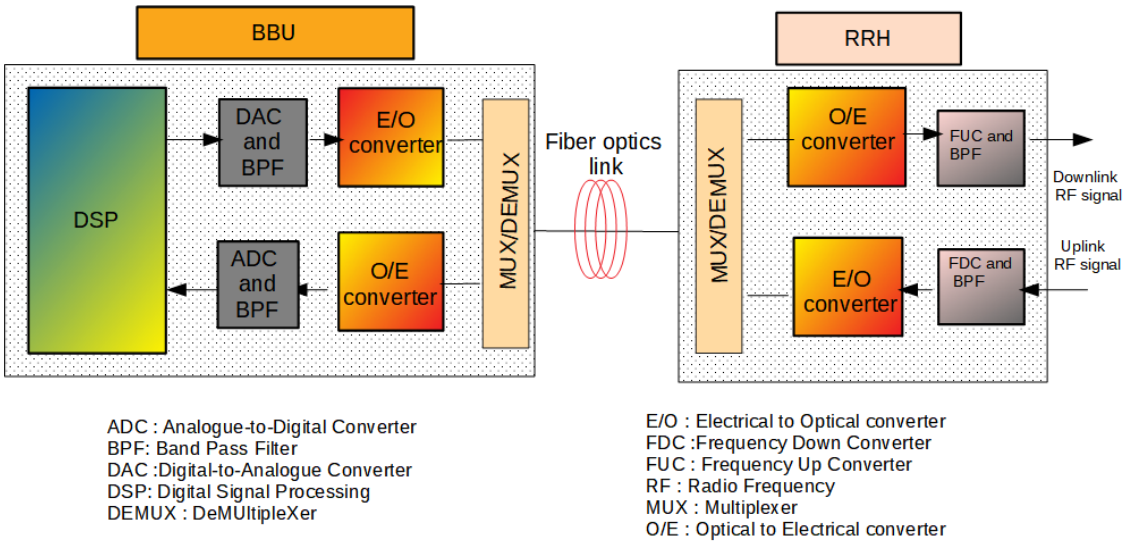

Figure 1.5: DSP assisted A-RoF architecture.

1.3.3 Analog-RoF

A-RoF is a technique used for transporting native radio waveforms over fiber optic link that is proposed to mitigated the massive bandwidth requirement of Digitized-RoF in the next generation mobile fronthaul application. The basic blocks of DSP assisted A-RoF architecture used in bidirectional link transmission is shown in Fig.1.5. The BBU that resides at central location is composed of powerful digital signal processing (DSP) engine capable of computing resource block mapping/demapping, modulation/demodulation, aggregation/deaggregation, channel estimation and pre-compensation of waveforms such as LTE and 5G for both uplink and downlink transmission direction. On downlink transmission from BBU to RRH, DAC converts the digital sequence from DSP output to analog and the unwanted out of band signal is filtered out by using BPF. The filtered analog signal is used to modulate the optical carrier using E/O converter blocks and then transmitted via fiber optics link towards the RRHs. The RRH at the remote site that is left with minimum bare tasks, is equipped with O/E converter which is used to detected the received optical carrier to electrical signal, frequency up converter (FUC) to up convert the intermediate frequency electrical signal (IF) into downlink RF signal. In the reverse uplink transmission, frequency down converter (FDC) is used to down convert the uplink RF input signal to IF which is then modulated in optical carrier using another O/E converter. The optically modulated signal is transported via fiber optic link. At the BBU side, the received optical signal is converted back to electrical in O/E converter. ADC is used to convert the detected analog signal into digital which is then processed in the DSP block [34].

The transport solution based on analog optics maximize the bandwidth efficiency and allows inexpensive mature analog RF hardware at RRH.

Unlike D-RoF, the bandwidth required for the fronthaul interface depends on the wireless radio signal in use. Since A-RoF based network deployment can be integrated on a typical 10 *Gbps* fiber transceiver, it is considered as a promising candidate for the next generation mobile fronthaul [87]. Recently, many experimental researches reveal that efficient bandwidth utilization is realized by using A-RoF optical transmission based on Intensity Modulation and Direct Detection (IM-DD) scheme. However, this ARoF solution is prone to noise and distortion cased by non-linearities as well it is less tolerance against fiber transmission impairments both at transmitter and receiver. Therefore the dynamic range of the link is reduced with the fiber span length[16].

The main target of this Thesis is to demonstrate that bandwidth efficient transmission using DSP assisted RF waveforms like LTE and 5G NR aggregation on IM-DD based A-RoF fronthaul link.

1.4 Further fronthaul solutions for C-RAN

In conventional C-RAN, the fronthaul links between BBU and RRH are usually based on huge bandwidth optical fiber. However, this architecture is not well suited for the majority of small cell deployments both in terms of cost and resource allocation.The available medias such as coax cables, twisted pair telephone line and power lines that provide copper-based home access can be employed as an alternative solution for fronthaul links. This solutions allows to optimize the fiber deployment only in the areas where it is effectively required or depending on the provided service to the subscriber[14].

Indoor Radio over Copper Fronthaul

Radio over Copper (RoC) is an alternative technology for the conventional fronthauling that is convenient for self-powered indoor deployment. This is due to the fact that it is supports the pre-existing LAN cables, which are currently deployed in buildings and enterprises, hence it highly reduces the cost of deploying a new infrastructure. The current researches reveals that LAN cables are capable of carrying high Gbps of air-link data rate supporting a massive number of antennas at each remote antenna unit (RAU). This is because of the fact that four twisted pairs bounded together to provide 1 GHz bandwidth over 100m [71].

Since, RAU are self-powered over the same LAN indoor building solutions based on LAN cables are suitable candidates to satisfy the huge traffic demand of the upcoming 5G networks. Furthermore, the infrastructural cost of RoC deployment is very low (already exiting cable) as compared to very high cost of D-RoF and A-RoF deployment that requires optical infrastructure.

Fronthaul Transport for Virtualized Small Cells

Small Cell Forum (SCF) has defined a MAC/PHY based split architecture, an approaches that divides the BS into MAC and PHY layer functions based on networked Functional Application Platform Interface (nAFPI), that allows to enable the fronthaul interface associated with the virtualized small cells to be transported over packet switched networks.

The fronthaul interface that connects the remote small cell radio transceivers at the physical network function to the higher layer virtualized small cell function in the virtual network function. Virtualization enables flexibility to dynamically locate the deployment of virtual network function. The recent study of SCF[60]functional splits demonstrated the analysis virtual network function/fronthaul termination on different location. For instance, for urban deployment scenario it can be on a macro cell sites, metro network data center, operator data center, metro service provider, regional data center and operator's edge service provider. From the transport perspective nFAPI impact the latency requirements associated with the fronthaul network. Where the exact fronthaul latency budget is linked with the usage of Hybrid-Automatic Repeat Request (HARQ) interleaving. In addition, it can be relaxed by using larger number of autonomous HARQ re-transmission.

1.5 Optical fronthaul solutions for C-RAN

A variety of optical network technologies can be implemented for the interconnection of centralized BBU pool and RRHs located at different antenna sites, referred as a fronthaul network. Widely deployed optical solutions that are employed in C-RAN architecture are :

Dedicated/Dark fiber

It is an independent fiber link from BBU directed towards a dedicated RRH. This kind of implementation usually occurs when an operator has a large installed fiber. It is an appropriate solution where it is more cost-effective to install fiber than to deploy an optical transport element at remote cell site[14]. It has an advantage of providing low latency and simple deployment. However, due to the fact that a point-to-point connection has to established between BBU and RRU, it requires the use of high fiber resources. Moreover, its applicability is limited for low cost infrastructure because the cost associated with the deployment of new fiber is relatively high. When base station density is increased in the 5G stage, fiber resources will be insufficient and can not provide high reliability for the ultra-reliable and low-latency communication (URLLC) services.

Optical Transport Network and Wavelength Multiplexing (OTN/WDM)

OTN/WDM assumes the time multiplexing of several users on a single wavelength having integrated WDM (sending several dense wavelengths simultaneously) interface on the same system chassis as the switching functionality. This allows the convergence of the WDM and OTN transmission functionality into a single system and has a benefit of eliminating any need for short reach interconnections between separate WDM and OTN, hence saves fiber resources [36]. The main drawback of this architecture is that the equipment cost is relatively high and not feasible for low cost application [35].

Passive Optical Network (PON)- WDM

PON-WDM solution allows transmission of multiple channels over a single fiber by using passive optical multiplexer/demultiplex known as Arrayed Wavelength Grating (AWG) which enhances the fiber capacity[47]. The advantages associated with this technology are fiber resource sharing, low cost and footprints. However it suffers from high accumulated insertion loss that limits the transmission distance. Furthermore, since passive equipments does not support Operation and Maintenance (OAM), fault isolation is difficult. Even if the latency caused by optical component is very small, the RRU and BBU must provide colored optical interface which adds the cost of wireless equipment. In this thesis we implemented passive WDM optical fronthaul solution for the realization of A-RoF based on IM-DD technique[14].

Since new fiber infrastructure is required in all the above optical solutions, the deployment cost of this solutions are very high with respect to the already existing twisted pair solutions in a low data rate application.

1.6 Thesis structure

The Thesis mainly focuses on the study of an alternative fronthaul solution, that is A-RoF fronthaul with DSP based radio waveform aggregation techniques, carrying out a performance comparison among two aggregation options. The analysis of this architecture solutions was carried out by first developing a physical layer system simulation carried out in the Photonext Inter-Departmental Center. The rest of the Chapters are organized as follows

Chapter 2 initially presents Intensity Modulation and Direct Detection (IM-DD) architecture used in the implementation of A-RoF based fronthaul. Furthermore, it describes the operating principle and characteristics of the optoelectronic devices used on transmitter, optical channel and receiver sides. Then it gives clear insight for the experimental demonstration which will be explained in Chapter 6. Chapter 3 reviews the physical channel generation of 4G LTE and 5G NR (new radio) waveforms for both uplink and downlink based on a multicarrier access transmission with orthogonal frequency division multiplexing (OFDM). Moreover, this chapter

discuses the theoretical derivation of signal processing steps used in the implementation of physical channel generation procedures. Chapter 4 presents the detail of the novel DSP based waveform aggregation techniques implemented on transmitter and receiver sides, which is the core part of the Thesis. The chapter outlines in depth the signal evolution of RF waveform such as 4G LTE and 5G waveforms (outlined in Chapter 4) aggregation based on frequency division multiplexing access(FDMA) and time division access (TDMA) techniques. Chapter 5 drives the optical path performance requirements and discusses the experimental procedures to demonstrate the transport of up to 96 LTE waveforms on IM-DD optical setup. Chapter 7 draws the conclusions of the thesis.

Chapter 2

Intensity-Modulated Direct-Detection (IM-DD) analog optical link

2.1 Motivation

Analogue Radio-over-Fiber (A-RoF) fronthaul solution appears to be an efficient candidate for next generation C-RAN architecture, where the transport of native 4G LTE and 5G NR waveforms can be achieved while fulfilling the bandwidth and latency requirements of C-RAN application. Moreover, it can be integrated on the existing legacy passive optical networks (PON) infrastructure that was developed and widely deployed to support wire-line users[107]. A-RoF based on Intensity Modulation and Direct Detection (IM-DD) technique is a prominent solution for short reach optical links with wavelength division multiplexing (WDM) /next generation passive optical networks NG-PON2 technologies[46]. This Chapter focus on describing the operating principles and characteristics of low cost optical devices used in IM-DD system as shown in Fig. 2.1. The basic IM-DD link consists of transmitter side, optical channel and receiver side. The transmitter side is considered as BBU and the receiver side as RRH for the downlink transmission, where the details of each units is described in the following Section.

2.2 Transmitter side

The role of the optical transmitter is to generate the optical signal, impose the information carrying signal, and launch the modulated signal into an optical fiber. The transmitter side of the IM-DD link is shown in Fig. 2.1 and analyzed both theoretical and experimentally in this Section. It is composed of continuous

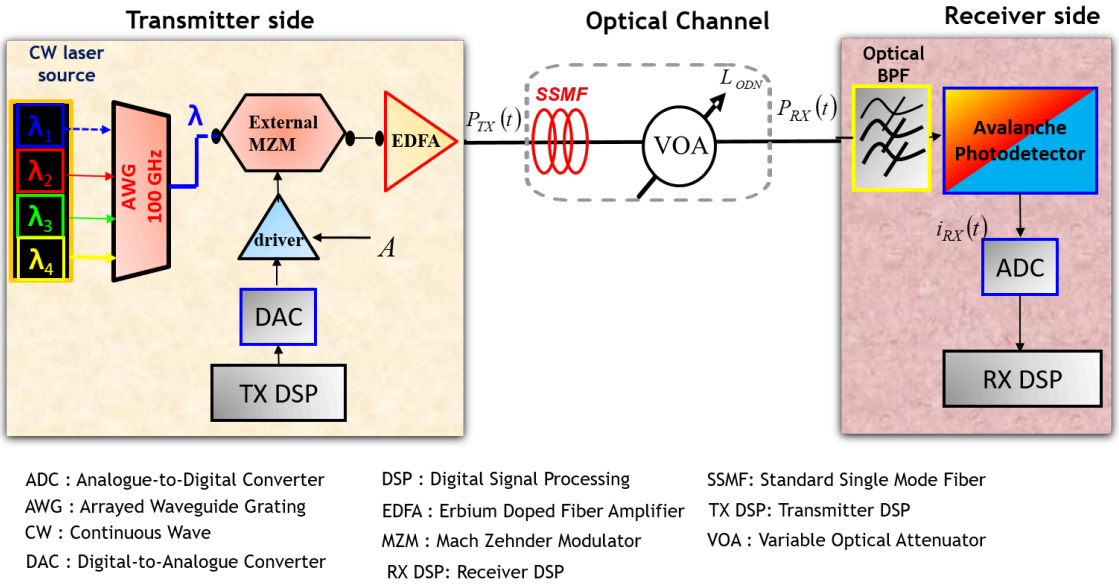

Figure 2.1: IM-DD architecture

wave (CW) lasers capable of emitting at different wavelengths, arrayed wavegude Grating (AWG) as a Wavelength Division Multiplexer (WDM) which is a passive optical device used to multiplex different channels on a single fiber, external Mach Zehnder Modulator (MZM) as an external modulator that is used to modulate radio frequency (RF) electrical signal in optical carriers, Erbium-doped fiber amplifier (EDFA) is used to amplify optical signal power, driver amplifier is an electronic component that is used to drive an electrical signal to the RF input of MZM. General overview of the optoelectronic components used at the transmitter side is described in the following Sections.

2.2.1 Semiconductor laser source

Light generation process occurs in certain semiconductor materials due to a recombination of electron and hole in p-n junction under direct biasing. Depending on the nature of recombination process, semiconductor light sources are classified as light emitting diodes (LED) in which spontaneous recombination dominates[106] and laser where stimulated emission of radiation is a dominating mechanism [94, Chapter 3]. Lasers are characterized by coherent light emission in which a beam of photons are identical in frequency and in phase. Thus the emitted light is characterized by narrow line width, high power, faster and high modulation width. Lasers used in optical communication systems are tunable over a narrow range and different semiconductor materials are used to emit laser at a central wavelength around

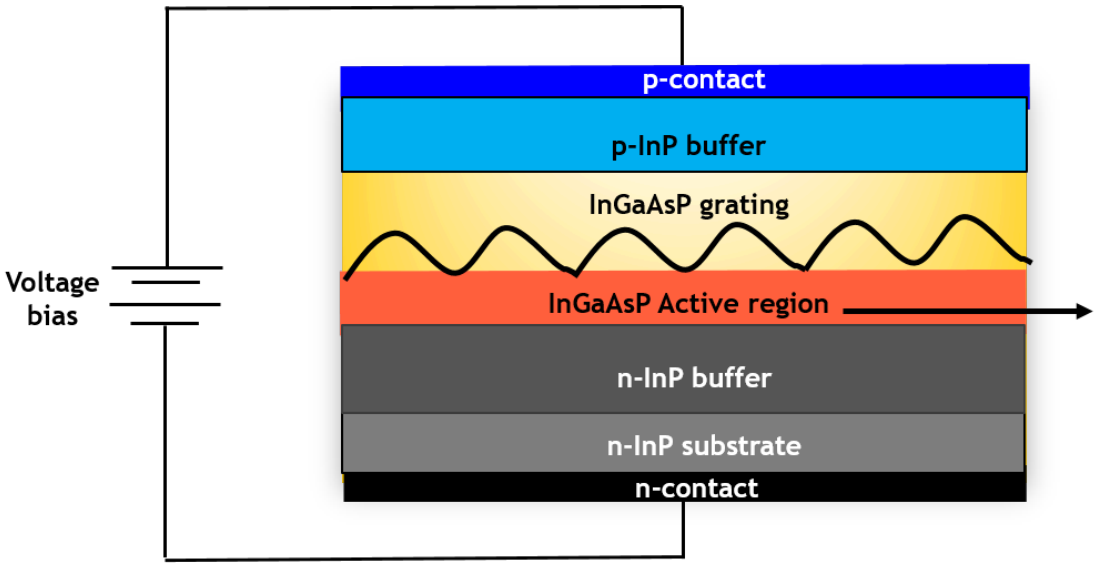

Figure 2.2: DFB laser structure.

of 680 nm, 800 nm, 1300 nm, 1500 nm [106]. The three types of semiconductor lasers used in optical communication systems are distributed feedback (DFB), extended cavity laser (ECL) and vertical cavity surface emitting laser (VCSEL). DFB semiconductor laser used in the implementation of IM-DD is described in the following Section.

Distributed Feedback (DFB) Laser

Distributed feedback (DFB) lasers are widely used laser sources in advanced optical communication systems for telecommunication applications. DFB are basically light emitting diodes with a resonator cavity that is formed either on the surface of the diode. In DFB laser shown Fig.2.2, the lasing feedback (reflection) is distributed along the laser cavity by diffraction on grating which consists of a periodic variation of refractive index. The period of the grating determins the lasing wavelength with in the gain spectrum of the active material. For this type of laser sources, the appropriate active material is made with quaternary compound such as InGaAsP and the non-active zones are made with binary compound like InP [13]. High performance such as narrow line width below 1 MHz, low threshold currents as low as 5 mA, output power as high as 100 mW, very low relative intensity noise (RIN) below -150 dB/Hz and high modulation bandwidths (3 dB bandwidths about 20 GHz) have been demonstrated for telecommunication application at 1.3 μm and 1.55 μm wavelength by using properly optimized InP based DFB lasers [24],[37][20].

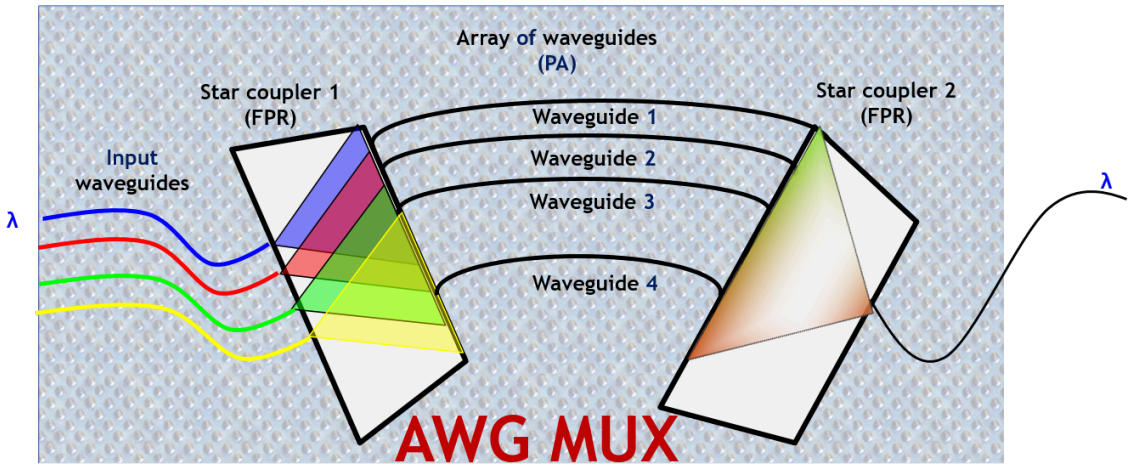

Figure 2.3: Basic AWG Multiplexer layout.

2.2.2 Arrayed Waveguide Grating (AWG)

Arrayed Waveguide Gratings (AWG) are key passive optical components in WDM networks that works on the principles of interferometry, a technique in which waves are superimposed causing the phenomenon of interference in order to extract the desired information. AWG multiplexers/demultiplexers are planar devices that are based on array of wave guides with both imaging and dispersive properties. AWG can be used as multiplexer (MUX) in dense WDM network to multiplex various WDM channels into one fiber or de-multiplexer at the receiver end of dense WDM network. Fig.2.3 shows the basic layout of AWG as a multiplexer, it consists of input/output waveguides where usually the number of waveguides indicates the number of transmitting channels. The waveguides in the phased array(PA) are spaced at regular intervals with a constant path length increment from one to the other and join the star couplers or free-propagation regions (FPR) at each end. The operating principle of AWG configured as multiplexer shown in Fig 2.3 is described as follows, the waves from the laser source having different wavelengths arrive at the input aperture of star coupler 1 and pass though FPR. At the output of FPR, the waves are coupled into the waveguide array and propagates through the individual waveguides having different optical path length towards the input aperture of the star couple 2. The phase delay proportional to the wavelength is introduced to the waves on each wave guides of different path length. The divergent beam to the input of the second star coupler is transformed into convergent one with the same amplitude and phase distribution. By using single optical fiber, multiple signals (channels) having different wavelength are taken as output[102, Chapter 4]. For AWG to be used as a de-multiplexer, the reverse operation mentioned for multiplexer will take place.

Table 2.1: Brief overview of state of the art AWG.

AWG device technology	Number of channels [#]	Channel spacings [GHz]	Bend radius [μm]
SoI [40]	11	1	6
SoI [26]	40	100	400
SoS [27]	512	25	85
SoS [57]	64	100	-
InP [96]	100	10	500

The most commonly used technologies for the implementation of today's AWG are silica-on-silicon (SoS) and Indium phosphide (InP)-based semiconductor technology. Moreover, Silcon on Insulator (SoI), polymer based and lithium niobate waveguides are also reported as well. SoS AWG currently holds the largest AWG market. It is relatively simpler to couple them with fiber, this is because the modal field of SoS matches with that of the fiber. Thus they have high fiber-coupling efficiency (losses in order of 0.1 dB) and low propagation loss. However, they are relatively larger. InP-based AWGs are attractive due to their compactness in size and potential for monolithic integration with active components such as semiconductor optical amplifier, and high speed electro-optic modulators. However, due to higher propagation loss, index contrast and the smaller waveguide dimensions it is more challenging to realize narrow channel spacing in InP-based AWGs than SoS. The state of the art of AWG are briefly reviewed in table 2.1

In the experimental part of this Thesis the AWG used for the realization of IM-DD system shown in Fig. 2.3 is based on SoS technology with 64 channels and 100 GHz spacing.

2.2.3 Optical modulator

The optical signal (beam) generated by the semiconductor laser source has to be modulated by the information signal before being transmitted over optical fiber. Intensity modulation can be achieved by using direct modulation or external modulation schemes. Direct modulation can be realized by directly modulating the bias current of the semiconductor laser where light is emitted when a high power level is transmitted and ideally no emission of light when a low (zero) power level is transmitted. The emitted light intensity is directly proportional to injected bias current only after the threshold current of the laser diode. Direct modulation can be done even at higher speed (up to 40 Gb/s in some laser) [94]. Even though it is conceptually simple and cheaper, it shows poor performance in terms of spectral occupancy, high relative intensity noise (RIN) and frequency chirp. Due to these

limitations direct modulation is not suitable for advanced telecommunication application. However it is widely used in low cost systems and local area networks. For transmitter operating at 10 Gb/s and above, external modulators are used to impose the information signal to be transmitted. The two most commonly used external modulators are Electro-Absorption Modulator (EAM) and Mach-Zehnder Modulator (MZM).

EAM are made of semiconductor materials that are characterized by changing the amount of light absorbed with applied electric field. EAM are built based on the principle of Franz-Keldysh on bulk conventional semiconductor and Quantum Confined Stark Effect (QCSE) on quantum well devices.

Mach-Zehnder Modulator (MZM)

Lithium Niobate Mach-Zehnder Modulator (LN-MZM) have been widely used for high speed and narrow band optical networks for radio-over-fiber (RoF) systems [65]. The schematic layout of MZM used in this Thesis is shown in Fig 2.4. The MZM is fabricated by embedding separate planar optical waveguides in Lithium Niobade electro-optical substrate. By using splitter, the optical input signal is split in the two arms of the waveguides. Without external voltage applied on the electrodes, the optical waves that propagate through the two arms are in phase and combined to give maximum intensity at the output of the MZM [80]. However, due to electro-optic effect of Lithium Niobate, the refractive index changes with applying external voltage via an electrode (electric field) and therefore the effective refractive index of the waveguides can be modified. Consequently, phase difference is induced between the optical waves propagating on the MZM arms. A recombination of the two different waves with a relative phase difference could create an interference that varies from constructive to destructive which rely on the relative phase shift. Hence optical signal can then be modulated in terms of intensity. If the relative phase difference is π, there is a total destructive interference which results a minimum intensity output. The drive voltage that gives phase difference of π is denoted as V_π.

The transfer function of LN MZM is shown by Eq.2.2. where the overall electric field from the RF time varying modulating signal $V_{in}(t)$ and V_{DC} is given by

$$V(t) = V_{in}(t) + V_{DC}. \tag{2.1}$$

The off driving voltage of the MZM is denoted by V_{off}, α determines the insertion loss at the input of the MZM and the extinction ratio (ER) is the power ratio of the MZM at maximum operating point and power at the off driving voltage and expressed in dB.

$$\frac{E_o(t)}{E_i(t)} = \frac{1}{\sqrt{\alpha}}\left\{ \sin\left[\frac{\pi}{2}\left(\frac{V(t)-V_{off}}{V_\pi}\right)\right] - \frac{j}{\sqrt{ER}} \times \left\{ \cos\left[\frac{\pi}{2}\left(\frac{V(t)-V_{off}}{V_\pi}\right)\right]\right\} \right. \tag{2.2}$$

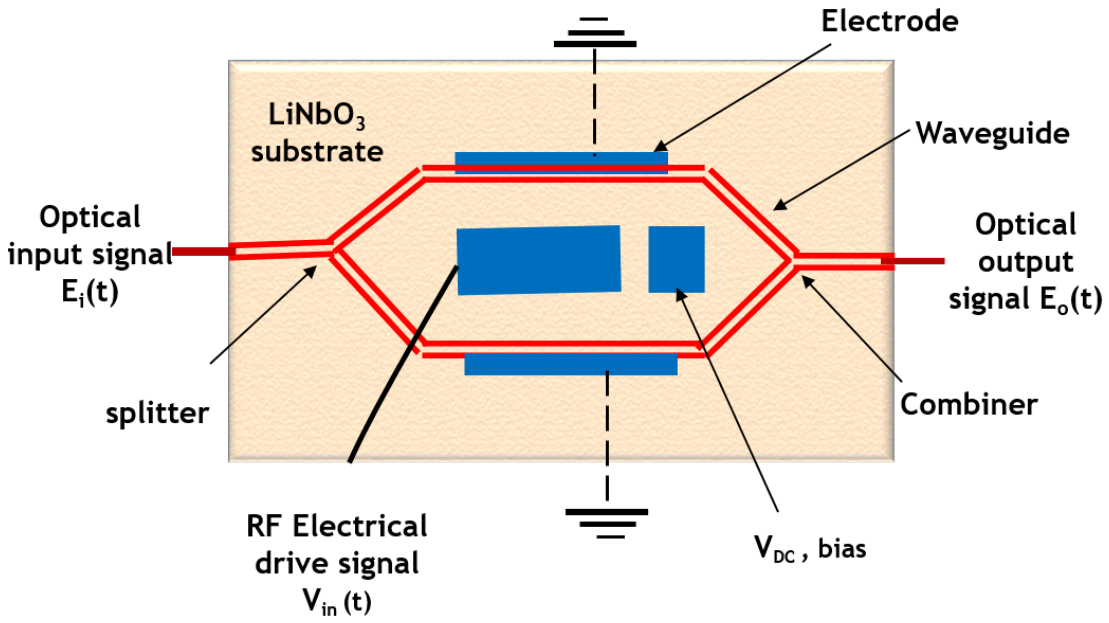

Figure 2.4: Lithium Niobate Mach-Zehnder Modulator.

The RF electrical drive signal governs the swing on the transfer curve, whereas the choice of DC bias voltage applied establishes the central point or operating point around which modulating swing appears. The choice of these two voltage signals are the controlling factors that can varied based on the specified type of application [42].

2.2.4 Erbium-Doped Fiber Amplifier (EDFA)

Optical amplifiers are used to compensate the optical signal power level that is reduced due to losses during propagation. The two Widely used optical amplifiers in telecommunication applications are Raman amplifiers and EDFA. A Raman amplifier is based on Raman gain, that results from the effect of stimulated Raman scattering and can be used to provide a widen gain bandwidth in fiber transmission cite58. In the simulation and experimental part of this Thesis we have used EDFA amplifier as described below.

Erbium doped fiber amplifiers are by far the most commonly adopted amplifier in the optical fiber communications. They can efficiently amplify in conventional C-band (1530-1565 nm) and long L-bands (1565-1625 nm) where the loss of telecommunication optical fibers become lowest in the entire optical electromagnetic spectrum [72]. EDFA can multiply multiple optical signals simultaneously and thus can be easily combined with WDM technology. It can be used as a booster amplifier (increase the launched optical power at the beginning of the link), in-line amplifier

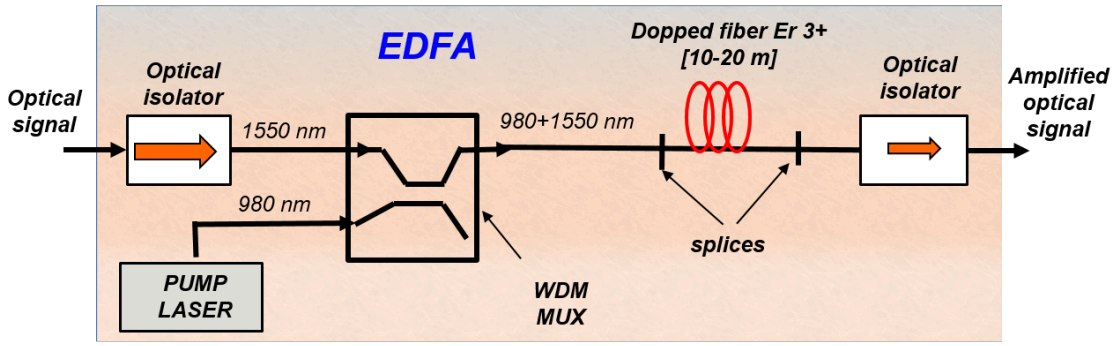

Figure 2.5: Erbium-doped fiber amplifier.

(compensate the attenuation induced by the fiber) and pre-amplifies (placed just before the receiver end such that sufficient power is launched to the receiver).

Amplification in EDFA takes place by using laser pump. The typical wavelengths used to pump EDFA are 980 or 1480nm. When an EDFA is pumped at 980 nm, Er ion doped in the fiber absorbs the pumped light is exited to an exited energy state. When sufficient launched power is pumped to the fiber and population inversion is takes place between ground and exited state, amplification by stimulation takes place at around 1550 nm[48].

Fig.2.5 shows the common internal configuration of EDFA amplifier. The input optical signal combined with pump laser in WDM multiplexer is launched in to Er doped fiber (EDF). The EDF create population inversion hence the input optical signal is then amplified by stimulated emission. Optical isolators (allow transmission of light only in one direction) place at the EDFA input and output, are used to prevent back reflection from the output port and stabilize the amplification process. Some important optical characteristics of EDFA are described as follows

- Saturated output power : is the maximum output power from the amplifier when it gets sufficient input power. An EDFA used as booster amplifier typically operates under this condition.

- Gain flatness : when EDFA is used for WDM transmission, ideally all the WDM channels have equal gain. However, in real scenario each of the channels has a different gain value and this variation is referred as gain flatness.

- Nose figure : is an important parameter of EDFA. Amplification in EDFA introduces noise to the optical signal that mainly occurs due to an amplified spontaneous emission (ASE) from the EDF. Consequently it reduces the Optical Signal to Noise Ratio (OSNR). Noise Figure (NF) of an amplifier indicate the degradation of an OSNR, in other words the EDFA with lower NF indicates lower noise characteristics (theoretically the minimum NF is 3 dB).

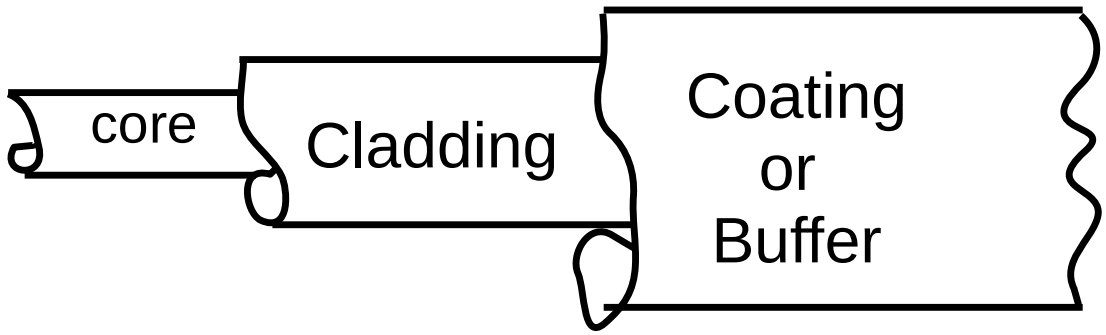

Figure 2.6: Structure of an optical fiber.

2.3 Optical channel

The optical channel in the IM-DD setup shown in Fig.2.1 is composed of a Standard Single Mode Fiber and Variable Optical Attenuator (VOA) which is used to emulate the over all optical distribution network (ODN) loss of the link.

2.3.1 Fiber

Optical fibers serves as the foundation of optical transmission systems due to the fact that they transport optical signal from source to destination. The combination of low loss and extremely large bandwidth allows high speed signals to be transmitted over longer distances with no need of amplification. An optical fiber is a very thin cylinder that acts as a dielectric waveguide by confining light (electromagnetic wave) from one end to other. It is usually made from glass or pure silica that shows very low attenuation at optical frequencies. In order to achieve two waveguide layers that have slightly different refractive indes (step index), the core is doped with materials that can increase the refractive index such as Titanium oxide, Germanium oxide, Di phosphorus trioxide, alumnium oxide and surrounded by cladding with lower refractive index value [94]. The core cladding refractive index ratio is chosen in such a way that light is totally confined with in core (total internal reflection) when propagating through the fiber. The common structure of an optical fiber is shown in Fig.2.6, the coating or buffer is used for mechanical reason (to support and protect the fiber).

The light propagating along the fiber follows only as such distinct electric field pattern across the fiber, each of the electromagnetic field is defined by a distinct mode on the fiber. Based on the number of waveguide modes that are allowed to propagate, fibers are classified as single or multi mode fibers.

Multi Mode Fiber

Multi mode fiber transfer the beam of light through spatial trasversal modes. Each mode is defined with a specific combination of electrical and magnetic components that occupies a different cross section of the core and takes distinguished path along the fiber. Thus the difference in mode path length results a different arrival time at the receiver end. This phenomenon referred as multi mode dispersion (intermodal dispersion), creates distortion and impose limitations on the signal bandwidth[94]. The typical core, cladding and coating diameter for multi mode fiber shown Fig.2.6 are 65 μm, 125 μm and 250 μm respectively.

Single Mode fiber(SMF)

In single mode fiber (SMF), the number of allowed waveguide mode in the fiber is only the fundamental one. As a result of this, the multi mode dispersion is eliminated. The fundamental mode occupies the central portion of the optical fiber and has a maximum energy at the axis of the fiber. The typical core, cladding and coating diameter Single mode fiber (SMF) shown Fig.2.6 are 9 μm, 125 μm and 250 μm respectively. The International Telecommunication Union (ITU) standardized the most common standard single mode fiber (SSMF) in ITU-T G.652 [54] specification with the following attributes:

- Attenuation : Typical attenuation coefficient in the wavelength range 1530 nm -1564 nm is 0.275 dB/km
- Chromatic distortion parameter at 1550 nm is 17$ps/km.nm$

2.3.2 Variable Optical Attenuator (VOA)

Variable optical attenuator is a passive device that is used to reduce the power level of an optical signal. It reduces the signal power in different ways, by absorbing the incoming light (absorptive principle), by scattering light (reflective principle) and gap loss principle. Absorptive principle introduce a power loss by inserting a material that converts some of the optical power into heat between the input and output port of the attenuator. The reflective principle or scattering is achieved by inserting a material that causes the optical signal to scatter. As a result the scattered light creates interference in the fiber there by reducing the optical power at the output side of the attenuator. Gap loss principle reduce the power level by using a longitudinal gap between two optical fibers so that the signal power is reduced at the output side of VOA[38].

Variable optical attenuators are commonly used in two scenarios :

- Permanently installed to properly match signal levels at the transmitter and receiver

- In fiber power level testing. In the experimental part of theis thesis, we used variable optical attenuator to temporary add a calibrated amount of signal loss in order to test the link power level margin (emulate optical distribution network loss).

2.4 Receiver side

The receiver side of the IM-DD optical setup shown in Fig. 2.1, consists of an optical band pass filter (BPF) (allow to pass in band signals in a certain wavelength range), avalanche photodetector (detect the optical signal into an electrical).

2.4.1 Optical Bandpass Filter (BPF)

Optical bandpass filter (BPF) is a device that selectively transmit light in desired range of wavelength and absorbs (block) the other. Examples of tunable bandpass filters are Lyot filter and Fabry-Pérot interferometer where the central wavelength is chosen by the user. The basic working principle of Fabry-Pérot interferometer is described as follows.

Fabry-Pérot interferometer is formed by separating two thin film reflectors with a thin film spacer. This configuration is also known as single cavity coating. In all dielectric cavity, the thin film reflectors are quarter wave stacks made with a dielectric material. Quarter wave stack is composed of alternating layer of two or more dielectric material each with an optical thickness corresponding to one quarter of central wavelength. This coating gives highest reflection at central wavelength and transmission at both higher and lower than the central wavelength. The spacer is a single layer dielectric material characterized by an optical thickness corresponding to an integral half of the central wavelength, induces transmission rather than reflection at the central wavelength. Therefore, light with a wavelength longer or shorter than the central wavelength undergoes a phase condition that maximize reflectivity and minimize transmission which results as a bandpass filter. The size of the passband , the degree of transmission and reflection out side the wavelength range is determined by the number and arrangement of the layer[83].

2.4.2 Photodetector

Optical photodetector is a device used to convert received optical signal into an electrical signal output that is proportional to the input optical power. Photodetectors to be used in optical communication systems should satisfy general requirements such as high sensitivity at the operating wavelength, high reliability, short response time to obtain suitable bandwidth, large electrical response to the received optical signal, minimum noise introduced by the detector, small size, low

bias voltage, and performance stability (temprature sensitivity). The most commonly used photodetectors in optical fiber communication applications are based on semiconductor materials usually are silicon, germanium, GaAs, InGaAs, etc, all which satisfy in various ways most of the photodetectors requirements[56]. They are mainly classified as positive intrinsic negative (PIN) and avalanche photodetectors (APD).

Positive Intrinsic Negative (PIN) photodector

PIN diode consisting of an intrinsic (lightly doped) region that is sandwiched between p-type and n-type layer is shown in Fig.2.7. Under reverse bias condition, the thickness of the depletion layer can be made sufficiently thick to absorb most of the incident light. A photon incident on the depletion region with higher or equal to the band gap energy of the fabricating material will excite an electron from the valance band into conduction band. This process leaves an empty hole in the valance band and is known as the photon generation of an electron-hole pair. The ideal photocurrent is proportional to the power of the incident light absorbed using anti reflection coating (used to prevent reflection of incoming light) as in Eq.2.3

$$i_{ph}(t) = \rho(\lambda)P(t), \tag{2.3}$$

where $\rho(\lambda)[A/W]$ is the responsibility of the photodiode that is related to the quantum efficiency η. It is defined as the ratio of the number of generated electrons to the number of incident photons as $\rho(\lambda) = \eta q/hv$, where q is the charge of electron and hv is the photon energy [94].

Avalanche Photodetector (APD)

The basic structure of Avalanche photodetector is shown in Fig.2.8. It posses similar structure PIN detector. However the main differences are APD requires higher reverse bias voltage and the intrinsic(i) zone (usually called π layer) is thicker.

The incoming photon passes through the thin p+ region are absorbed in intrinsic (π) layer and creates a hole electron pair. This charge carriers will be pulled by very high electric field (that comes from the high reverse bias) away from one another. Around the multiplication region the intense electric field strongly accelerate the charge carriers and pick up energy. When this electrons collide with other atoms they produce new electron hole pairs, the process called impact ionization will repeat. As a result of this impact ionization, a single arriving photon can produce many electron hole pairs, providing a much better level of sensitivity [94].

APD based receivers are most commonly used in the next-generation passive optical networks (NG-PON2) current prototypes. Because of their multiplicative property, APD boost the signal-to-noise ratio(SNR) of the detected optical signal

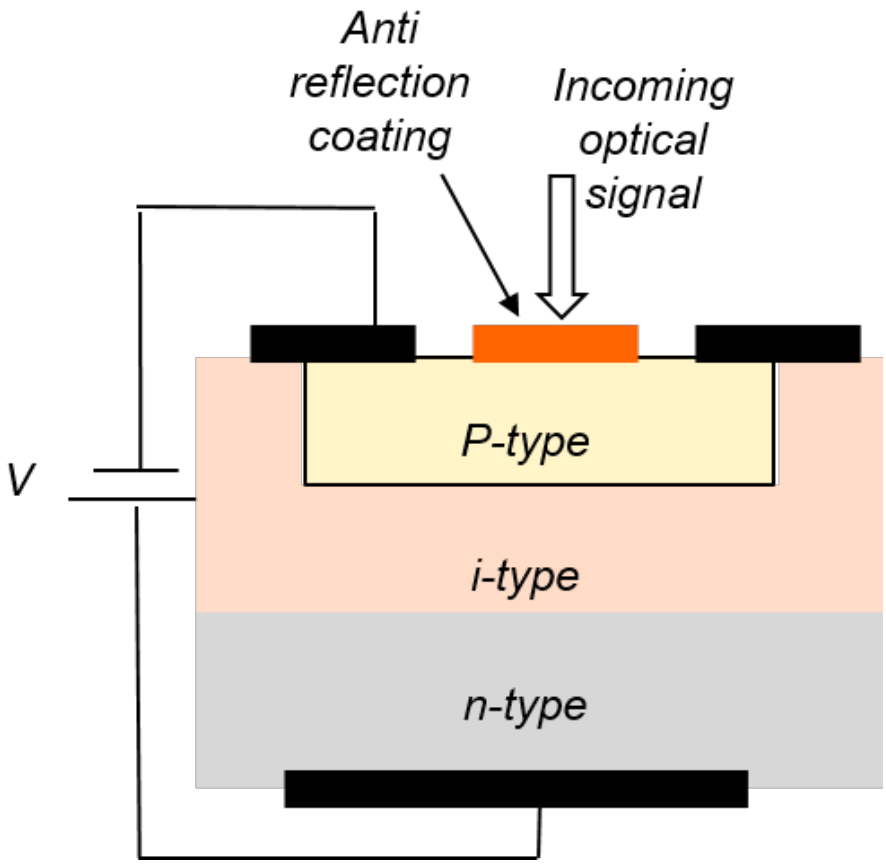

Figure 2.7: PIN photodiode.

even though they introduces excess noise[43]. APD is considered in this Thesis for the realization of IM-DD based fronthaul architecture. The ideal photocurent induced by APD is described in Equ.2.4 as

$$i_{ph}(t) = M\rho(\lambda)P_{in}, \tag{2.4}$$

where M is the maximum APD gain (multiplication factor), $\rho(\lambda)[A/W]$ is the responsibility of the APD and P_{in} input power of the incident light[49].

2.5 Chapter summary

This Chapter outlines the theoretical derivation and working principles of the opto-electronics components used in the IM-DD optical set up used in the realization of A-RoF fronthaul solution. The first part of this Chapter discuses about the transmitter side components, laser, arrayed waveguide grating, Mach-Zehnder-Modulator and Erbium-doped fiber amplifier which are used in the simulation model

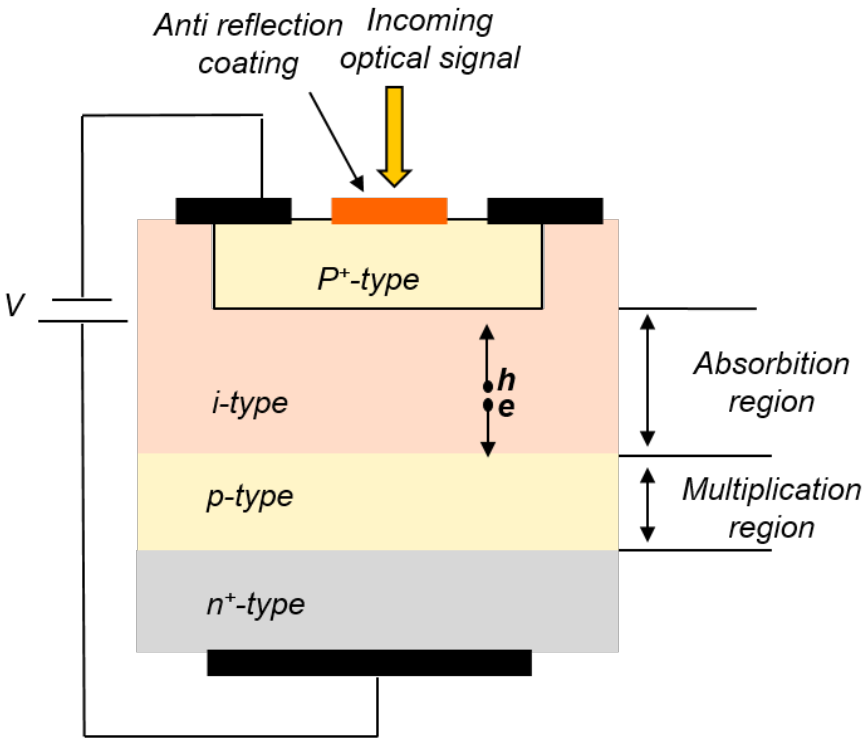

Figure 2.8: APD basic structure.

and experimental part of this thesis. The second Part explains about the general overview of optical channel components, fiber and variable optical attenuators used in IM-DD set up. The last parts of this Chapter describes about the optical components, optical band pass filter and potodetector used at the receiver side of the IM-DD setup.

Chapter 3

LTE and 5G NR physical layer overview

3.1 Motivation

The development of new technologies such as automated intelligence, Internet of things (IoT), high quality Internet protocol (IP) telephony, and high speed data communications, among others, are becoming a reality. These technologies requires faster, high capacity, quality of service (QoS) guaranteed, reliable, and continuous inter-connectivity among users and devices. The fourth generation (4G) long term evolution-advanced radio access network is introduced in the 3rd Generation Partnership Project (3GPP) specification with the main requirements of providing high spectral efficiency, high peak data rates, short round trip time as well as flexibility in frequency and bandwidth. This protocol is now being deployed worldwide. In the meantime 3GPP is in the process of developing the technical specification of fifth-Generation (5G) radio access technology, the so-called new radio (NR) aiming to provide unparalleled connected mobile society with the requirements of the International Mobile Telecommunications (IMT)-2020 and beyond [19]. Specifically the 5G NR is often used not only in radio access technology. It is also used in a wider range of new services foresee to be implemented by the future mobile communication technology. The 5G NR uses cases are classified into three classes: enhanced mobile broadband (eMBB) which corresponds to the evolution of the current 3G and 4G technologies, by supporting higher end-user data rates; massive machine-type communication (mMTC) which corresponds to services associated with massive number of devices that are required to have very low cost, low energy consumption and longer battery life; and ultra-reliable and low-latency communication (URLLC) type of services that requires very low latency and extremely high reliability [53].

The objective of this chapter is to provide an overview of the physical layer structures and the baseband signal processing flow used in the generation of the 4G

LTE and 5G NR waveforms based on frequency division duplex (FDD) transmission mode.

3.2 LTE physical channel structure

Multiple access schemes implemented on the fourth generation (4G) long-term-evolution (LTE) radio access technology are based on the conventional orthogonal frequency division multiplexing (OFDM) multiple access and single carrier frequency division multiplexing (SC-FDMA) technology for the downlink and uplink signal generation respectively. OFDM is a a special form of multicarrier transmission techniques in which the information transmitted on wide band channel is subdivided in frequency domain and align data symbols with several orthogonal subchannels (subcarriers). As a result, the individual spectra of each subcarriers overlap one another and achieve an efficient use of frequency spectrum. This provides an OFDM scheme that has spectral efficiency, robust to inter symbol interference (ISI) and inter carrier interference (ICI) caused by multipath fading, and a natural support for multiple input multiple output (MIMO) schemes. However, one of the major drawback associated with OFDM is the large variation in the instantaneous transmit power. This results mobile terminals to have higher power consumption [110]. Due to the fact that it is challenging to design complex power amplifiers in uplink transmission, SC-FDMA is implemented as an alternative technique by combining the conventional OFDM with a precoding based on Discrete Fourier Transform (DFT). SC-FDMA used in the uplink transmission can still achieve the advantages associated with OFDMA. In addition, it substantially reduces the fluctuation of the transmitter power observed in OFDM [41].

3.2.1 Multicarrier OFDM Transmission

OFDM is the downlink transmission scheme used in LTE standard. It is a special class of multicarrier modulation which represents broadband transmission bandwidth as a collection of many narrow band channels. Implementation of OFDM modulation/demodulation using inverse Discrete Fourier Transform (IDFT)/ (DFT) is demonstrated the first time in [108]. In an OFDM modulation, the original signal is first modulated and mapped into the resource grid, where each symbol is aligned in frequency domain. The IDFT then decompose each symbols (S_k assigned to a single subcarrier in the frequency axis) into sinusoidal identified by frequency and amplitude. An efficient fast Fourier transform (IFFT) is equivalent to modulation of sinusoidal orthogonal frequency subcarrier bank which corresponds to the total number of FFT points (N_{FFT}) shown in Fig.3.1.

The total bandwidth occupied by the total number of used subcarriers N_{sc} , each with spacing $\triangle f$ can be obtained as.

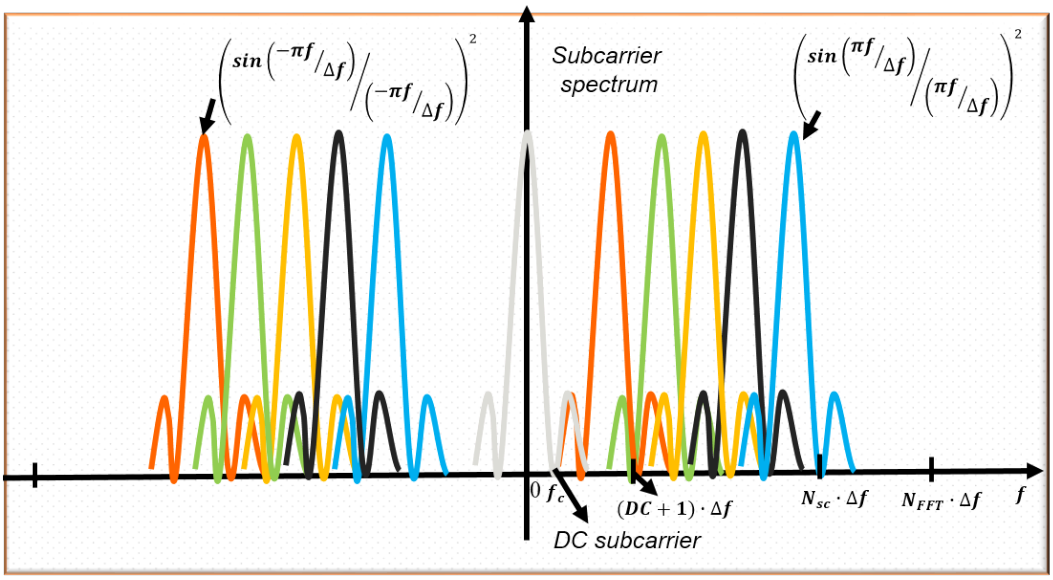

Figure 3.1: OFDM subcarriers.

$$BW = N_{sc} \cdot \triangle f. \tag{3.1}$$

The channel sampling rate is determined by the total number of subcarriers N_{FFT} according to.

$$F_s = N_{FFT} \cdot \triangle f. \tag{3.2}$$

The discrete time representation of one OFDM symbol using iFFT can be expressed as

$$x(m) = \frac{1}{N_{FFT}} \sum_{k=1}^{N_{FFT}} S_k \cdot exp\Big(\frac{j2\pi km}{N_{FFT}}\Big). \tag{3.3}$$

The FFT size (N_{FFT}) is selected based on the fact that it is implemented with modulo 2 algorithm and shall be a power multiple of 2. Moreover the design of iFFT should taking into consideration that it can easily be reproduced in a field-programmable gate array (FPGA) devices which gives efficient and provide fast implementation of the algorithm.

For the sake of an efficient and fast implementation, N_{FFT} is considered to the next power 2 of N_{sc}. For example if the number of subcarriers (N_{sc}) is 1200 then the FFT size (N_{FFT}) with the next power of 2 will be 2048.

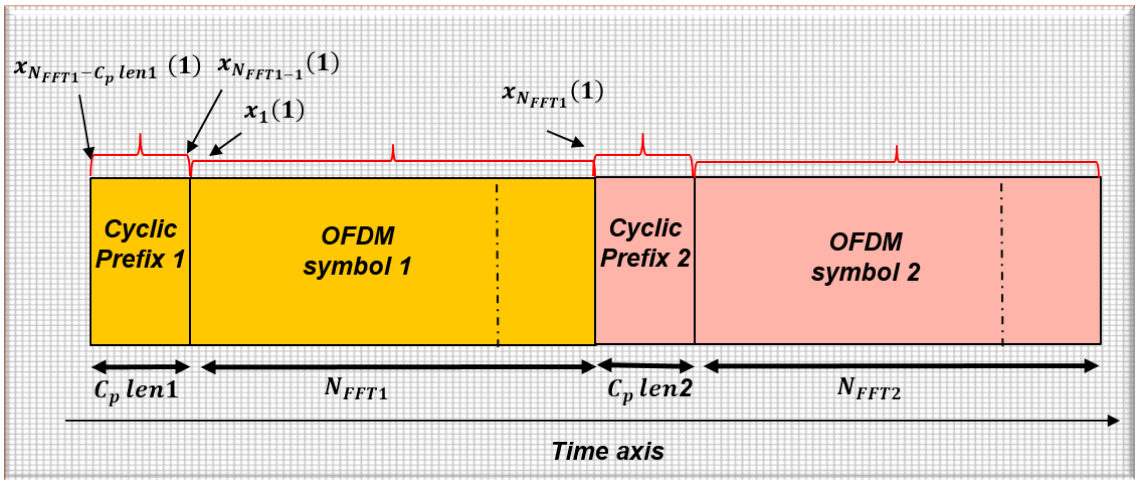

Figure 3.2: Cyclic prefix insertion on OFDM symbol

Cyclic prefix insertion

Cyclic prefix is an important functional block in OFDM signal generation. It is used to combat inter symbol interferences (ISI) between adjacent OFDM symbols that arises due to delay spread from time-dispersive channels or multipath fading that could give different path delays between subcarriers. For instance, consider two consecutive OFDM symbols (two subcarriers per symbol) affected by dispersive channel with a delay spread of t_d. The subcarriers are aligned up on transmission and at the receiver we keep the same FFT size as IFFT at the transmitter. Dispersive channels causes a delay of t_d in one of the subcarriers. As a result, the slower subcarrier crosses the symbol boundary causing interference with the neighboring OFDM symbols (ISI). In addition, an OFDM waveform in the FFT window for the delayed subcarrier is incomplete and causes inter carrier interference[64]. The method used to mitigate the ISI and ICI is to transmit quasi-periodically extended time domain blocks. That can be achieved by inserting cyclic extension of an OFDM symbol into a guard time interval (C_plen). As shown in Fig.3.2, a piece of the OFDM Time-domain symbol with length C_plen1 (Cyclic prefix) is copied from the tail of OFDM symbol 1 having a total subcarrier length N_{FFT1} and inserted at the head of OFDM symbol 1. Thus in the case of ISI, the lost portion (delayed subcarrier) is recovered with cyclic prefix and completed OFDM symbol is received in the FFT window at the receiver. Moreover, it allows the system to be insensitive to time-dispersive channels (as long as the span of the time dispersion doesn't exceed the $CPlen$) and preserve orthogonality between subcarriers[29].

As a trade off, cyclic prefix insertion causes symbol period extension, without addition of extra information(overhead) and therefore the net bit rate will be reduced by a factor of $N_{FFT}/_{(N_{FFT}+CPlen)}$. The choice of $CPlen$ must be sufficient to cover typical delay spreads encountered on real propagation channel scenarios

in cellular environment. On the other hand, it should create minimum overhead as possible. Two class of cyclic prefix lengths are specified in Evolved Universal Terrestrial Radio Access Network (E-UTRAN) LTE standard and they are indicated as "normal cyclic prefix" and "extended cyclic prefix". Normal cyclic prefix length can be either 144 or 160 samples, mostly used in urban cells and high data rate applications. Whereas extended cyclic prefix length is set to be 512 samples. For instance a 20 MHz LTE with FFT size (N_{FFT}=2048), the overhead with normal cyclic prefix insertion is 144 hence the net bit rate is reduced by $2048/(2048+144) \approx 0.934$. Whereas the overhead with an extended cyclic prefix is 512 causes the net bit rate reduction by $2048/(2048+512)$=0.8. Even though the longer (extended) cyclic prefix introduces more overhead (reduce transmission efficiency), it may be advantageous in specific channel propagation environments with an extensive delay spread. Typically in rural areas, and low data rate applications[29].

Peak-To-Average-Power Ratio

OFDM being a summation of large number of independently modulated subcarriers, may exhibits high instantaneous signal peak with respect to the average signal level. The probability of having the high peak is unlikely as the modulated data on each subcarrier is theoretically random and uncorrelated. The Peak-To-Average-Power Ratio (PAPR) of an OFDM signal can therefore be interpreted as a random variable with a distinct probability density function (pdf). According to central limit theorem, the sum of a large number of random variables (subcarriers) follows a Gaussian pdf in time domain with a very large tail in amplitude. When OFDM modulated signal changes from low instantaneous amplitude to a higher amplitude, large signal swing is encountered at the input of each electronic device in the transmission chain and consequently may lead to high harmonic distortion. This phenomenon potentially contaminates the neighboring channels with adjacent channel interference and impose non linear distortion[64]. The PAPR is quantified as

$$PAPR = \frac{P_{peak}}{P_{ave}}, \tag{3.4}$$

where P_{peak} is the peak power and P_{ave} is the average power of an OFDM waveform.

3.2.2 Single Carrier Frequency Division Multiplexing Access

Single carrier frequency division multiplexing access (SC-FDMA) is adopted in 3GPP specification for uplink transmission of LTE channels with the purpose of reducing the high Peak to Average Power Ratio (PAPR) observed in OFDM. It

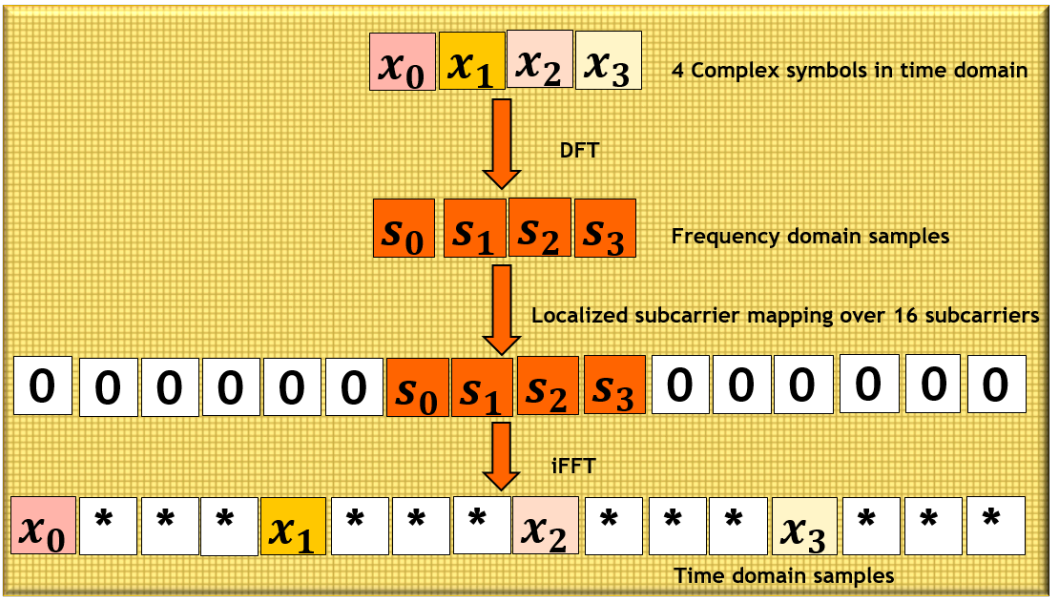

Figure 3.3: SC-FDMA transmitted symbols in time. domain.

is a modified form of OFDM scheme with a similar throughput performance and complexity that is implemented by preceding the OFDM modulator with Discrete Fourier Transform (DFT) precoder [93]. SC-FDMA, characterized by lower PAPR, highly benefits user equipment (UE) or mobile terminal in terms of transmit power efficiency and manufacturing cost.

The main difference of SC-FDMA with respect to an OFDM is each data symbol is spread over the entire allocated bandwidth. SC-FDMA signal appear to be like a single carrier by spreading the signal power over the bandwidth, consequently reduces the mean transmission power and guarantee that the dynamic range of the transmitted signal (stay in the linear region of the power amplifier)[110]. Where as in OFDM, each modulated data symbol is assigned to one designated subcarrier.

SC-FDMA can be regarded as Discrete Fourier Transform (DFT)-spread (M-point) OFDM (using N-point inverse Fast Fourier Transform (IFFT), where the M-point DFT output complex symbols is assigned as amplitude to N-point IFFT, a process known as subcarrier mapping. The two subcarrier mapping techniques mainly used in SC-FDMA are localized mapping and distributed (inteleaved) mapping. In localized mapping, the DFT output symbols of the input data (users) are mapped to a consecutive subcarriers hence occupies a dedicated part of the useful spectrum. On the other hand, the DFT output symbols in distributed mapping is interleaved over the entire bandwidth. Fig.3.3 shows an example of SC-FDMA transmission scheme with localized mapping. The number of available iFFT subcarriers (N=16) is shared by 4 blocks of symbols (users) each with DFT size (M = 4).

The PAPR of SC-FDMA is lower than that of regular OFDM. This is due to the fact that the effect of the N point IFFT is mostly canceled by the M point DFT. For example if M=N, the cascaded DFT and IFFT are completely canceled out and the symbols look like single carrier time domain symbols consequently with lower PAPR.

3.2.3 Time frequency frame structure

The bandwidth of an OFDM subcarrier spacing is selected based on the fact that smaller spacing allows a flat fading on each subcarrier . However, very low spacing will degrade the performance beyond a certain limit for the reason of Doppler shift and phase noise[110]. Therefore, selection of subcarrier spacing in OFDM based systems needs to carefully balance the overhead due to cyclic prefix against sensitivity to Doppler spread and other types of frequency errors[29]. The subcarrier bandwidths $\triangle f = 1.25kHz$, $\triangle f = 7.5kHz$ and $\triangle f = 15kHz$ are specified in the LTE standard [3, Section 4.2]. The most widely implemented subcarrier spacing in LTE is $\triangle f = 15kHz$ (used in this Thesis for LTE waveform generation).

One of the prominent feature of OFDMA is that the transmitted OFDM signal can be mapped in time-frequency representation as a resource grid. In LTE resource grid, the x-axis indicate the OFDM symbol to which it belong in time and the y-axis indicated the OFDM subcarrier in frequency.

Considering LTE frame structure type 1 in Frequency Division Duplex (FDD) mode as shown in Fig.3.4 [4, Section 4.1], one radio frame has a length of $10ms$. Different time units in LTE is expressed as a multiple of basic time unit $T_s = 1/(15000 \times 2048) = 1/30720000$. T_s can be considered the sampling time for an OFDM in LTE with an FFT size of 2048. Moreover, T_s is selected such that it is the exact multiple of the chip rates of UMTS and 1xEV-DO that are 3.84 Mcps and 1.22288 Mcps respectively. This would greatly reduce the complexity of chipset when LTE has to support UMTS and 1xEV-DO technologies with the same chipset. The radio frame is $T_f = 307200T_s = 10ms$ long and consists of 10 equally spaced subframes of length $T_{subframe} = 30720T_s = 1ms$ and it is numbered from 0 to 9. Scheduling in both downlink and uplink is done on the subframe basis. 10 subframes or 20 slots ($T_{slot} = 15360T_s = 0.5ms$) or up to 60 subslots ($T_{subslot} = 5120T_s = 0.1666ms$) are available for downlink and uplink transmission in every $10ms$ interval separated in frequency. Fig.3.4 shows type 1 LTE frame structure, where each slot consists of OFDM symbols that can either be seven for normal cyclic prefix (OFDM with normal cyclic prefix length is used in this Thesis) or six for extended cyclic prefix. The first OFDM symbol CP duration is set to $CPlen1 = 160T_s \approx 5.2\mu s$ and the remaining six OFDM symbols have $CPlen = 144T_s \approx 4.7\mu s$. The difference in $CPlen1$ is set to make the overall slot length divisible by 15360 ($0.5ms$).

A resource element is the smallest physical resource in LTE grid. It consist of

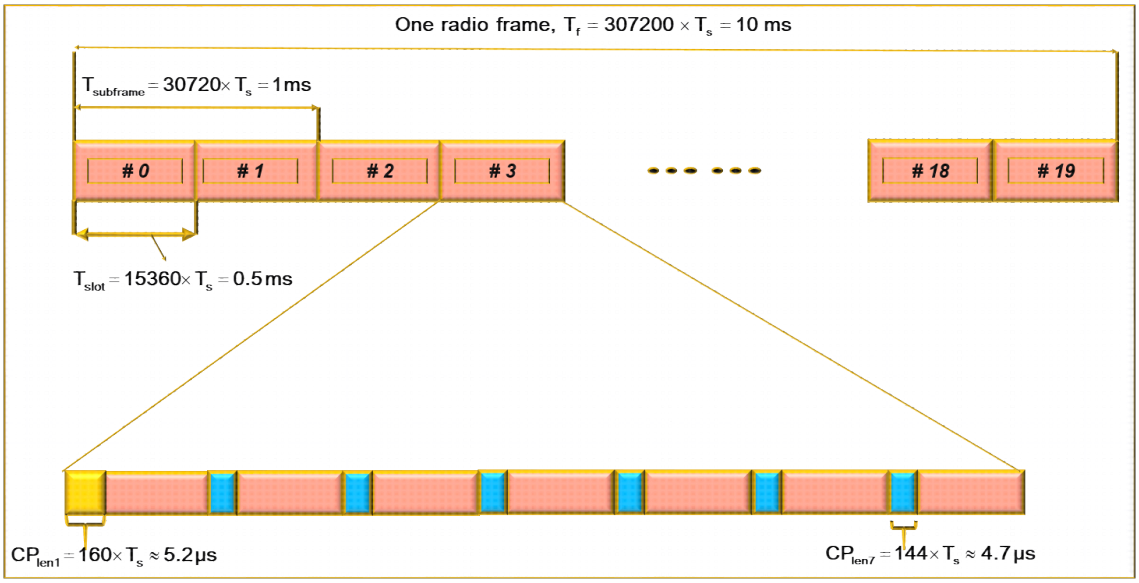

Figure 3.4: LTE frame structure type 1.

a subcarrier in frequency during one OFDM symbol duration. Furthermore, the resource elements are grouped into resource blocks, that are formed by a concatenation of 12 consecutive subcarriers in frequency each separated by $15kHz$. The total bandwidth of a resource block is $180kHz$ during one slot time. Each resource block thus consists of $7 \cdot 12 = 84$ resouce element in normal cyclic prefix and $6 \cdot 12 = 72$ resource elements in the case of extended cyclic prefix. Fig.3.5 shows LTE time-frequency resource grid using normal cyclic prefix.

The basic time domain unit for dynamic scheduling in LTE is one subframe. The minimum scheduling unit consists of two consecutive resource blocks, referred as a resource block pair[29, Chapter 5].

LTE transmission schemes allows a configuration of any number of resource blocks in frequency domain, that ranges from a minimum of six resource blocks to maximum of 100 resource blocks. The dynamic resource blocks allocation corresponds to an overall channel transmission bandwidth ranging from 1.4 to 20 MHz [2, Section 5.6]. Considering an efficient IFFT size (based on next power of 2), the sampling rate of each bandwidth can be obtained by applying Eq.3.2. Transmission configuration parameters (resource block, channel bandwidth allocation and sampling rate) for LTE physical transmission are summarized in Table 3.1.

3.3 LTE physical processing

The radio protocol for LTE is divided into user and control plane architecture. Application at user plane create data packet that are processed by Transport

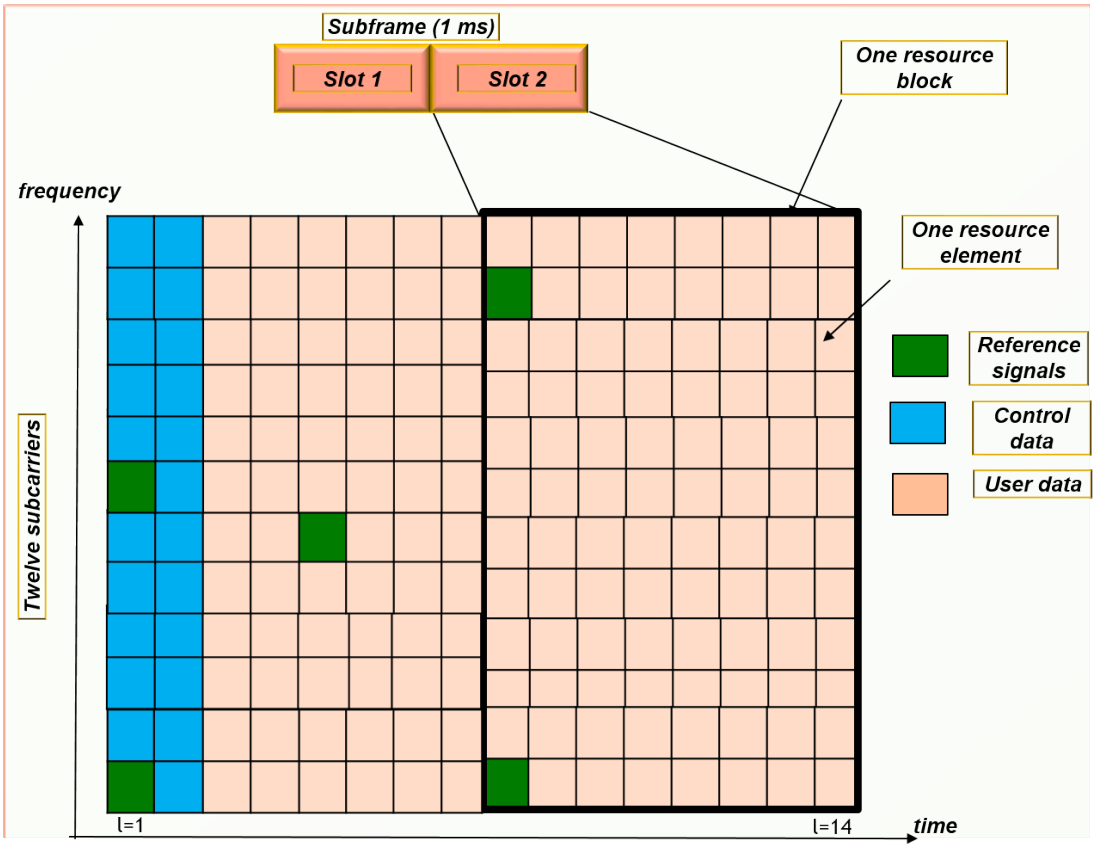

Figure 3.5: LTE physical time-frequency resource grid.

Table 3.1: LTE transmission configuration parameters : channel bandwidth , number of resource blocks and sampling rate.

Channel bandwidth	1.4	3	5	10	15	20
Resource blocks	6	15	25	50	75	100
FFT size	128	256	512	1024	1536	2048
Sampling rate [MHz]	1.92	3.84	7.68	15.36	23.04	30.72

Channel Protocol(TCP) and User Datagram Protocol(UDP), whereas in the control plane, the Radio Resource Control (RRC) protocol writes the signaling messages that are exchanged between the base station and the mobile. The control plane takes care of radio-specific functionality that depends on the state of the UE that are either idle or connected. The user plane protocol stack between eNodeB and user equipment(UE), consist of sub-layers such as Radio Link Control (RLC), Media Access Control (MAC) layer and Packet Data Convergence Protocol (PDCP).

Logical channels represent the data transfers and connection between RLC layer

and MAC layer. Two types of logical channels defined in LTE standard are traffic channel that is responsible for traffic user plane data and control channel that is responsible for transfer of control-plane information. Transport channels connects MAC layers to the physical layer (PHY) and the physical channels are then processed by transceiver at the PHY layer [110, Chapter 2]. A physical channel corresponds to a set of resource elements carrying information originating from the higher layers of LTE protocol stack to be transmitted on the air interface. Downlink data transmission uses transport channels such as Downlink Shared Channel (DL-SCH) for data transfer, Broadcast Channel (BCH) to provide system information to all mobile users connected to the base station (eNodeB), Paging Channel (PCH) to convey paging control about the paging information when searching a unit on the network and Multicast Channel (MCH) to transmit multi cast control information required for multi cast reception and set up multi cast transmission.

The uplink data transmission uses Uplink Shared Channel (UL-SCH), the only transport channel in LTE [5]. The mapping of DL-SCH in downlink side and UL-SCH in uplink on the physical channels are considered in the following Sections.

3.3.1 Uplink physical channels and procedures

The uplink physical channels defined in LTE standard [4, Section 5] are Physical Uplink Shared Channel (PUSCH), Physical Uplink Control Channel (PUCCH) and Physical Random Access Channel (PRACH). The PUSCH carries the user data transmitted from the Uplink Share Channel (UL-SCH) transport channel that is used for the transmission of all uplink higher layer information and uplink control information (UCI). PRACH is used for the initial access of user equipment (UE) to the network through transmission of random access preamble (random access channel procedure). The PUCCH carries UCI or uplink L1/L2 control signaling, which needs to be transmitted on uplink regardless of whether or not the UE has been assigned any resource for UL-SCH transmission [29, Chapter 7]. Depending on this, two modes of UCI transmission are supported in LTE standard as simultaneous and non simultaneous transmission of UL-SCH and UCI. Simultaneous transmission occurs when a resource is assigned for UL-SCH in the current subframe and non simultaneous transmission happens when the UE doesn't have a resource assigned for UL-SCH in the current subframe [6, Section 10.1].

UCI on PUCCH

If UE has not been assigned any resource for UL-SCH transmission, the UCI is transmitted on the uplink resource blocks assigned for UCI on PUCCH. Eight PUCCH format is defined in LTE standard [4, Section 5.4]. Fo instance, in the case PUCCH format 1b is characterized by carrying two information bits per subframe is used for HARQ acknowledgments (ACK/NACK), scheduling (signaling) requests

or a combination of the two. HARQ acknowledgments are used to acknowledge one transport block for the downlink signals. It is transmitted only when the UE correctly received control signaling related to the downlink transmission dedicated to the UE. Signaling Request (SR) are transmitted only when the UE request uplink resources for data transmission otherwise the UE should be silent to save battery resource and unnecessary interference.

UCI on PUSCH

If the UE is transmitting data on PUSCH, a valid resource blocks (scheduling grant) in the sub frame for control information is time multiplexed with user data. The first two symbols shown by the blue color portion in the Fig.3.5 are dedicated for control information. Only HARQ acknowledgments and CSI (Channel State Information) are transmitted on the PUSCH. Since the UE is already schedule , there is no need to request scheduling. Thus no SR is transmitted. The HARQ acknowledgments that is used for the proper operation of downlink transmission uses robust quadrature phase shift keying (QPSK) modulation format that can be multiplexed independently from the user data. The CSI report consists of channel quality indicator (CQI), Precoding Matrix Information (PMI) and Rank Indicator[110]. CQI is an indicator of the downlink radio channel quality. The CQI value allows the UE to feedback the base station (eNodeB) to set the optimal modulation scheme and coding rate values that align with the current radio link quality. There are sixteen CQI values specified in LTE standard [6, Section 7.2.3]. As the CQI value is higher, the corresponding modulation order and coding rates are also higher.

The PMI is an indicator for the dedicated precoding matrix to be used in a base station (eNodeB) for a given radio link. The RI signals the number of useful transmit antennas, estimated based on the channel quality and its effect on the correlations observed between adjacent receiver antennas. PMI and RI are mainly used in MIMO mode which is beyond the scope of this Thesis

Uplink physical signal

Two types of physical signals are defined for the LTE uplink[4, Section 5.5].

- Demodulation Reference Signal (DM-RS) are to be used by the base station (eNodeB) for channel estimation purpose intended in the demodulation of PUSCH and PUCCH. Thus, DM-RS are only transmitted being associated with PUSCH or PUCCH. DM-RS are indicated by the green resource elements shown in Fig.3.5.
- Sounding Reference Signal (SRS) are intended to be used by base station (eNodeB) for channel-state estimation to support the channel propagation dependent scheduling and link adaptation.

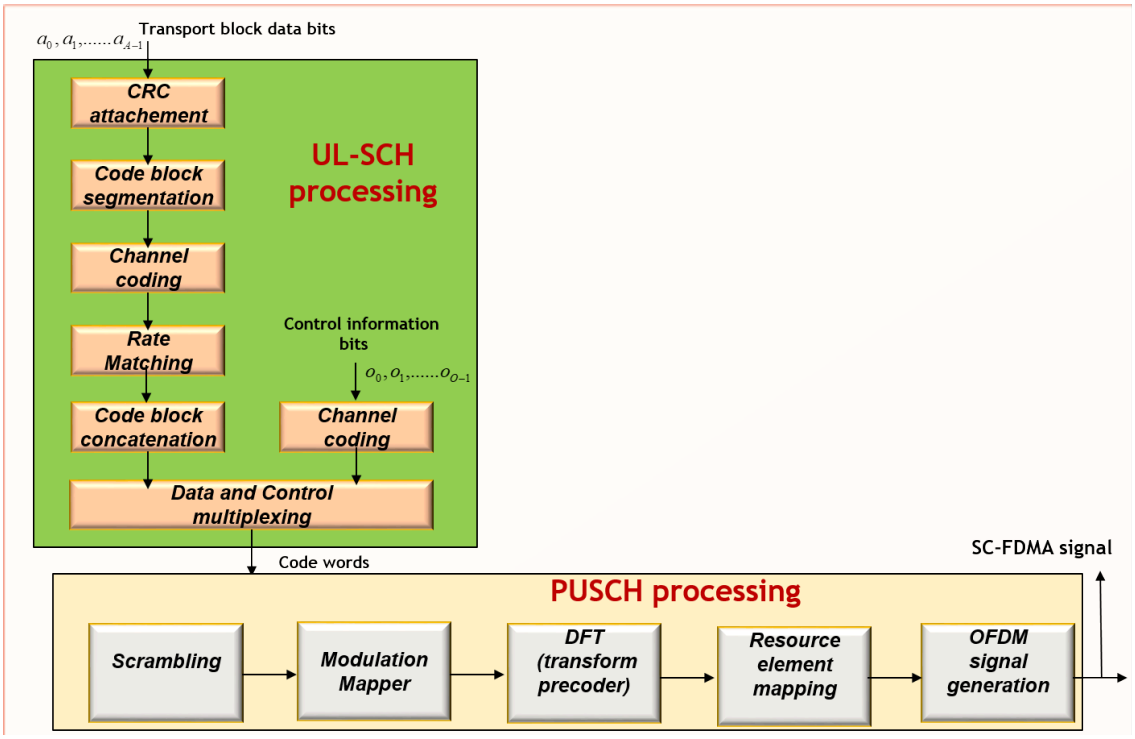

Figure 3.6: Overall Uplink signal processing chain of UL-SCH and PUSCH.

Uplink processing

Fig. 3.6 outlines the signal processing flow applied on the UL-SCH transport channel [5, Section 5.2] and the subsequent mapping to the PUSCH mapped on a single transmission base on one antenna port[4, p. 5.3].

Since resource scheduling in LTE is done on subframe basis, every transmission time interval (TTI) corresponding to $1ms$, there is at most one transport block in TTI. The signal processing procedure for PUSCH generation is described in the following Sections.

CRC attachment

Cyclic Redundancy Check (CRC) is the first step considered in the physical layer processing. CRC is an error detecting code provided in each transport block. The entire transport block is used to calculate the CRC parity bits of length 24 (appended on every block) through the following cyclic generator polynomial.

$$g_{CRC24A}(D) = [D^24 + D^23 + D^6 + D5 + D + 1]. \tag{3.5}$$

The CRC allows the receiver for the detection of transport block. The corresponding error status can then be used by the downlink HARQ acknowledgments with ACK or NACK indication.

Code block segmentation

In LTE turbo codes are used for Forward Error Correction (FEC) technique in the data channels. Turbo code in LTE is a systematic Parallel Concatenation Convolutional Codes (PCCC) with two 8-state constituent encoders and one contention free internal interleaver. LTE defines the maximum internal interleaver size of turbo encoder for channel coding code block size to be $Z = 6144\,bits$ and the minimum size to be $Z = 40 bits$. If the transport block size including 24 CRC parity bits exceed the maximum block size, it will be segmented into smaller code with the size supported by the turbo encoder. Moreover, an additional 24 bit CRC is attached on every block code. If the transport block size is less than the maximum size, there will be only one block code per transport block or if it less than the minimum block size filler bits are added on the transport block size.

Channel coding

Channel coding for UL-SCH based on turbo coding or Parallel Concatenation Convolutional Codes (PCCC) using two 8-state constituent encoders rate-1/2 and-1/1 implying that the overall coding rate of 1/3 and one internal interleaver[62, Chapter 10]. The structure of the turbo encoder is shown in Fig.3.7. The encoder starts from initial state zero at position A and each constituent encoder is independently terminated by a tail bit at position B. For an input block size of K bits, the output of the turbo code consists of three length $(3 \cdot K)$ bit streams, corresponding *Systematic bit*, *Paritybit* 1 and *Paritybit* 2 streams, as well as twelve tail bits for trellis termination. The tail bits are multiplexed with in the three output streams hence its length increased to $K + 4$.

Interleaving is a technique of swapping the position of input bit in a non contiguous way so that the forward error correction is robust with respect to burst error. Thus, selecting an interleaver has stong impact on the error performance of the turbo encoder. The internal interleaver shown in Fig.3.7 for the LTE turbo encode is based on Quadratic Permutation Polynomial (QPP) interleaver that is a contention-free interleaver suitable for parallel turbo decoder implementation [89], implying the decoding can be parallelized without the risk of contention when parallel process are accessing the interleaver memory. QPP interleaver provides mapping from input bits to the out bits based on the relation

$$\prod(i) = \left(f_1 \cdot i + f_2 \cdot i^2\right) mod\, K, \tag{3.6}$$

where i is the bit index at the interleaver output, $\prod(i)$ is the same bit index at the input of the interleaver, K is the code block size (interleaver size) in the range of [40 - 6144] bits. The parameters f_1 and f_2 depend on the block size K that is summarized in [5, Section 5.1.3].

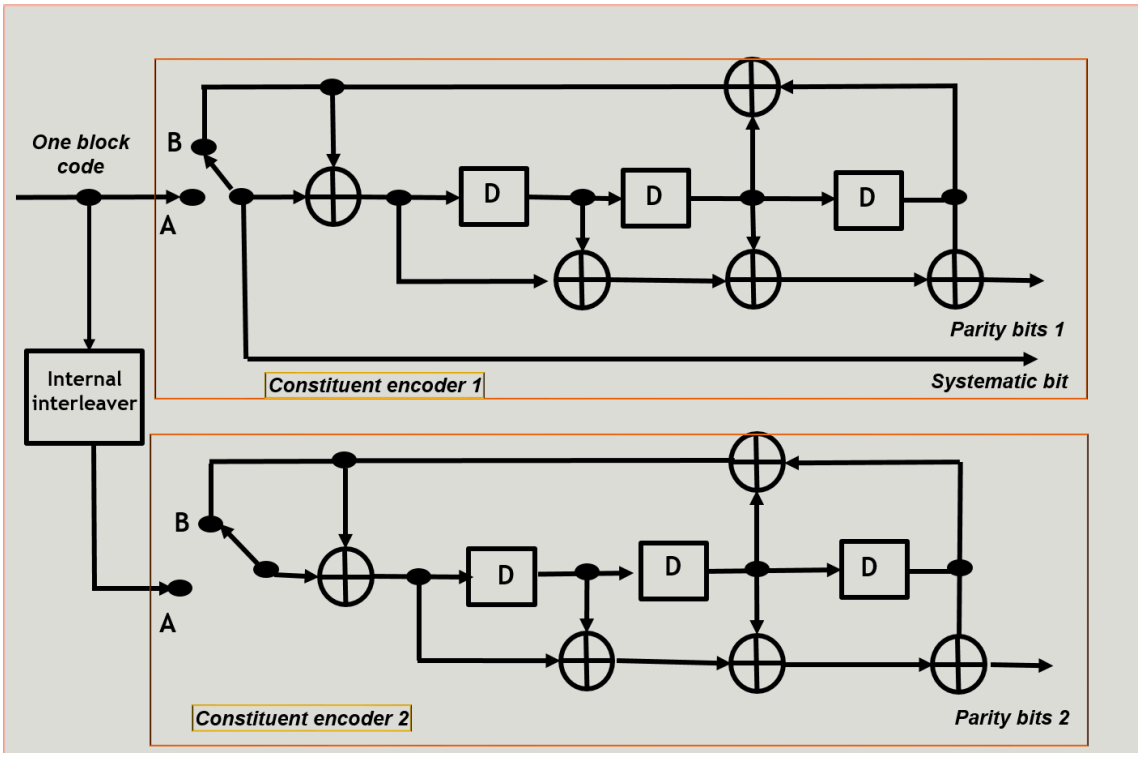

Figure 3.7: Rate 1/3 turbo encode structure.

Rate matching

Rate matching is used to extract the code words from the output of the turbo code and set the exact code bits to be transmitted within the current subframe (TTI). The rate matching for turbo coded output, defined per block codes is illustrated in Fig.3.8, where each of the the three output steam of the turbo code indicated as $Systematic bit$, $Paritybit\,1$ and $Paritybit\,2$ in Fig.3.7 is rearranged by its own sub block interleaver[25]. Each sub block interleaver works based on row-column permutation. Code block can then be visualized as a rectangular matrix format such that 1 dimensional code block is obtained by reading bits column-wise (32 columns are assigned in LTE).

Bit collection buffer is formed by inserting the interleaved systematic bits at first and then bit by bit interlacing of the two interleaved parity bits streams. Due to the fact that sub block interleaving are based on row-column permutation, interlacing allows equal level of protection for each constituent encoder parity bits.

For matching the desired code rate, the number of coded bits to be selected for transmission depends on the redundancy version (RV) corresponding to different starting points for the extraction of the coded bits from the buffer[29, Chapter 6]. The bit selection reads out first desired number of code bits from the start of the buffer.

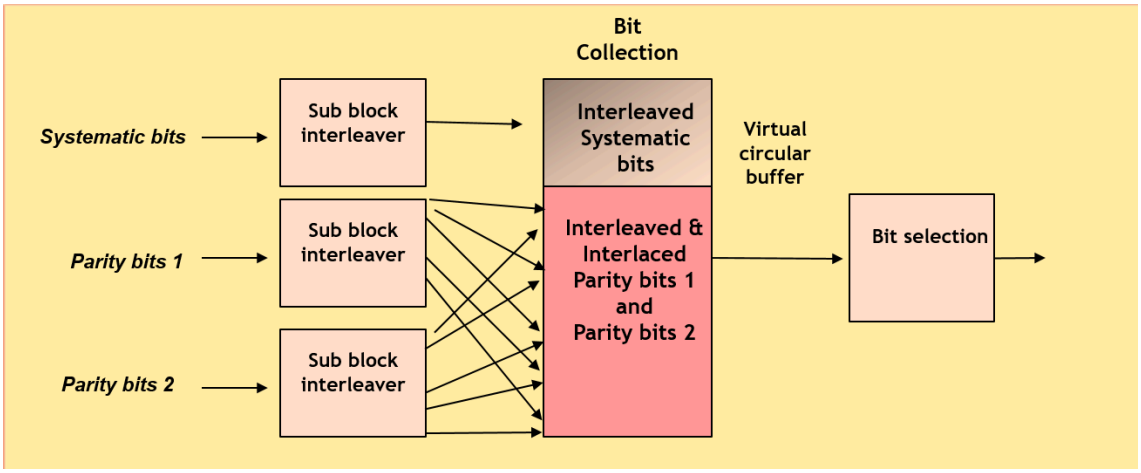

Figure 3.8: Rata matching for turbo code rate-1/3.

Scrambling

Scrambling in uplink applied to the coded bits in every code words delivered from UL-SCH imply multiplication (exclusive-or operation) by a predefined scrambling sequence of bits to be transmitted on the physical channel. Applying different scrambling sequence for neighboring cells makes the interfering signal after de-scrambling to be randomize hence ensures the processing gain provided by the channel code [6, Section 5.3.1].

SC-FDMA modulation Mapper

The uplink modulation mapper is used to map the block of scrambled bits to the corresponding block of complex modulation symbols. In LTE standard, the set up modulation formats for UL-SCH processing are quadrature phase shift keying (QPSK), 16-QAM (quadrature amplitude modulation) and 64-QAM. The number of bits carried per symbol can be obtained by 3.7

$$n = \log_2(M), \tag{3.7}$$

where n is the number of bits mapped per symbol and M is the constellation cardinality. Modulation with high cardinality is used when the the channel quality is high.

DFT (Transform precoder)

The DFT precoding part is depicted in Fig.3.9. The $K \times M$ serial complex modulated data from the modulation mapper is converted in to parallel K blocks of M symbols. The M symbol (time domain signal) is fed through an M-point

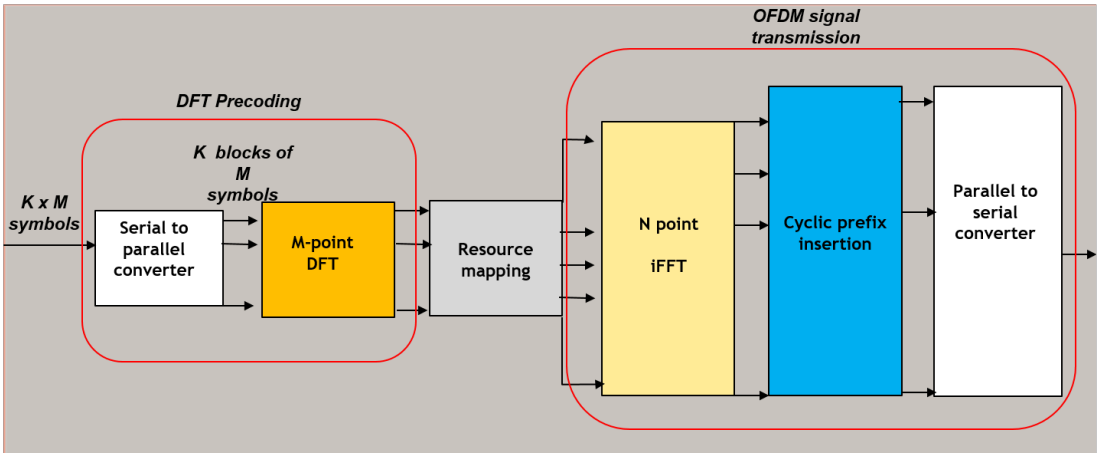

Figure 3.9: SC-FDMA signal generation scheme.

DFT to produce a frequency domain representation of the input signal. The DFT size imply the data subcarriers assigned for transmission and it should be a power multiple of 2 (for efficiency and implementation complexity). However, this kind of constraint may limit the flexibility of resource scheduling in uplink transmission.

Resource mapping

The DFT output data symbols are mapped to a subset of subcarriers within the resource mapping block shown in Fig.3.9. The Resource mapping assigns the DFT output as an amplitude for the selected subcarriers and can be classified as localized mapping or distributed mapping. In the case of localized mapping, the DFT outputs are mapped to a subset of consecutive subcarriers in a certain bandwidth range. Instead in distributed mapping the DFT output are assigned to the entire subcarries over the entire bandwidth non-continuously[93]. In the example of localized mapping (which is considered in this Thesis) shown in Fig.3.3, the available N=16 point IFFT subcarriers are shared by K=4 blocks (users) each occupies M=4 (DFT) subcarriers. In this case N is related to K and M as $N = K \times M$.

OFDM signal generation

An N point IFFT shown in Fig.3.9 is used to transform the complex subcarrier amplitude to a complex time domain signal. Every point in IFFT modulates a single subcarrier and the summation of the over all modulation is transmitted sequentially as OFDM signal. Furthermor, cyclic prefix is inserted and transmitted serially.

3.3.2 Downlink physical channels and procedures

Downlink physical channel corresponds to a set of resource elements carrying information originating from the higher layers such DL-SCH and downlink control information (DCI) that are not sent by the higher layer. The downlink physical channels defined in [4, Section 6] are the Physical Downlink Shared Channel (PDSCH) which unicast user data and paging information, Physical Downlink Control Channel (PDCCH) serves to map and convey DCI, Physical Hybrid-ARQ Indicator Channel(PHICH) carries HARQ Indicator (HI) and ACK/NACKs for the uplink packets, Physical Control Format Indicator Channel (PCFICH) contains Control Format Information that are necessary to decode PDCCH information, Physical Downlink Multicast Channel(PDMCH) used for Multimedia Broadcast Single Frequency Network (MBSFN) operations, and Physical Broadcast Channel(PBCH) carries system information required by the UE in order to access the network during cell search procedure.

Physical layer transmission in LTE technology usually uses multiple antenna for downlink, that meaning that the eNodeB uses multiple transmitter antenna and UE uses multiple receiver antenna. This way of transmission can be configured in various multiplexing, precoding methods, DCI format, and transmission scheme of PDSCH is called as Transmission Mode (TM)[6]. For example TM1 (Transmission Mode 1) can be associated with DCI format 1A and 1 and transmission scheme of PDSCH corresponding to PDCCH as single transmit antenna and single receiver antenna (single antenna port). TM2 is linked with transmission scheme of Transmit Diversity, TM3 and TM4 are associated with MIMO transmission with out feedback from UE and with UE feedback (CQI, PMI and RI). The detail of TM is presented in [6, Section 7].

Downlink reference signal

Downlink reference signals are predefined dedicated resource element with in the OFDM time-frequency grid. In Fig.3.5, downlink reference signals are indicated the green resource element. Five types of downlink reference signals are specified in LTE standard to be used by UE for different purposes as, cell-specific reference signals (CRS), demodulation reference signal (DM-RS), Channel State Information reference signals (CSI-RS), MBSFN reference signal and positioning reference signals.

Downlink processing

The downlink baseband signal processing of PDSCH generation is shown in 3.10. The PDSCH carries DL-SCH user data as a transport blocks that are transmitted at a time per a subframe. In other words, transport blocks are transmitted with

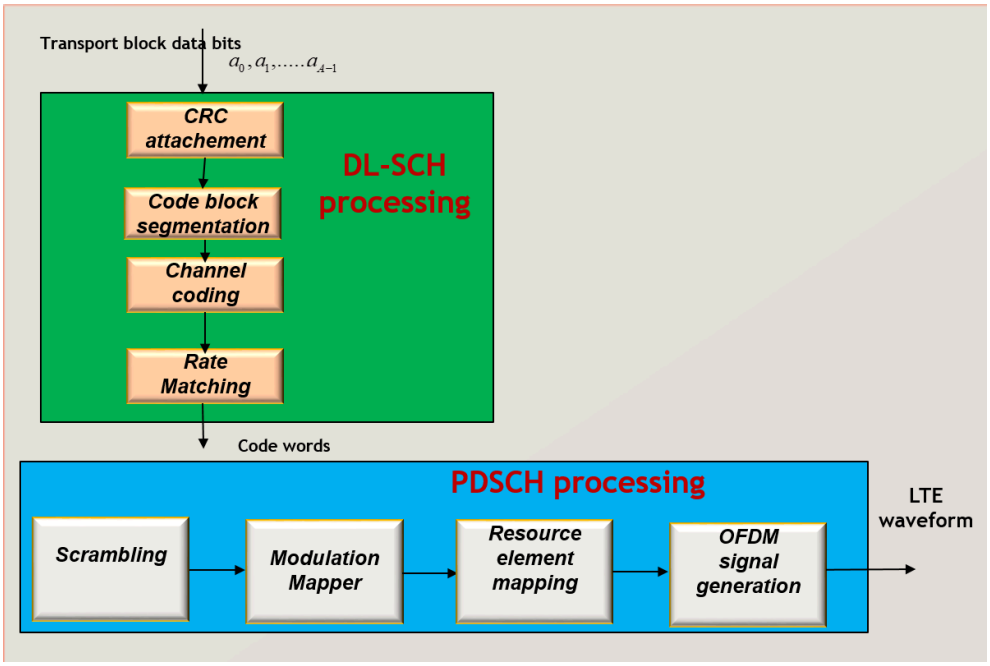

Figure 3.10: Overall downlink signal processing chain of DL-SCH and PDSCH.

a transmission time interval (TTI) at every 1 ms. Basically the DL-SCH and the UL-SCH processing shown are almost similar and summarized as follows.

- CRC attachment : CRC with 24 parity bits is calculated and attached on each transport block.
- Code block segmentation: used to limit the internal interleave size of the turbo encoder with the same parameters described as in the uplink.
- Channel coding : Turbo coding rate-1/3 using QPP based internal interleaver shown in Fig. 3.7 can also be used on DL-SCH.
- Rate matching : The rate matching algorithm of DL-SCH is essentially the same as that of UL-SCH elaborated in Fig.3.8
- Scrambling : The purpose of downlink scrambling is the same as that of the uplink, that is to randomized the downlink interference between neighboring cells. Thus ensure the processing gain provided by the turbo code to be fully optimized.
- Modulation Mapper : The data modulation format are similar to that of the uplink QPSK, 16QAM and 64 QAM. Moreover, 256 QAM can be used in downlink where channel quality is quite high. Resource element mapping : Modulated

symbols from the modulation mapper output are mapped as an amplitude of the selected subcarrier.

- OFDM signal generation : The same principle of OFDM generation process is implemented as shown in Fig.3.9.

3.4 5G/NR physical structure

Similar to the 4G LTE Section.3.1, OFDM multi carrier transmission scheme is also adopted in the 5G NR technology. This is due to the fact that the OFDM robustness to time dispersion and simplicity to be represented in time and frequency resource grid. However, unlike in LTE where SC-FDMA (DFT-precoded OFDM) is the only uplink transmission schemes, 5G NR uses the conventional OFDM also for the uplink transmission with the motivation of having the same transmission scheme in both uplink and downlink directions. Nevertheless, SC-FDMA can also be used as an alternative in uplink for the purpose of its advantage in reducing high Peak-to-average power ratio (PAPR). In the analysis of NR uplink channels of this Thesis, the conventional OFDM is applied for waveform generation.

3.4.1 5G NR numerologies

5G NR as a candidate technology for International Mobile Telecommunications (IMT)-2020 and beyond[59], defined to operate in a wide range of carrier frequencies from sub-6 GHz specified as frequency range 1 (FR1) (from $450MHz - 6GHz$) up to millimeter wave (mmWave) band designated as(frequency range 2 (FR2)) $24.256GHz - 52.6GHz$ [9, Section 5.1]. In order to operate on the wide range of deployment scenarios, 5G NR is designed to supports multiple subcarrier options ranging from 15 kHz to 240 kHz selected with appropriate handling of multi-path delay spread and phase noise that relies on the carrier frequency range. Thus, the corresponding cyclic prefix duration changes accordingly [11, Section 4]. Supported subcarrier spacing can be obtained as Eq.3.8 and summarized in Table 3.2.

$$\triangle f = 2^{\mu} \cdot 15[kHz], \tag{3.8}$$

where μ is the subcarrier spacing type [0-4] and $\triangle f$ is subcarrier spacing [15kHz - 240 KHz].

3.4.2 Time-frequency frame structure

Downlink and uplink NR waveforms transmissions are organized into frames with $T_f = (\frac{\triangle f_{max} \cdot N_f}{100})T_c = 10ms$ duration, each consisting of 10 equally spaced subframes of $T_{sf} = (\frac{\triangle f_{max} \cdot N_f}{1000})T_c = 1ms$ duration, where $\triangle f_{max} = 480 \cdot 10^3 Hz$

Table 3.2: NR transmission numerologies.

μ	$\triangle f = 2^{\mu} \cdot 15[KHz]$	Cyclic prefix length [Samples]
0	15	normal (144)
1	30	normal (144)
2	60	normal (144), extended (512)
3	120	normal (144)
4	240	normal (144)

and $N_f = 4096$ [11, Section 4]. To provide consistent and exact time definitions, time intervals with in the NR specification are defined as a multiple of basic time unit $T_c = \frac{1}{\triangle f_{max} \cdot N_f}$. The basic time unit T_c can be considered as a sampling time of an FFT-based transceiver implementation for maximum subcarrier spacing of $480kHz$ with a FFT size set to 4096 . A subframe in turn is divided into slots, each consisting of 14 OFDM symbols.

Subcarrier spacing 15 kHz was selected as a baseline for 5G NR numerology, motivated by the coexistence with LTE. Consequently the NR slot structure for 15 kHz subcarrier spacing is identical to LTE subframe structure described in Section 3.2.3. The slot structure with higher subcarrier spacing in NR is derived by scaling the baseline structure to the power of two [30, Chapter 7]. The number of consecutive OFDM symbols in a subframe thus depend on the subcarriers spacing type Eq.3.9[11, Section 4.3]. Table 3.3 summarizes required number of OFDM symbols in a slot, where the number of slots in a frame and the number of slots in subframe for subcarries spacing type μ cab be obtained from Eq.3.9.

$$N_{symb}^{subframe,\mu} = N_{symb}^{slot,\mu} \cdot N_{slot}^{subframe,\mu}. \tag{3.9}$$

Frame structure defined in NR numerologies is shown in Fig.3.11. Since slot is defined as fixed number of OFDM symbol, as the subcarrier spacing (μ) increases by one the slot duration decreases by half. This principle is fundamental to support low latency application. However, the cyclic prefix also shrinks as a subcarrier spacing increases hence can not be implemented in all kinds of deployment scenarios.

Unlike LTE, that was designed to support a maximum bandwidth up to 20 MHz, 5G NR is designed to support very wide bandwidth (up to a maximum of 400 MHz) in a single NR waveform. A resource element (RE), the smallest physical resource in NR consists of one subcarrier with a bandwidth determined by subcarrier spacing type μ during one OFDM symbol. Physical resource block (PRB) are formed by a concatenation of 12 consecutive resource elements. The frequency domain frame structure for subcarrier type $\mu = 3$ ($\triangle$ f = 120 kHz) is shown in Fig.3.12. Physical Resource Block (PRB) definition in NR is different from that of LTE. NR physical

Table 3.3: Number of OFDM symbol in a slot, number of slot in a frame and number of slot in a subframes required per subcarrier spacing type μ.

μ	$N_{symb}^{slot,\mu}$	$N_{slot}^{frame,\mu}$	$N_{slot}^{subframe,\mu}$
0	14	10	1
1	14	20	2
2	14	40	4
3	14	80	8
4	14	160	16

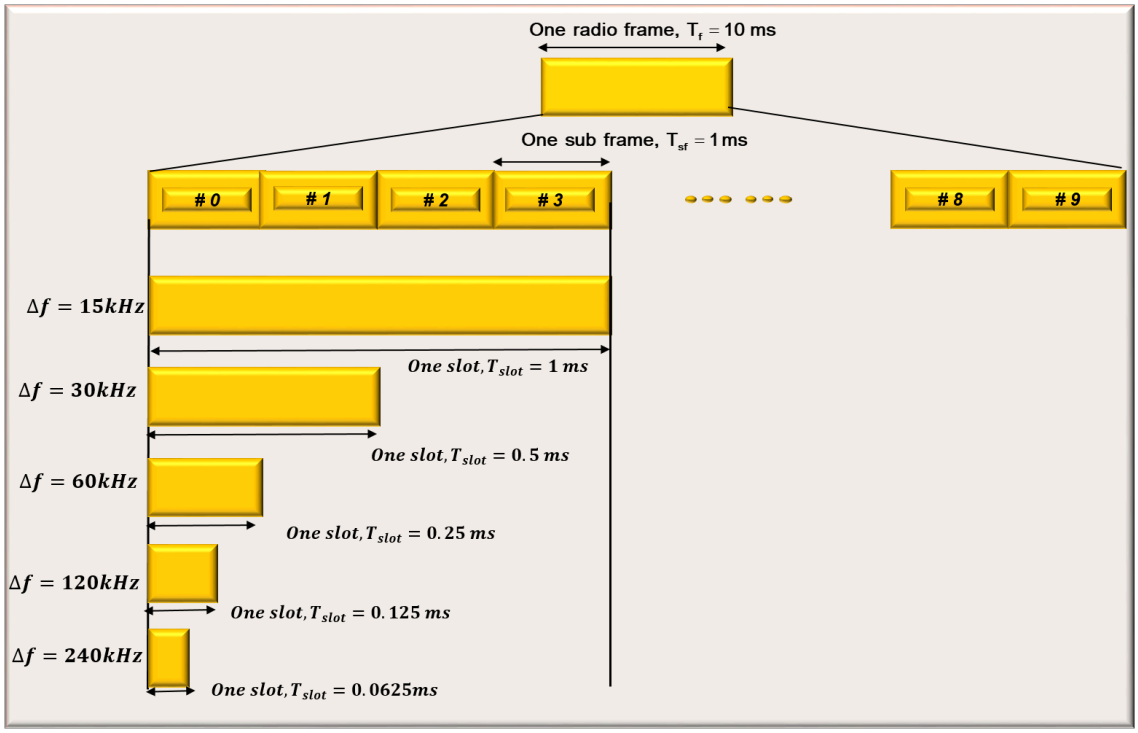

Figure 3.11: Time domain NR frame structures.

resource block is twelve resource elements only in frequency domain in one OFDM symbol where as in LTE shown in Fig. 3.5, it consist of twelve subcarriers in frequency and one slot in time domain. The total bandwidth of a physical resource block is calculated as $BW_{PRB} = 12 \times \triangle f$. For instance, $\mu = 3$, RB bandwidth becomes $BW_{PRB} = 12 \times 120\text{kHz} = 1.44$ MHz.

NR physical layer transmission define multiple bandwidth configuration (resource block) for every subcarrier spacing types (SC Types). The maximum bandwidth allocation ranges from 50 MHz ($\mu = 1$) up to 400 MHz ($\mu = 4$). Table 3.4 illustrate NR numerologies [10, Section 5]. The maximum nominal bandwidth can be obtained as Max BW = Maximum PRB $\times 12 \times \triangle f$. For example, Max BW for

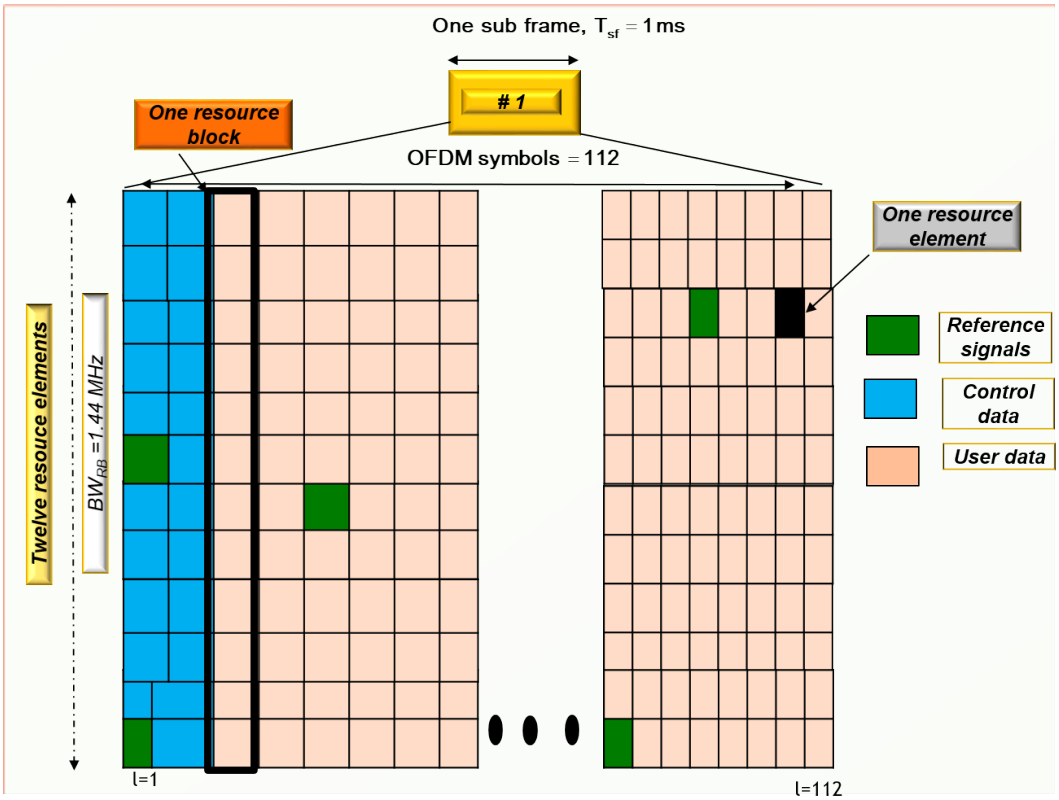

Figure 3.12: NR frequency domain frame structure of $\mu = 3$.

Table 3.4: NR transmission configuration parameters : channel bandwidth , number of resource blocks and sampling rate.

Subcarrier spacing (μ)	0 ($15kHz$)	1 ($30kHz$)	2 ($60kHz$)	3 ($120kHz$)	4 ($240kHz$)
Minimum PRB	20	20	20	20	20
Maximum PRB	275	275	275	275	138
Maximum BW [MHz]	49.5	99	198	396	397.44
Maximum Subcarriers	3300	3300	3300	3300	1656
FFT size	4096	4096	4096	4096	2048
Sampling rate [MHz]	61.44	122.88	245.76	491.53	491.53

SC Type $\mu = 3$ (120 kHz) is $275 \times 12 \times 120$ KHz $= 396$ MHz

3.5 NR physical processing

Logical channels represent the data transfers and connection between Radio Link Control (RLC) layer and Media Access Control (MAC) layer. The MAC layer handles logical channel multiplexing and scheduling related functions for different numerologies. MAC layer provides service to the RLC in the form of logical channels. As in LTE, logical channels are defined based on the type information they carry as control channel that is responsible for the transmission of control and configuration information in NR operation and traffic channel that carry the user data [30].

The MAC layer provides service to/from the physical layer in the form of transport channels, which defines how the data information is transmitted over the radio interface. Data on transport channels are grouped into transport blocks. The physical layer provides service to the MAC layer in the form of transport channels with in transmission time interval TTI. Physical channels corresponds to a set of resource elements required for transmission of transport channels such as UL-SCH (for uplink) and D-SCH (for downlink) that are originated from the higher layer of 5G NR protocol stack. Moreover, control channels, DCI and UCI are physical channels without dedicated transport channels that are used to provide necessary control information about the downlink and the UE in uplink transmission respectively.

3.5.1 Uplink physical channels and procedures

Similar to LTE, the uplink physical channels defined in NR standard are Physical Uplink Shared Channel (PUSCH), Physical Uplink Control Channel (PUCCH) and Physical Random Access Channel (PRACH)[11]. PUSCH is responsible to carrying and set up resource blocks for user data of UL-SCH transport channel and UCI. PUCCH is the basis for the transmission of uplink control. In practice, UCI could be transmitted on the PUCCH regardless of whether the user device is transmitting data on the PUSCH. The UCI transmission modes on PUCCH and PUSCH are similar to the LTE structure described in Section 3.3.1. PRACH is used for the initial access of the device to the available cell through data transmission of random access preamble [11, Section 6].

Uplink physical signals

The uplink physical signal are used by the physical layer only, since doesn't carry information originating from higher layers. Three uplink physical signals are defined in NR standard [11, Section 6.1.2].

- Demodulation Reference Signal (DM-RS) are used by the base station (gNodeB) for channel estimation purpose which are intended for coherent demodulation of

PUSCH. DM-RS are only transmitted being associated with PUSCH or PUCCH. They are are indicated by the green resource elements shown in Fig.3.12.

- Phase-Tracking Reference Signals (PT-RS) can be considered as an extension to DM-RS for PUSCH demodulation and intended for compensation of phase variation across the transmission duration [30, Chapter 9.11.3].
- Sounding Reference Signal (SRS) are intended to be used by base station (gNodeB) for channel-state estimation which supports the channel propagation dependent scheduling and link adaptation.

3.5.2 Downlink physical channels and procedures

Downlink physical channels defined in NR standard are Physical Downlink Shared Channel (PDSCH), Physical Broadcast Channel (PBCH), Physical Downlink Control Channel (PDCCH)[11, Section 7]. PDSCH set resource blocks to unicast user data and paging information carried by DL-SCH transport channel information transmitted from higher layers. In NR, the only control channel, PDCCH map resources to DCI. The principles of PDCCH processing in NR is similar to LTE. PBCH is used to carry information required by user device to access the network during cell search procedure. The PDSCH signal process flow is described in the following Section.

Downlink physical signals

Downlink physical signals correspond to a set of resource elements used by the physical layer only, since doesn't carry information originating from higher layers. Five downlink physical signals are defined in NR [11, p. 7.1.2].

- Demodulation Reference Signal (DM-RS) contained in PDSCH (DM-RS are indicated by the green resource elements shown in Fig.3.12) are intended for channel estimation purpose that enables coherent demodulation of the user device [30, Chapter 9.11].
- Phase-Tracking Reference Signals (PT-RS) can be seen as an extension to DM-RS for PDSCH demodulation and intended for compensation of phase variation across the transmission duration [30, Chapter 9.11.3].
- Channel State Information Reference Signal (CSI-RS) are set to be used by the user device to acquire channel state information.
- Synchronization Signal (SS) (Primary and Secondary) are used to enable the user device to find a cell when entering a system or to find a new cell moving with in a system. Primary Synchronization Signal (PSS) and Secondary Synchronization

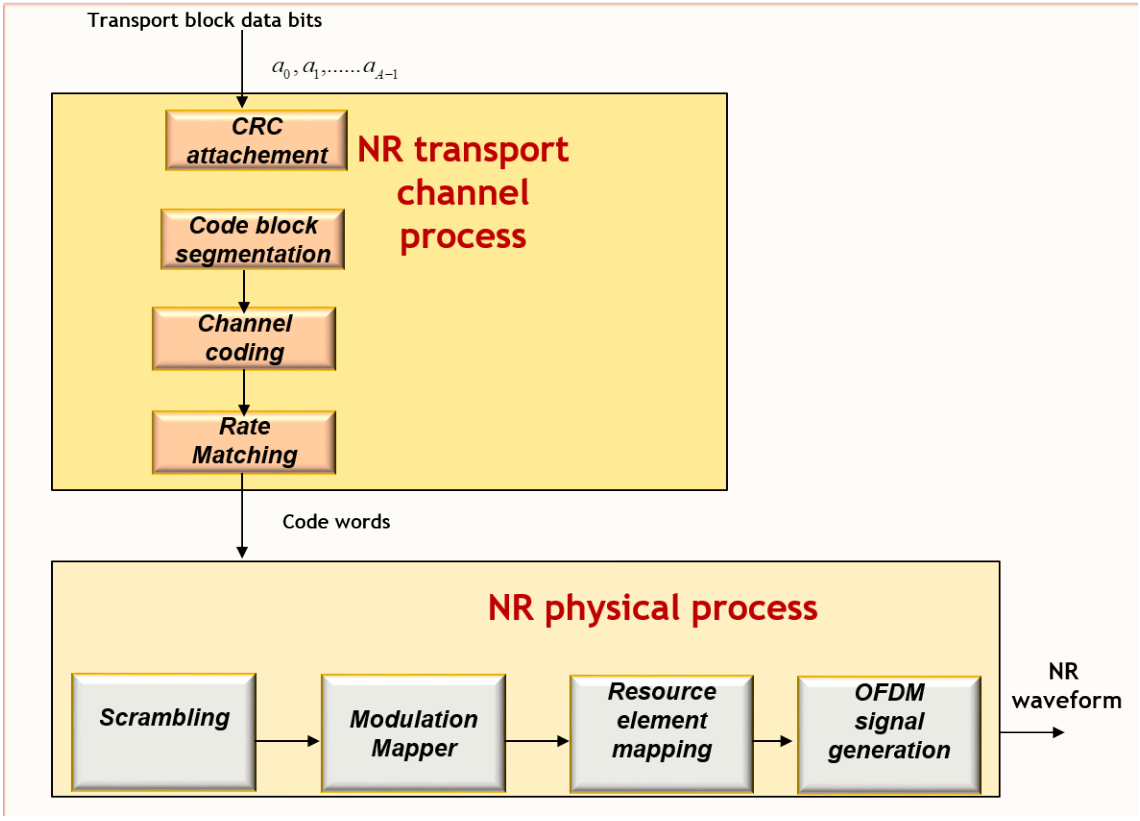

Figure 3.13: NR physical channel processing.

Signal (SSS) carried in PBCH are transmitted periodically in each NR cell[30, Chapter 9.11.3].

NR channel processing

In 5G NR technology, OFDM multiplexing scheme is used in both uplink and downlink transmission. Therefore, similar signal processing flows can be used for both directions. Fig. 3.6 outlines the simplified signal processing flow applied as a combination of NR transport channel process (UL-SCH/DL-SCH) and NR physical channel process (PUSCH/PDSCH) on a single carrier frequency transmission and one antenna port.

As in LTE, resource scheduling in NR is done on subframe basis. Therefore in every transmission time interval (TTI) there is at most one transport block provided from/to the MAC layer that are used encode/decoded data transport services over the radio transmission link. NR physical channel signal processing flow is described in the following Sections.

CRC attachment

Cyclic Redundancy Check (CRC) is the first step considered in the physical layer transport channel processing. It is calculated and attached on each transport block. For transport blocks size larger than 3824 bits, a 24-CRC (24 parity bits)is used. Otherwise 16-CRC (16 parity bits) is used [12, Section 5.1].

Code block segmentation

The Low Density Parity Check Matrix Moding (LDPC) channel coding specified in NR[12, Section 5.2.2] limits the maximum number of code block size input as 8448 bits for base graph 1 (BG1) and 3840 for base graph2 (BG2). If the defined code block sizes are larger than the maximum. The code block including the CRC is segmented (divided) into equal sized code block and an other CRC is attached on the segmented code blocks.

Channel coding

Channel coding scheme defined for UL-SCH /DL-SCH transport channel is based on LDPC. This codes invented the first time in 1963[39] have been ignored for many years since they were thought to be impractical. Nowadays LDPC are exposited to be implementation on high code rate applications. The performance of LDPC coder is similar to that of turbo coding with implementation advantages. The encoding of turbo codes in LTE, inherently gives rate 1/3 codes. However, higher coding rates are achieved by removing (puncturing) parity bits and by subsequent transmission of the punctured bits. The LDPC codes in 5G NR consists of higher coding rate (core) and an extended sequence of parity bits that can be appended to a lower the code rate. When these bits are not transmitted, they can be eliminated entirely from the decoding process. Hence, the number of decoding operation increases with respect to the transmitted block size of the code rather than the information block length. Consequently, the throughput of the LDPC decoder increases with the code rate [88].

The LDPC codes are commonly represented based on parity check matrix (PCM) and a graphical description known as tunnel graph which mirror the parity check matrix. The tunnel graphs are bipartite graph (BPG) where variable nodes corresponds to bits in the code word and the other set of nodes consisting of check nodes corresponds to the parity check where the bits must satisfy $Hc^T = 0$. Thus variable node ($m = N - K$) represented by the column of the parity check matrix and the check node is corresponds to the row(N)[88]. Thus an LDPC code with (N, K) representation as Fig3.14 can give wide range of properties including the code rate, which is one of the reason why base graph is used in NR specification.

Designing a good LDPC code is literally mean to find a sparse (sparseness of the matrix implies simpler decoding operation.) parity check matrix H. This can

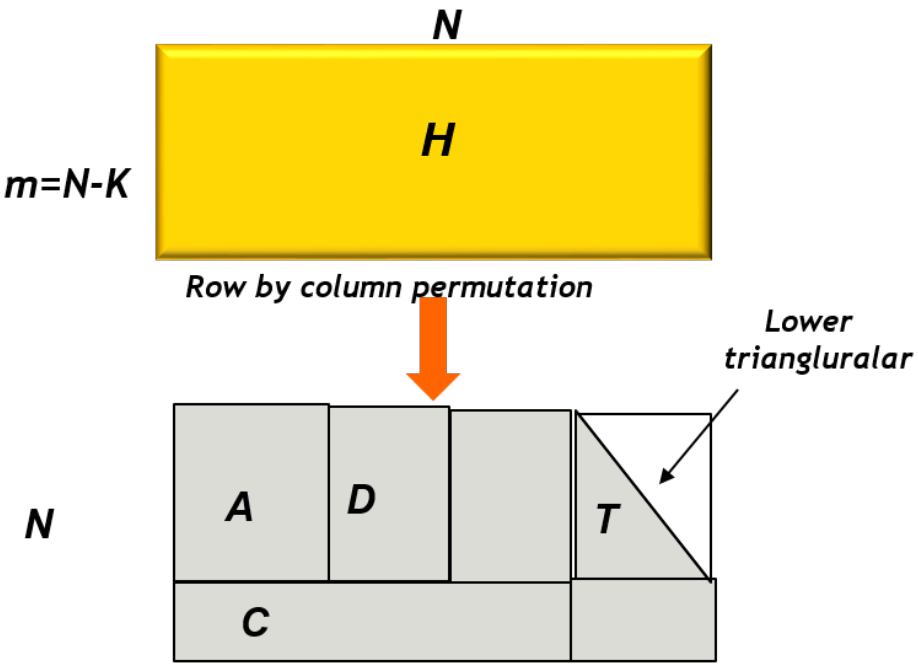

Figure 3.14: Base graph for LDPC encoder.

be obtained by reducing the parity check matrix to lower triangular form using column and row permutation designed to preserve the sparseness of the matrix as shown in Fig3.14[97]. Quasi-cyclic code with a dual diagonal structure of the kernel part of the parity check matrix are used in NR specification which gives a decoding complexity which is linear in number of coded bits and enables simple encoding operation .

Parity check matrix H in NR, can be obtained by BG, shift size Z and shift coefficients. The LDPC codes for NR, supports flexible information block size (maximum of 8440), Z for expansion $Z_{max} = 384$ and filler bits.

Two base graphs are defined in NR as BG1 and BG2 [12] which are designed for better performance optimization and improved decoding latency with in predefined code block length and code rates.

- BG1 is mainly designed for code block size ranges 300-8448 bits and code rates range $\approx$ 8/9-1/3. Further lower rates performance can be achieved via repetition.
- BG2 is mainly designed for block code size ranges 40 - 3840 bits, code rates between $\approx$ 2/3 - 1/5, and further lower rates via repetition.

The detail of the parameters to be used in BG1 and BG2 are described in [12, Table 5.3.2-2 and 5.3.2-3] respectively.

Rate matching

Rate matching in NR is used to extract coded blocks from the LDPC code with the desired code rate. Bit selection from the transmitter side circular buffer depends on the redundancy version (RV) index as in LTE 3.3.1. In this case the circular buffers are filled with an ordered sequence of systematic and parity bits. Each RV enables the receiver to know where the received packet started in the circular buffer and allows to perform appropriate soft-combination operation[44].

Scrambling

Similar to LTE, Scrambling applied to the coded bit imply multiplying the (exclusive-or operation) by a predefined scrambling sequence of bits. The scrambling codes in both PDSCH and PUSCH depends on the identity of the user device.

Modulation Mapper

The modulation mapper transform the block of scrambled bits to the corresponding block of complex modulation symbols. The supported modulation format in NR uplink and downlink transmission are QPSK, 16 QAM,64 QAM and 256 QAM.

Resource mapping

The purpose of the resource mapping is to distribute(map) the modulated symbols as an amplitude of the selected subcarriers.

OFDM signal generation

An N point IFFT, transform the complex subcarrier amplitude to a complex time domain signal. Every point in IFFT modulate modulates a single subcarrier and the summation of the over all modulation is transmitted sequentially as an OFDM signal. Cyclic prefix is inserted and transmitted serially as in LTE.

3.6 Chapter summary

This Chapter describes an overview of the physical layer specification of LTE and 5G NR radio access network technology. The Chapter mainly focuses on the understanding the basic structure of the physical channel and the baseband signal processing flow used to generate the physical channels. The first part of Chapter briefly review the principle of multicarriers OFDM transmission schemes implemented in the realization both LTE and 5G NR technology. It then outlines the physical layer channel structure of LTE with description of the time domain frame

structures, the time-frequency resource grid representation and the dynamic bandwidth allocation parameters. The simplified baseband signal processing flow implementation of uplink (PUSCH) and downlink (PDSCH) channel splited as transport channels processing such as CRC attachment, code block segmentation, channels coding, rate matching and physical process such as scrambling, modulation mapper, resource element mapping and OFDM/SC-FDMA signal generation of LTE is elaborated.

The second part of the Chapter outlines the 5G NR physical layer structure including the understanding of the 5G NR numerologies based on scalable subcarrier spacings and the corresponding time and frequency domain frame representation. The simplified baseband signal process chain similar LTE is described in the context of 5G NR technology for the uplink and downlink physical channel generation.

Chapter 4

DSP techniques for aggregation of LTE and 5G NR waveforms

4.1 Motivation

The very high demand for mobile data caused by new wireless technologies such as coordinated multi-point (CoMP), carrier aggregation, and massive-MIMO with a large throughput capacity has led to significant challenge to the existing optical and wireless access networks. C-RAN architecture enhances the capacity and coverage of radio access networks by centralizing signal processing and higher layer functionalities at the central office, and supervise remote radio heads (RRH) cooperatively. The transport of radio signal over fiber known as fronthaul, is a crucial network element in C-RAN scenario. Mobile fronthaul are usually categorized as digitized radio-over-fiber (D-RoF) and analogue radio-over-fiber(A-RoF).

The motive of this Chapter is to discuss the novel digital signal processing (DSP) techniques for aggregation of LTE and 5G NR radio waveforms on A-RoF architecture using Time Division Multiplexing Access (TDMA) [68] and Frequency Division Multiplexing Access (FDMA)[69].

This Chapter and the following presents the original work carried out during the entire PhD activity. The PhD work focuses on the comparison between DSP based TDMA and FDMA aggregation techniques in mobile fronthauling.

4.2 TDMA DSP

The transmitter and receiver side Digital Signal Processing (DSP) blocks based on time division multiplexing access (TDMA) is shown in Fig. 4.1. The transmitter DSP at the central office is used to aggregated and the receiver DSP at the remote antenna site is used for de-aggregation of advanced radio waveforms. The details of each DSP functional blocks will be described in the following Subsections.

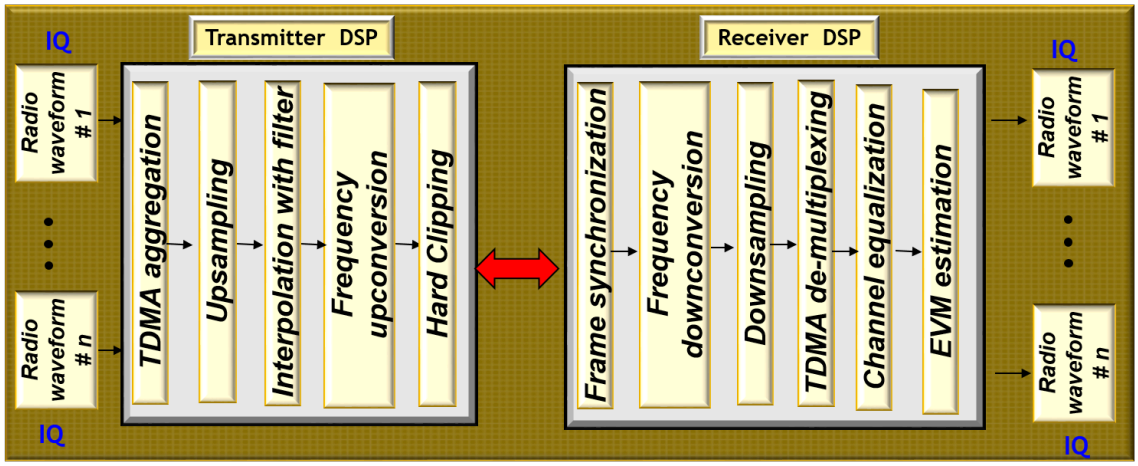

Figure 4.1: TDMA DSP setup.

Radio waveforms

The radio waveforms considered to be aggregated are 4G LTE and 5G NR waveforms, where the procedure for the generation of these radio waveforms are descried in Chapter 3. Aggregation of n 20-MHz LTE waveforms with a sampling rate 30.72-MHz and n 5G NR signals each with scalable bandwidth ranges both in uplink and downlink are considered in this Thesis. In the cases of 5G NR waveforms, generation up to n waveforms each with the bandwidths $50-MHz$, $100-MHz$, $200-MHz$ and $400-MHz$ are considered for the realization of DSP based channels aggregation.

4.2.1 TDMA transmitter DSP

The signal evolution of TDMA aggregation scheme for the transmitter DSP is described as follows.

TDMA aggregation

The complex samples of each radio waveforms are aggregated based on time domain (TD) symbol wise cascaded approach, which is an interleaving of time domain samples. An example of Time Domain Multiplexing (TDM) of the first 3 20-MHz LTE waveforms which are cascaded into one steam is shown in Fig.4.2. A cascade of n waveforms in time can be represented as

$$X(t) = \sum_{ch=1}^{n} x_{ch}(t), \tag{4.1}$$

where $X(t)$ is a stream of cascaded waveforms and $x_{ch}(t)$ denotes the time

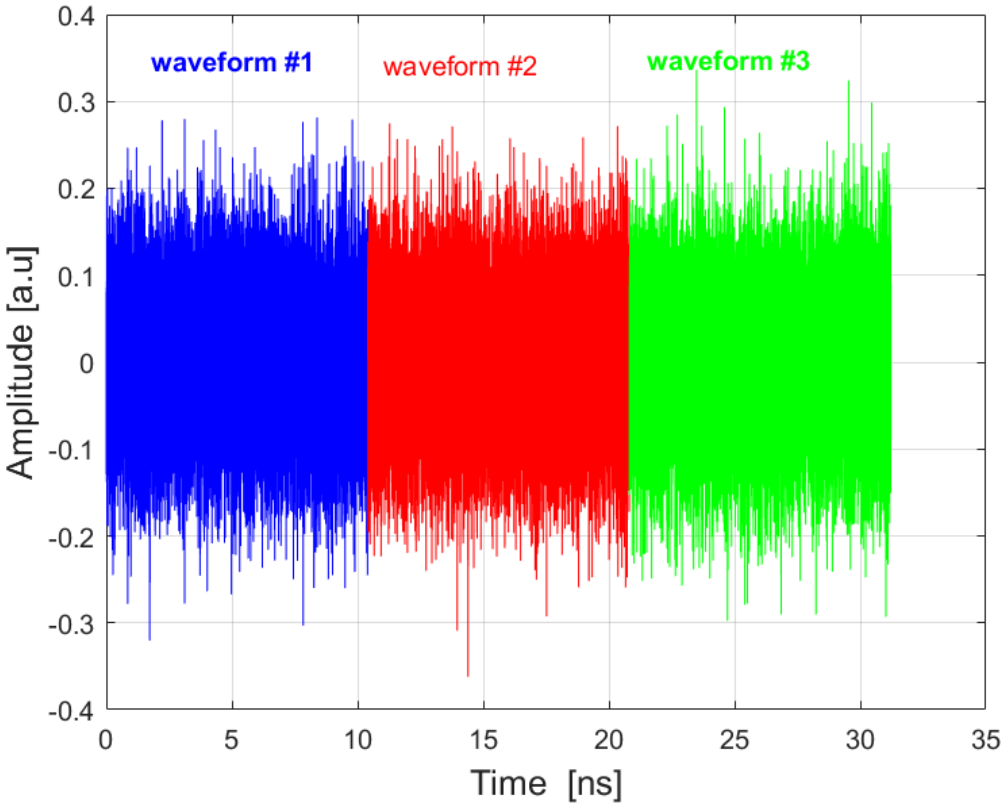

Figure 4.2: Example of 3 20 MHz LTE waveform TDM.

domain representation of ch^{th} channel (waveform) defined by the OFDM signal representation (downlink LTE) as in (3.3).

A spectrum of a single baseband 20-MHz LTE waveform with sampling rate $fs = 30.72$-MHz (shown in Fig.4.3a). The spectrum for aggregation of 48 20MHz LTE waveforms in TDM is shown in Fig.4.3b. The TDM cascade stretches the bandwidth $n = 48$ times in frequency as shown in Fig.4.3b and accumulates the OFDM symbols in time[109].

The aggregated signal $X(t)$ shown in Fig.4.3b is band limited in its Fourier transform $X(f)$, which is zero outside the interval $(-T_{BW}/2 < f < T_{BW}/2)$. The total signal bandwidth can thus be obtained as $T_{BW} = n \cdot BW$, where n is the number of aggregated waveforms and BW is the bandwidth occupied by each waveforms as computed in Eq.3.1. Hence the total bandwidth T_{BW} of the 48 20-MHz LTE waveforms shown in Fig.4.3b is 960-MHz.

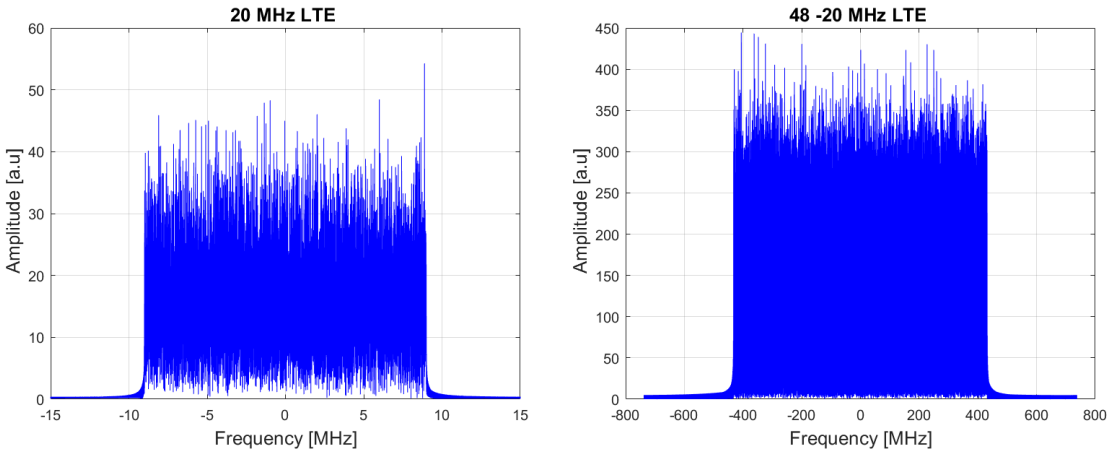

(a) Single 20MHz LTE waveform spectrum. (b) 48 20MHz LTE TDM spectrum.

Figure 4.3: TDM spectrum.

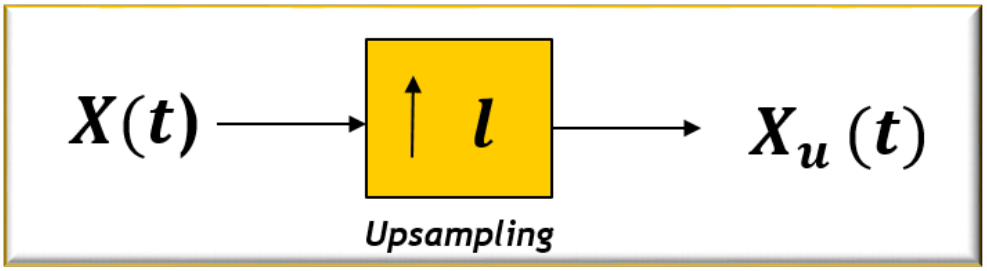

Figure 4.4: upsampling.

Upsampling

Upsampling of the time domain aggregated complex signal (X(t)) is required to fit with the DAC sampling rate used in our experimental model. Upsampling to a higher (l times) sampling rate can be implemented by inserting $l-1$ zeros between each in phase and quadrature (IQ) complex samples. The system level diagram for upsampling is shown in Fig. 4.4. The upsampled signal is effectively scales the time axis by a factor l as $X_u(t) = X(t/l)$.

The upsampling of $X(t)$ can be viewed as a product of $X[t]$ with a periodic train of unit impulse function as

$$X_u(t) = X(t/l) = \sum_{k=-\infty}^{\infty} X[(k) \cdot \delta(t - l \cdot k)]. \tag{4.2}$$

Applying the frequency convolution property of Fourier transform, the time domain product of Eq.4.2 can be transformed into frequency domain convolution[95, Chapter 2], which results $X_u(f)$ as in Eq.4.3.

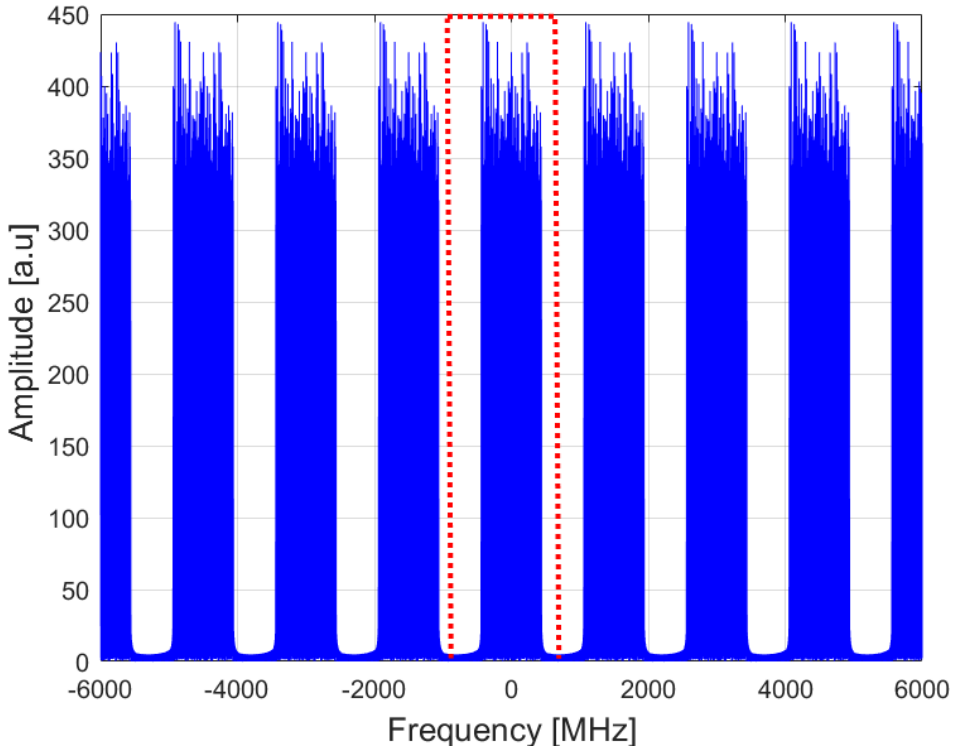

Figure 4.5: Upsampled TDM aggregated waveform with upsampling factor l=8 to 12 GSa/s.

$$X_u(f) = \frac{l}{T_s} \sum_{t=-\infty}^{\infty} \left(\sum_{k=-\infty}^{\infty} X[k] \cdot \delta[t - l \cdot k] \right) e^{-j2\pi ft} = X(l \cdot f), \tag{4.3}$$

where T_s is the period of the aggregated input signal. In addition, the spectrum replicates itself periodically in frequency every $1/T_s$. Choosing a sampling rate l/T_s with a Nyquist criterion that is $l \cdot fs \geq 2T_{BW}$, the original waveform can be recovered by using low pass filter. Since in our experiments we had an Arbitrary Waveform Generator (AWG) running at 12 GSa/s, the typical upsampling parameters are $fs = 48 \cdot 30.72MHz$ for the lower sampling rate of the input signal shown in Fig.4.3b and upsampling factor $l = 8$. Fig.4.5 shows the input signal upsampled (l=8) to 12 GSa/s.

Interpolation with filtering

Interpolation filter is used to remove all replicas (images) of the signal transform except the original signal shown by the red dot lines on the Fig.4.5. Proper choice of the filter parameter leads to an interpolation between the non-zero samples of

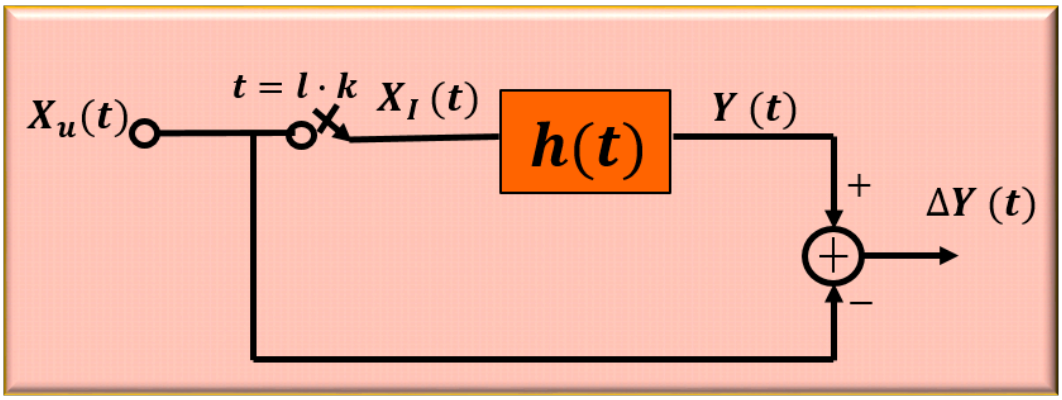

Figure 4.6: General block diagram of interpolation filter.

sequences, hence creates a smoothly varying samples. This can be realized by using digital Interpolated Finite Impulse Response Filter (IFIR)[78]. For the input sequence $\{X_u(t)\}$ Eq.4.2, the interpolated output values are different from zero for $t = l \cdot k$ where l is an upsampling factor greater than 1 (integer) and $k = 0, \pm 1, \pm 2...$.

$$X_I(t) = \begin{cases} X_u(t) & \forall\, t = l \cdot k \\ 0 & otherwise \end{cases}$$

General block diagram of an interpolator filter is shown in Fig.4.6. Considering finite duration filter, the degree of the filter has to be designed as $n = 2l \cdot L$ where L is the stretching or interpolation factor that needs to be chosen with respect to the efficiency and the functionality of the filter. For low pass interpolation finite impulse response (IFIR) filter, the maximum interpolation factor L is determined as function of stopband frequency, ω_s as [77].

$$L_{max} = \lfloor \frac{\pi}{\omega_s} \rfloor. \tag{4.4}$$

The floor in Eq.4.4 guarantee the stopband frequency is less than π.
The filter output can be described as the convolution:

$$Y(t) = \sum_{u=-l \cdot L}^{l \cdot L} h(u) \cdot X_I(t-u), \tag{4.5}$$

where $h(u)$ is the impulse response of the filter. In frequency domain it is described as

$$H(f) = \begin{cases} T & if\ |f| \leq \frac{f_s}{2} \\ 0 & otherwise \end{cases}$$

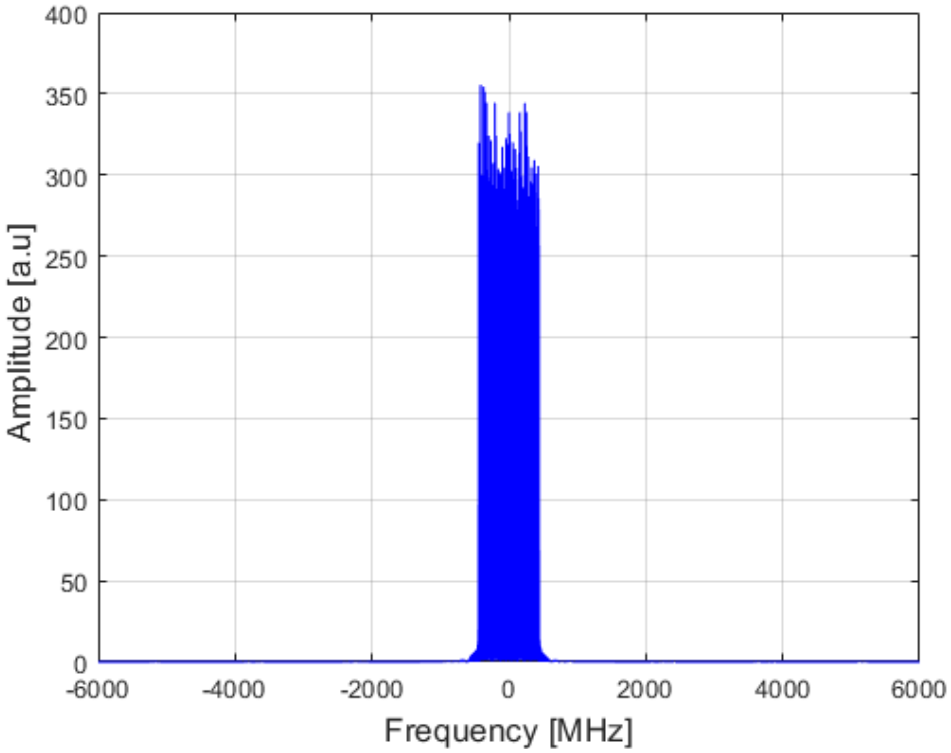

Figure 4.7: Interpolated upsampled waveform.

where T is the filter gain, f_s is the sampling frequency of the filter. From the multiplication property relation of frequency transform and convolution in time domain, the frequency domain filter output (4.5) will be

$$Y(f) = H(f) \cdot X_I(f). \tag{4.6}$$

The upsampled aggregated waveform depicted in Fig.4.5 is filtered by using IFIR and the resulting filtered waveform is shown in Fig.4.7.

Frequency upconversion

Frequency upconversion of the upsampled complex aggregated waveform is required to generate a real output signal which is used to drive the Mach-zehnder modulator (MZM) RF input in the IM-DD setup. The frequency upconversion can be obtained by using linear IQ modulation method which is basically multiplying the complex signal by complex exponential (IQ mixing) and talking the real part[101]. Consider the complex signal $Y(t) = Y_I(t) + j \cdot Y_Q(t)$, it is modulated (upconverted) in two orthogonal cosine and sine carriers as in Eq.4.8 .

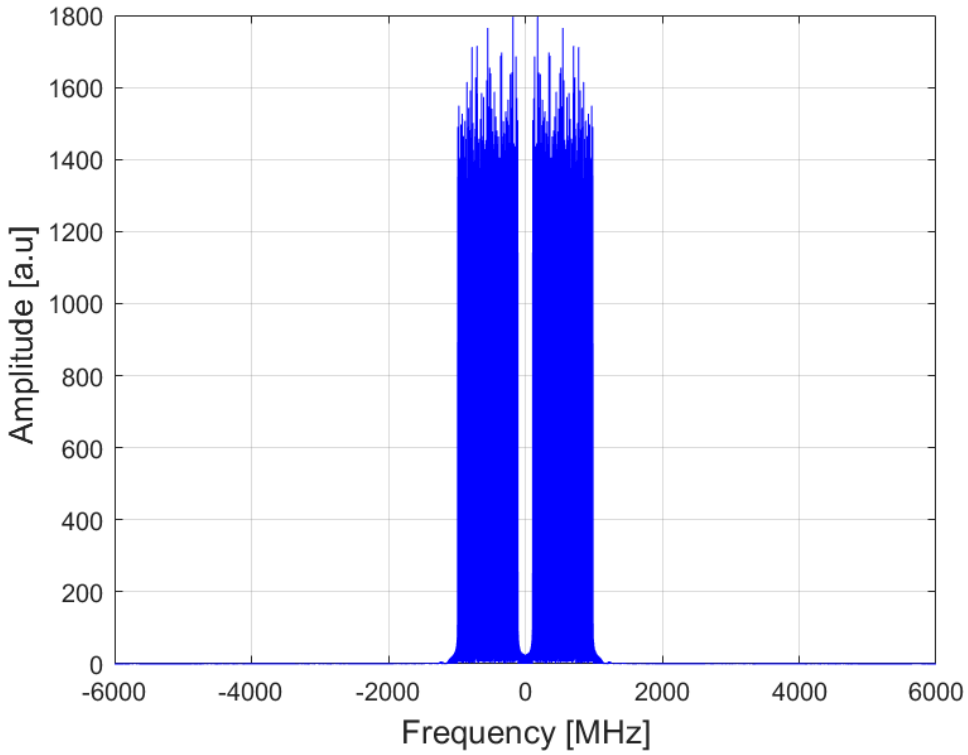

Figure 4.8: Frequency upconverted real signal.

$$Y_{up}(t) = Re[Y(t) \cdot e^{j2\pi f_c t}] = Y_I(t) \cdot \cos(j2\pi f_c t) - j \cdot Y_Q(t) \sin(j2\pi f_c t) \tag{4.7}$$

$$= \frac{1}{2}\Big(Y(t) \cdot e^{j2\pi f_c t} + Y(t)^* \cdot e^{-j2\pi f_c t}\Big), \tag{4.8}$$

where f_c is the desired carrier frequency. The spectral components at $-f_c$ and f_c contains the original information $Y(t)$. The frequency upconverted real output of the complex interpolated upsampled waveform is depicted in Fig.4.7, which is upconveted (shifted) to the carrier frequency $f_c = BW/2 + Gauard\ interval(GI)$. f_c selected for the 48 20-MHz LTE is selected as $960/2MHz + 70MHz = 550MHz$ and its real output signal is shown in Fig.4.8.

Hard clipping

All the consideration in this section on hard clipping based on OFDM signal is also valid for the the aggregated signal (that is not strictly speaking an OFDM). An OFDM signal as a summation of many subcarriers has approximately Gaussian probability density function in the time domain (thanks to Central Limit Theorem)

with a large dynamic range that may lead to high Peak-To-Average-Power Ratio. Therefore, the receiver detection performance is very sensitive to nonlinear devices used in the IM-DD setup, such as DAC and MZM. An electrical domain OFDM signal is transported into optical carrier by using MZM. The nonlinear MZM has a sinusoidal electrical to optical power transfer characteristics that may restricts the signal to occupy a narrow dynamic range in the linear region of the transfer function. As a result of the high PAPR with low average power causes nonlinear distortion that impairs the performance of the receiver. One of the signal distortion techniques used to reduce the high PAPR is signal clipping[22]. The hard clipping implemented on the real bandpass output signal with the variance $\delta^2_{Y_{up}}$ normalized to 1 as shown in 4.9 is described based on Eq.4.9.

$$Y_c(t) = \begin{cases} -R_{cl} & if \ Y_{up}(t) < -R_{cl} \\ Y_{up}(t) & if \ -R_{cl} < Y_{up}(t) < R_{cl} \\ R_{cl} & if \ Y_{up}(t) > R_{cl} \end{cases} \tag{4.9}$$

The clipping level in logarithmic scale dB (commonly used) can be described as (4.10)

$$R_{cldB} = 20 \cdot \log_{10} \left(\frac{R_{cl}}{\delta^2_{Y_{up}}} \right). \tag{4.10}$$

Due to the fact that the OFDM has dense subcarrier, hard clipping causes frequency leakage across subcarriers and in-band distortion[66]. There is a trade off between the noise incorporated due to clipping with the effect of performance degradation due to out of band distortion and the performance improvement with lower PAPR. A small value of R_{cl} (strong hard clipping) gives rise to a large electrical signal but also a large clipping distortion, while small value of R_{cl} can reduce(almost completely) the signal distortion, but in turn generates a small signal that is less resilient to receiver noise. Therefore, an optimum clipping R_{cl} has to be found experimentally.

4.2.2 TDMA receiver DSP

The DSP flow associated with the TDMA de-aggregation of the receiver DSP is described in the following Sections.

Frame synchronization

Frame synchronization is an algorithm that is used to approximately estimate the received aggregated signal frame start position in time domain. A periodic training symbol in time domain is provided by the transmitter to point out the start of the frame and robust time synchronization. The algorithm proposed by Timothy Schmidl and Donald Cox [90], is exploited to find both timing (estimation

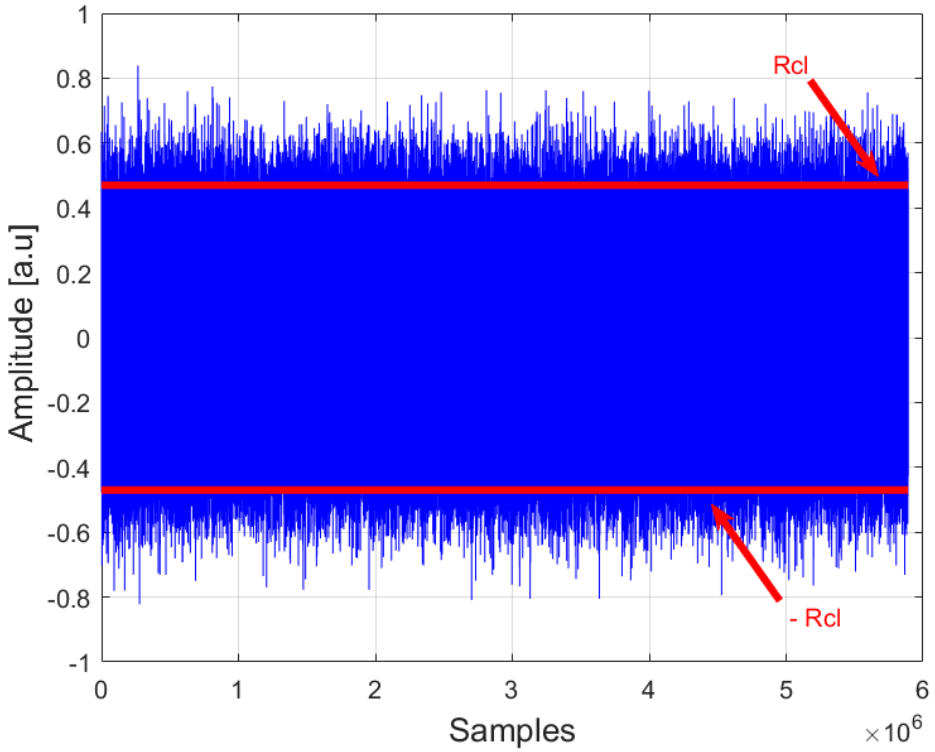

Figure 4.9: Hard clipping.

of frame start in time domain) and frequency offset estimation. Considering the received signal $Y_{rx}(t)$ with a delay and additive white Gaussian noise (AWGN) channel as

$$Y_{rx}(t) = Y_c(t - \tau) + n(t), \tag{4.11}$$

where τ is the unknown delay to be estimated at the receiver and $n(t)$ is AWGN noise. The time delay estimate $\hat{\tau}$ can be obtained by feeding $Y_{rx}(t)$ to a sliding window cross correlation lag N (the size of the periodic training reference symbol). The peak tells where the sliding widow is aligned with the reference signal which consequently reveals the start of the frame. $\hat{\tau}$ can be obtained as (4.12)

$$\hat{\tau} = \underset{\tau}{\operatorname{argmax}}\{R(\tau)\}. \tag{4.12}$$

$R(\tau)$ is the cross correlation function of lag N normalized to the received signal power as

$$R(\tau) = \frac{\sum_{l=\tau}^{\tau+N-1} Y_{rx}(l+N) \cdot Y^*_{train}(l)}{\sum_{l=\tau}^{\tau+N-1} |Y_{rx}(l+N)|^2}, \tag{4.13}$$

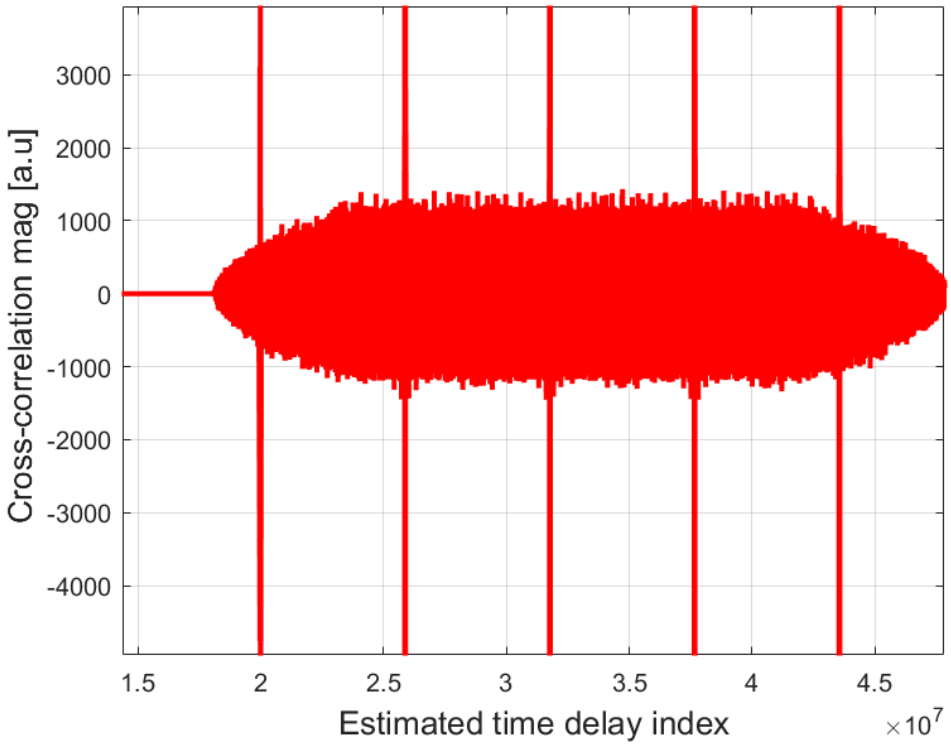

Figure 4.10: Cross correlation evaluated for frame synchronization.

where Y_{train} is the periodic training reference symbol. Fig.4.10 shows the $R(\tau)$ of the received aggregated 48 20- MHz LTE waveforms (which is taken as an example). The frame replicas are due to the fact that the signal is acquired by the Real Time Oscillator (RTO) available in our experimental lab running at 40 $GSa/$. Consequently the peaks tells the beginning of frame index of the replicas.

Frequency downconversion

The received real band pass signal is downconverted to complex baseband signal by using IQ demodulation which is a method used to recover the original message $Y(t)$ from the modulated signal Y_{up} Eq.4.8. Considering the $Y_{syn}(t)$ signal after frame synchronization, downconversion is obtained as

$$Y_{dc}(t) = 2 \cdot Y_{syn}(t)e^{-j2\pi f_c t} = \Big(Y(t) \cdot e^{j2\pi f_c t} + Y(t)^* \cdot e^{-j2\pi f_c t} + n(t)\Big)e^{-j2\pi f_c t}$$

$$Y_{dc}(t) = Y(t) + Y(t)^* e^{-j4\pi f_c t} + \dot{n(t)}. \tag{4.14}$$

where Y_{dc} is the downconverted baseband signal. Ignoring clipping effect in Eq. 4.14 for clarity, the desired complex signal can be recovered by removing the high

frequency component in Eq. 4.14 by using an Interpolation with filtering or digital low pass filter that is used to pass signals lower than the designed cutoff frequency and removes (attenuates) signal above the cutoff frequency.

Downsampling

Downsampling the downconverted baseband signal to a lower (l times) sampling rate is required to recover the original sampling rate of the aggregated complex signal that was upsampled to fit with DAC sampling frequency. Dowsampling of a signal satisfying Nyquist criterion (without aliasing problem) by l times can be achieved by keeping only the l^{th} sample from the input signal ($Y_{dw}(t) = Y_{dc}(l \cdot t)$) as in Eq.4.15.

$$\begin{aligned} Y_{dw}(f) &= \sum_{m=-\infty}^{\infty} (Y_{dc}(l \cdot m)) e^{-j2\pi f m} \\ &= \sum_{n=-\infty}^{\infty} Y_{dc}(n) \sum_{k=-\infty}^{\infty} \delta(n - mk) e^{-j2\pi f \frac{n}{l}}|_{n=lm} \end{aligned} \tag{4.15}$$

Applying the convolution property of the Fourier transform, Eq.4.15 can be rewritten (the detail passage is found on [61]) as in Eq.4.16.

$$Y_{dw}(f) = \frac{1}{l} \sum_{k=0}^{l-1} Y_{dc} e^{-j2\pi f \frac{k}{l}}. \tag{4.16}$$

The frequency spectrum of the received aggregated waveforms (48 20-MHz LTE) downsampled to the baseband sampling frequency is shown in Fig. 4.11.

TDMA de-multiplexing

The downsampled aggregated signal de-multiplexed (de-aggregated) in time to recover the individual radio waveforms. An example for de-multiplexing of 3 20-MHz LTE waveforms is shown in Fig.4.12. where each waveform is de-interleaved in the dedicated time interval.

Channel equalization

Channel equalization at the receiver is required to compensate for the channel impairments (temporal time dispersion) that may lead to inter-symbol and inter carrier interferences. Since OFDM signal is affected by frequency selective channel, the subcarrier spacing (bandwidth) of the radio waveforms (LTE and 5G NR) are designed to be smaller than the channel coherence bandwidth. This potentially gives a flat fading on each subcarrier that can be described by a single complex multiplication so that equalization can be achieved with one tap. The impulse response of the channel can be obtained by inserting training sequence of one OFDM

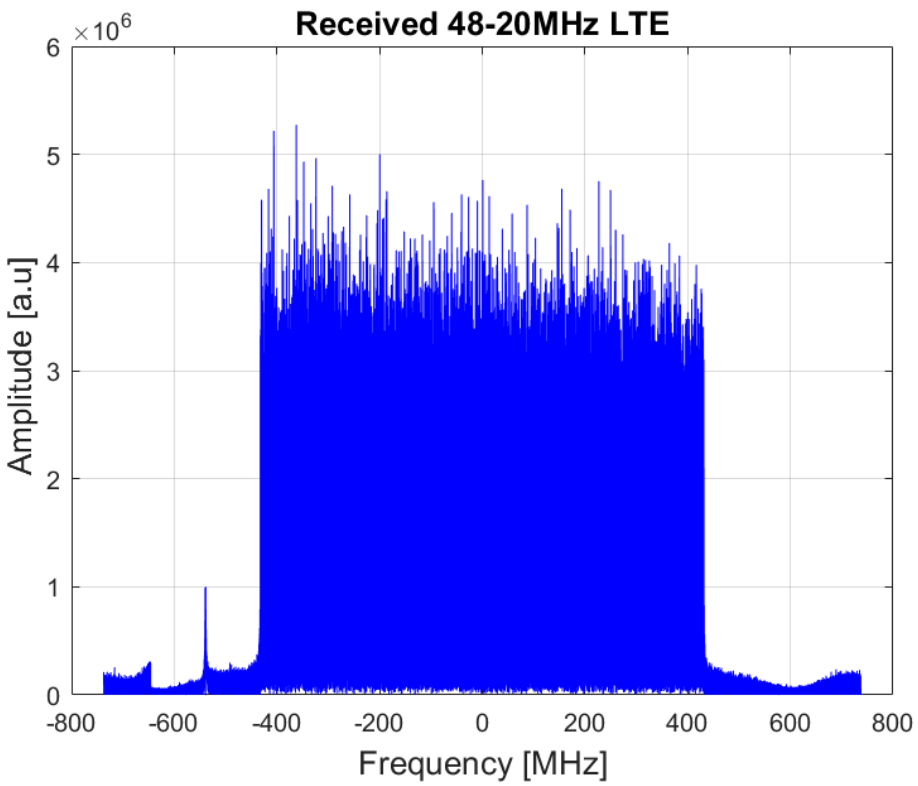

Figure 4.11: Downsampled aggregated waveforms.

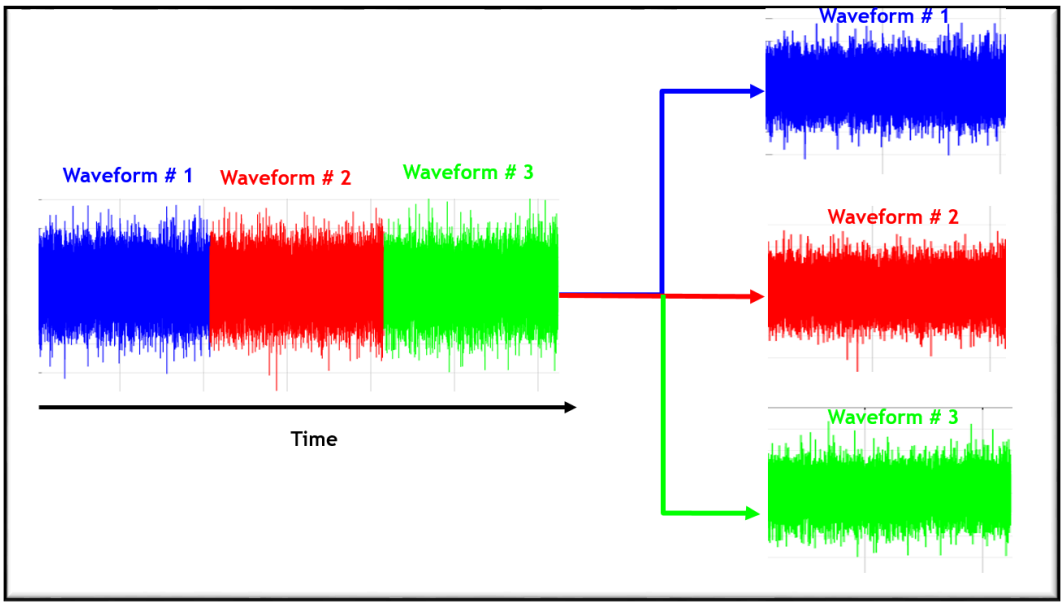

Figure 4.12: Time domain de-multiplexing of 3 20-MHz LTE waveforms.

length (N subcarrier) from the transmitter and known at the receiver hence all the subcarriers have information about the channel effect.

Let the time domain signal at the output of the transmitter associated with k^{th} subcarrier as

$$x(t) = X_k \cdot exp\Big(\frac{j2\pi kt}{N}\Big). \tag{4.17}$$

Since the channel frequency response on each subcarrier is different, the received signal is affected with different path gains h and time delay τ expressed as

$$y_(t) = X_k \cdot h \cdot \sum_{g=1}^{g_{max}} exp\Big(\frac{j2\pi k(t-\tau)}{N}\Big) + n(t) \tag{4.18}$$

where $n(t)$ is the noise factor at time t and g_{max} is the maximum path length. Considering g_{max} for simplicity, the frequency domain representation of Eq.4.18 can be written as

$$Y_k = X_k \cdot (h_1 + h_2 exp\Big(\frac{-j2\pi k(\tau_2 - \tau_1)}{N}\Big) + N_k$$

$$Y_k = X_k H_k + N_k \tag{4.19}$$

where $H_k = (h_1 + h_2 exp\Big(\frac{-j2\pi k(\tau_2-\tau_1)}{N}\Big)$. Since X_k is known at the receiver, the channel estimation for ideal noiseless channel can be obtained as

$$H_k = \frac{Y_k}{X_k}. \tag{4.20}$$

The phase shift (rotation) and attenuation due to channel effect can be recovered by a single complex multiplication (one tap equalize) as

$$\hat{X_k} = \frac{Y_k}{H_k} = X_k + \frac{N_k}{H_k}. \tag{4.21}$$

EVM estimation

Error Vector Magnitude (EVM) is the most common figure of merit for quantifying the quality of digitally modulated signals using QAM formats. Fig.4.13 depicts the received signal constellation for 64 QAM modulated signal and the error vector on the n_{th} symbol. The measured received symbol vector $S_{Rx,n}$ deviates from the transmitted symbol vector $S_{Tx,n}$ and the error vector on the n_{th} symbol is therefore estimated as a vector difference $err_n = S_{Rx,n} - S_{Tx,n}$[91].

The EVM estimation in its root mean square error for L randomly transmitted data can be obtained from Eq.1.4.

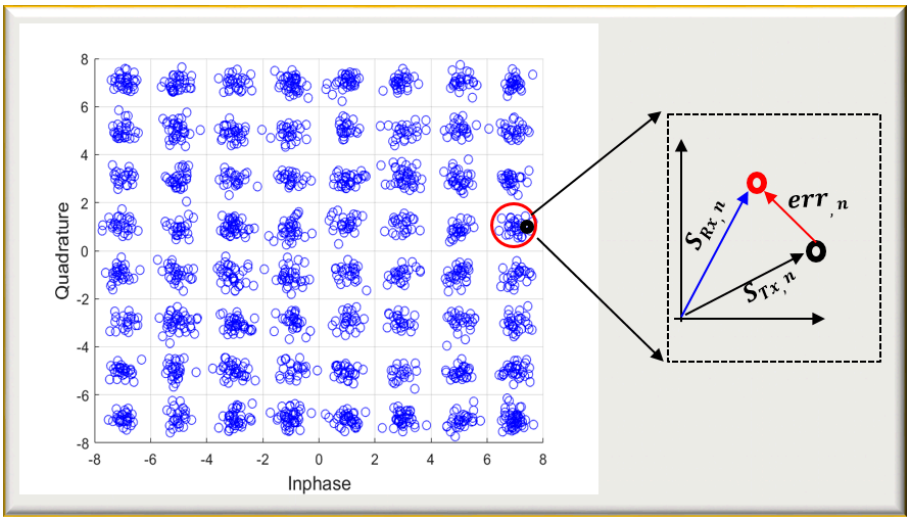

Figure 4.13: EVM estimation.

Alternatively, EVM can be estimated from the Signal-to-Noise Ratio (SNR) in AWGN channel[92]. SNR is the relative measure of the signal power with respect to the noise power commonly expressed as

$$SNR = \frac{E_s}{N_o} = \frac{\sum_{n=1}^{L} \mid S_{Tx,n} \mid^2}{\sum_{n=1}^{L} \mid S_{Rx,n} - S_{Tx,n} \mid^2} \tag{4.22}$$

The EVM_{rms} normalized to the power of the longest ideal constellation as computed as in Eq.1.4 can be rewritten as

$$EVM_{rms} = \left[\frac{\sum_{n=1}^{L} \mid S_{Rx,n} - S_{Tx,n} \mid^2}{\sum_{n=1}^{L} \mid S_{Tx,n} \mid^2}\right]^{\frac{1}{2}} \tag{4.23}$$

$$\approx \left[\frac{1}{SNR}\right]^{\frac{1}{2}} \tag{4.24}$$

Bit Error Rate (BER) is also an other importance performance metrics which is used to measure the probability of bit error $p_b(e)$ in terms of erroneous bits per the transmitted. BER can be estimated by comparing the decoded bit pattern of the received signal with a pre-defined transmitted reference bits. An estimation of probability of bit error $\hat{p_b}(e)$ can be obtained as the ratio of the number detected erroneous bits with the total number of transmitted bits. The estimate $\hat{p_b}(e)$ will approach the true $p_b(e)$ for large number of transmitted bits[85].

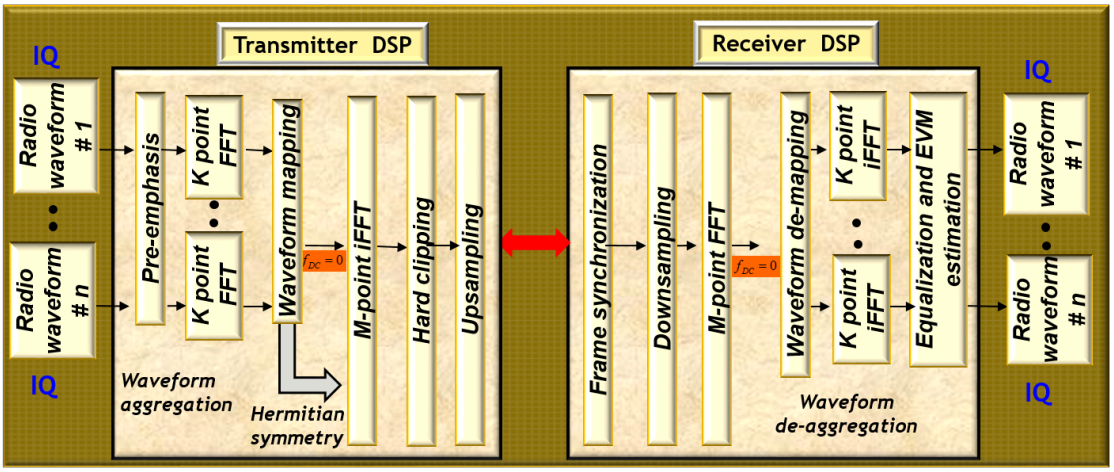

Figure 4.14: FDMA DSP setup .

4.3 FDMA DSP setup

The other alternative channel aggregation approach considered in this Thesis, the Frequency Division Multiplexing Access (FDMA) digital signal processing (DSP) setup for the aggregation of next-generation radio waveforms such as LTE and 5G NR is shown in Fig.4.14. The signal evolution from the transmitter DSP towards the receiver DSP will be described in the following Subsections.

Pre-emphasis

Pre-emphasis (pre-compensation) is a technique used to mitigate the power roll-off at high frequencies due to band limited IM-DD link and equalize the performance the FDMA aggregated waveforms over frequency. The equalization rule (pre-emphasis) involves multiplying each radio waveforms with a set of k globally optimized real coefficients (amplitude scaling factor), so that all radio waveforms shows similar performance behavior at the receiver end[99]. The pre-emphasis technique which consists the multipltiplication of the amplitude of each C_i waveforms by the amplitude scaling factor k_i is shown in the Fig.4.15, where i = 1,2...n and n is the total number of aggregated waveforms. Pre-emphasis technique applied based on the system frequency response such that the power change on the i^{th} channel [69] with respect to the first channel in dB is expressed as

$$\triangle P(i) = \frac{(i-1)}{n-1} \times P_{rolloff}\,[dB], \tag{4.25}$$

where $P_{rolloff}$ is the roll off power (power difference) of the last waveform with respect to the first in dB. The $P_{rolloff}$ value depends on the total number of aggregated channels n, the radio waveform type (LTE or 5G NR) and the corresponding

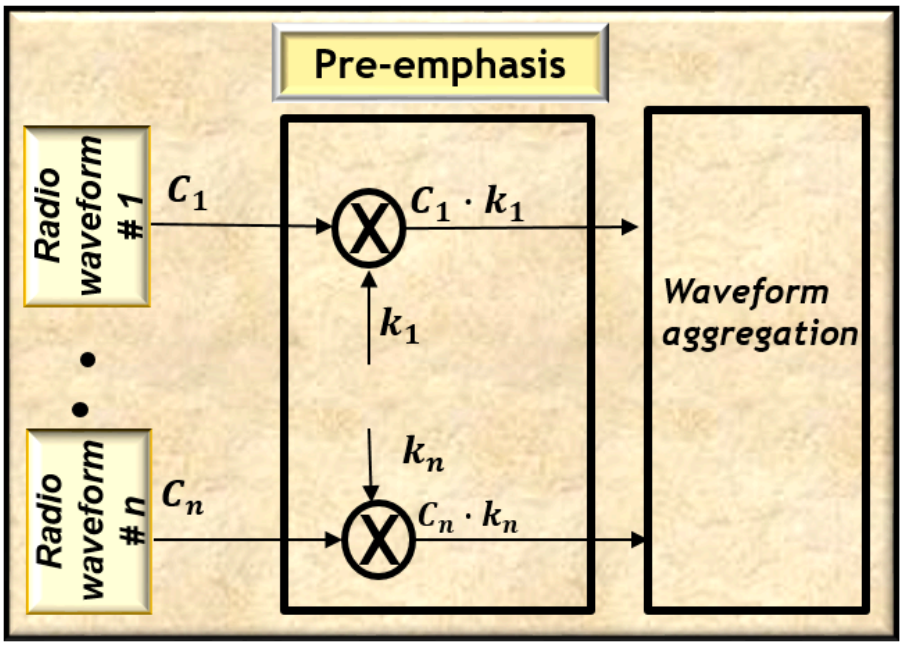

Figure 4.15: Pre-emphasis technique.

numerologies. For instance for the case of flat channel response with $P_{rolloff} = 0$ dB ($\triangle P(1) - \triangle P(n) = 0$ dB), consequently the amplitude scaling factors k_i of each waveform is set to 1.

Waveform aggregation

To achieve a high-capacity mobile fronthauling with a better spectral efficiency, the pre-compensated time domain radio waveforms are transformed into frequency domain using lower size K point FFT/IFFT. The optimum K size can be obtained as

$$k = N_{FFT,ref} \cdot \frac{\triangle f}{\triangle f_{bin,ref}}, \tag{4.26}$$

where $\triangle f$ is subcarrier spacing of the waveform to be aggregated, $\triangle f_{bin,ref} = 1.92MHz$ is the optimized reference frequency spacing or resolution of the aggregated signal and $N_{FFT,ref} = 2048$ is the reference FFT size aligned with LTE standard. For example k point for 20 MHz LTE ($\triangle f = 15KHz$) from Eq. 4.26 is set to 16 and similarly k for SCs type 1 ($\triangle f = 30KHz$) is 32.

The frequency domain waveforms after the k point FFT are mapped based on seamless channel mapping such that the center frequencies of the i^{th} channels after M point IFFT aggregation gives out to be

$$f_{center}(i) = i \cdot f_{samp}, \tag{4.27}$$

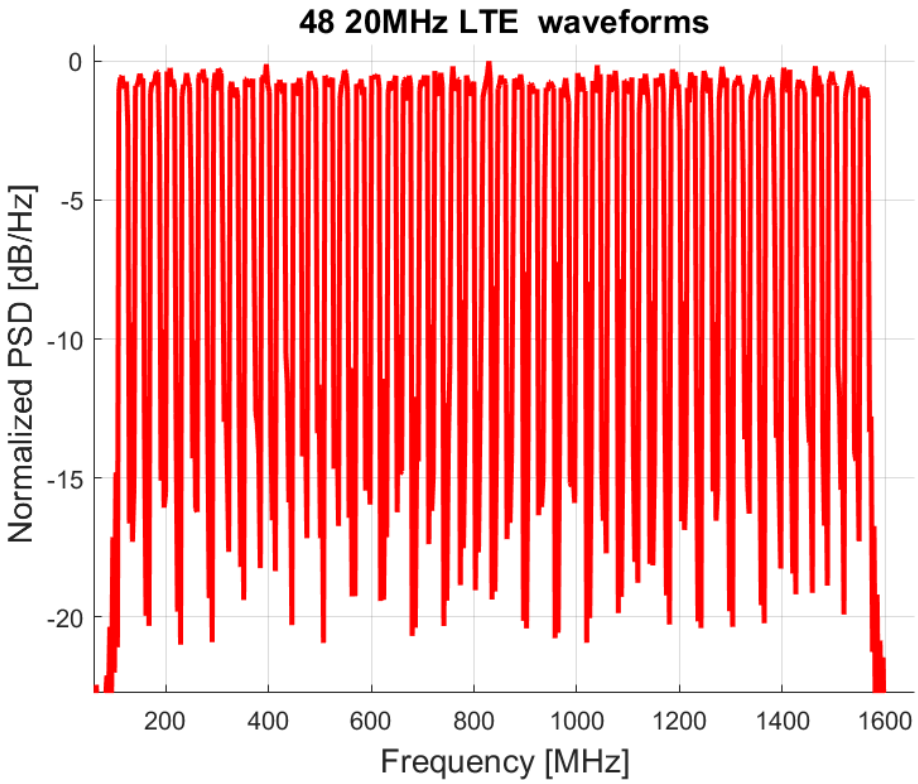

Figure 4.16: FDMA aggregation of 48 20-MHz LTE with parameters: $k = 16$, $M = 2048$ and $f_{bin} = 1.92MHz$.

where f_{samp} is the sampling frequency of the radio waveform such as LTE and 5G NR described on Table 3.1 and Table 3.4 respectively and $i = 1, 2, ...n$ (n is the total number of aggregated channels). Since a real valued aggregated signal output is required to to drive the RF input of the MZM, which directly modulate the intensity of the optical carrier. This corresponds to a Hermitian symmetry in the frequency spectrum of the mapped waveforms are feed to the half points (negative frequency range) of M-point IFFT.

The frequency resolution of the aggregated signal after that is used to align the center frequency of the aggregated signal as in Eq.4.27 can be obtained as

$$\triangle f_{bin} = \triangle f_{bin,ref} \cdot \frac{M}{N_{FFT,ref}}. \tag{4.28}$$

The M size depends on the number of channels and radio waveform types. For instance for 48 20-MHz aggregated LTE waveforms, $M = 2048$ and $\triangle f_{bin} = 1.92MHz$. The power spectral density of the aggregated 48 20-MHz LTE waveforms is shown in Fig.4.16.

Hard Clipping

To reduce the high PAPR, Hard clipping similar to TDMA DSP is applied on the real valued FDMA aggregated waveforms.

Upsampling

The clipped aggregated time domain signal is upsampled to higher sampling frequency that is required to fit with DAC sampling rate used in the IM-DD experiment ($12Gsa/s$). The same uplink DSP procedure is used as in TDMA DSP.

4.3.1 FDMA receiver DSP

The received digital signal at the receiver DSP shown in Fig.4.14 is processed to de-aggregate and recover the transmitted radio waveforms. The off-line receiver DSP blocks is described in the following Subsection.

Frame synchronization

Frame synchronization on the received aggregated waveform is used to identify the frame starting position of the acquired aggregated signal in time domain. Similar frame synchronization algorithm used in TDMA DSP is applied also for FDMA DSP.

Downsampling

Downsampling of the synchronized FDMA aggregated waveforms (OFDM frame) is used required to lower the sampling rated of the original baseband signal. The downsampling DSP is similar to the one used in TDMA DSP.

Waveform de-aggregation

The downsampled time domain signals are feed to M-point FFT. The first half (positive frequency range) points of the M point FFT output in frequency domain is used to de-map (de-aggregate) the waveforms and the time domain de-aggregated radio waveforms are recovered after the K point IFFT operation.

Channel equalization and EVM estimation

The effect of channel (optical) impairments such as phase shift (rotation) and attenuation on the de-aggregated radio waveforms can be recovered by using a one tap equalizer Sec.4.2.2 similar to the one used in TDMA DSP. The link performance measure on the radio waveforms is evaluated based on EVM estimation described on TDMA DSP.

4.4 Chapter summary

This chapter explains the off-line DSP techniques employed for aggregation/de-aggregation of radio waveforms (4G LTE and 5G NR described in Chapter 3) based on a novel TDMA and FDMA approaches. The details of the theoretical analysis and processing steps employed in the signal evolution of aggregation (transmitter DSP) and de-aggregation (receiver DSP) in each DSP blocks are elaborated for both TDMA and FDMA schemes.

Chapter 5

Experimental demonstration of DSP-aggregated fronthaul transmission of LTE waveforms on IM-DD optical setup

5.1 Motivation

In this Chapter, next-generation radio waveforms such as LTE and 5G NR waveforms described in Chapter 3, are aggregated based on the DSP techniques using TDMA and FDMA approaches elaborated in Chapter 5 over a conventional PON infrastructure.

The main motive of this Chapter is to experimentally demonstrate the transport of up to 96 DSP−aggregated downlink LTE waveforms (PDSCH) on a single wavelength and 4 wavelengths on WDM experiment. The Chapter aims to evaluate the performance of the FDMA and TDMA based waveforms aggregation over the PON-like infrastructure, compliant with the Optical Distribution Network (ODN) parameters set by ITU-T in G.987.2 specification[55]. Specifically, one of the most critical issues in a PON is the very high loss introduced by the ODN. The minimum requirement in class N1 XG-PON is 29 dB of ODN loss. Moreover, this Chapter focus also on determining the correct requirements for the optical path in the fronthaul network while considering the radio link.

5.2 Optical path requirements

This section focus in determining the correct requirements for the optical path in a fronthaul based 5G networks while considering also the radio part. In optical fronthauling, the optical transmission should impair the signal as little as possible,

to give the biggest "budget" to the radio part. The relation between link quality and the modulation format to be adopted is analyzed in our work by the root mean square error vector magnitude EVM_{rms} specified in [2] and illustrated in Table 1.1. Those EVM values should be ensured at the final receiver end. Therefore, proper EVM-budgets should be determined for both optical and radio trunks, in order to defined the parameters for dimensioning the fronthaul segment. It is well known that (thanks to the Central Limit Theorem), on each individual OFDM subcarrier, an LTE and 5G NR transmission can be accurately modelled as an Additive White Gaussian Noise (AWGN). Thus, EVM can be related to SNR as described in Eq.4.24. The cascade of optical and the wireless radio link can be modelled by two Independent AWGN channels whose total SNR is :

$$SNR_{TOT} = \frac{1}{SNR_F^{-1} + SNR_W^{-1}}, \tag{5.1}$$

where SNR_F and SNR_W are the SNR of the fronthauling and the wireless parts respectively[17]. Translating Eq.5.1 to the total EVM, we can thus write:

$$EVM_{TOT} = \sqrt{EVM_F^2 + EVM_W^2}, \tag{5.2}$$

where EVM_F and EVM_W are the EVM on the fronthaul and wireless part. Assuming the maximum SNR penalty $K_{pen,dB}$, the wireless segment

$$SNR_{W,dB} = SNR_{TOT,dB} - K_{pen,dB}, \tag{5.3}$$

where $SNR_{TOT,dB}$ is the total target SNR at the mobile terminal specified in [2]. For instance, setting $K_{pen,dB} = 1$ dB would mean accepting a 1 dB penalty on the power budget of the wireless segment due to the degradation induced by the fronthaul segment. Rearranging 5.1 & 5.3, the $K_{pen,linear}$ can be expressed as

$$K_{pen,linear} = \frac{SNR_W - SNR_F}{SNR_F}. \tag{5.4}$$

Reintroducing the EVM expression

$$EVM_F = EVM_{TOT} \cdot \sqrt{\frac{K_{pen,linear} - 1}{K_{pen,linear}}}. \tag{5.5}$$

Eq.5.5 provides the EVM_F requirement on the fronthaul segment given the target total EVM_{TOT} and the acceptable penalty on the wireless link. Fig.5.1 shows the relation of EVM_F with $K_{pen,dB}$ for advanced modulation formats specified in [2] and the required EVM_{TOT} reported in Table 1.1. For instance, for a 64 QAM transmission with the requirement $EVM_{TOT} = 8\%$, acceptance of $K_{pen,dB}$= 3 dB penalty on the power budget of the wireless link would require $EVM_F < 6\%$ on the optical fronthaul segment. Taking into consideration an acceptable penalty on the radio link $K_{pen,dB} = 1$ dB, would need $EVM_F < 3.6\%$.Table 5.1 summarizes the max EVM_F penalty for different modulation formats.

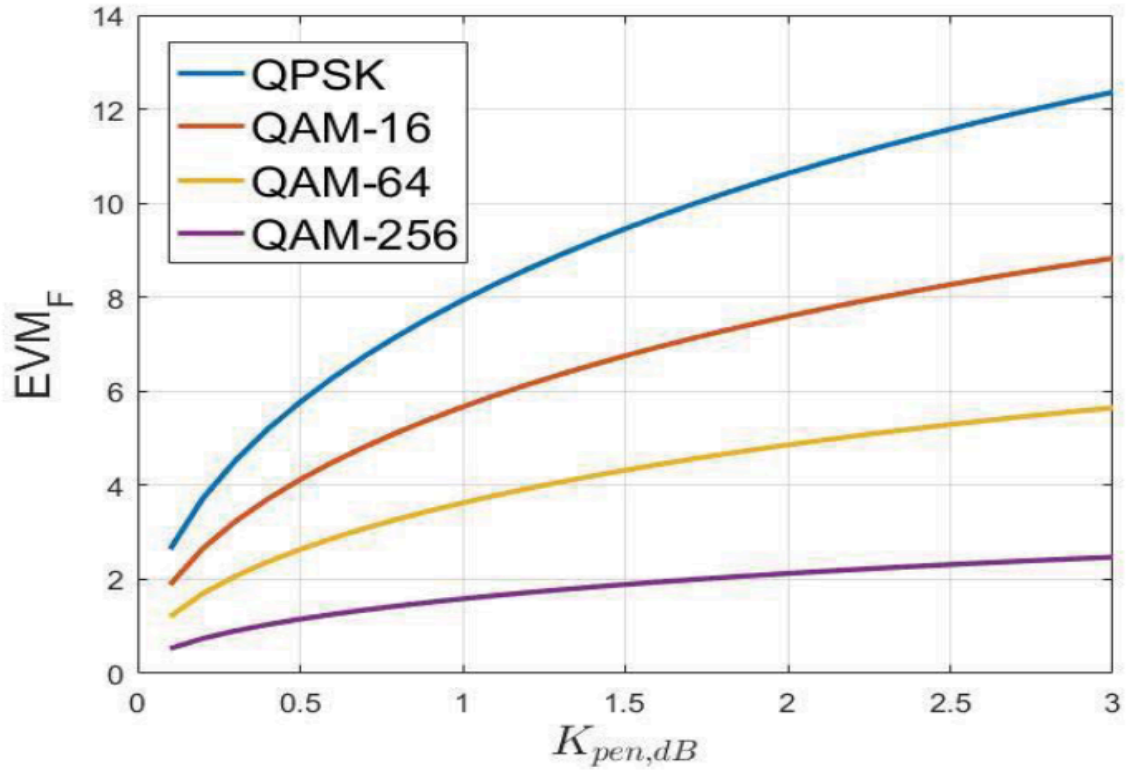

Figure 5.1: EVM (%) of the fronthaul segment vs. penalty on the wireless segment for different modulation formats.

Table 5.1: Modulation format vs. max EVM_F with 1 dB penality on the wireless link.

Modulation Formats	max EVM_F%
256-QAM	1.58
64-QAM	3.68
16-QAM	5.66
QPSK	7.93

5.3 Experimental setup

The experimental test bench that emulates the PON-like infrastructure based on IM-DD optical link is shown in Fig.5.2. At the transmitter side, an Arbitrary Waveform Generator (AWG) is used to store and process the off-line generated aggregated waveforms from the TX DSP. In the the fronthaul implementation considered in the Thesis, it is used as a digital-to-analogue converter (DAC) with a sampling rate equal to 12 Gsa/s and vertical resolution of 10 bits. The driver

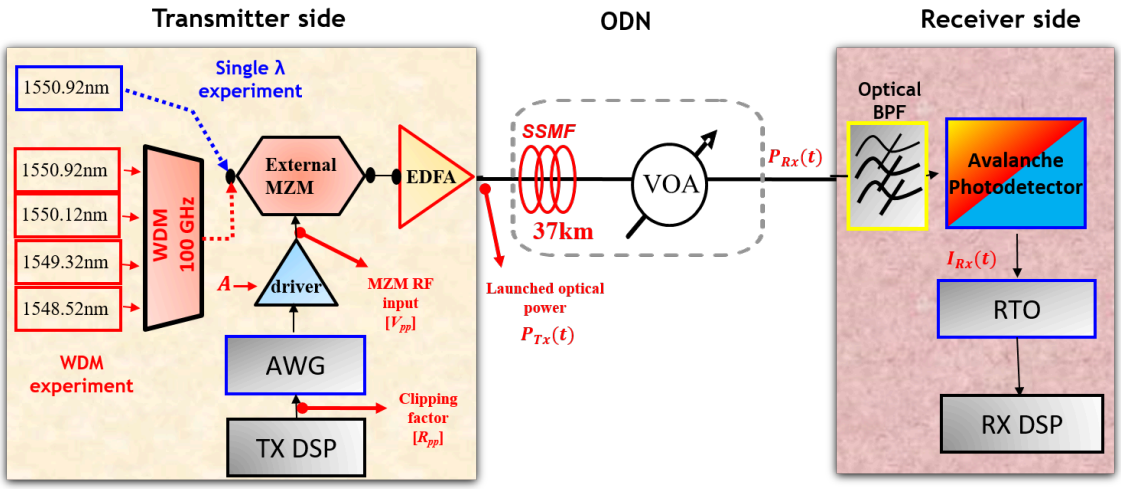

Figure 5.2: Experimental setup.

is used to amplify the AWG analogue output signal to the MZM radio frequency RF input. An external MZM modulator is used to modulate the continuous wave (CW) optical carrier. The External Cavity Laser (ECL) source generate laser at wavelength, $\lambda = 1550.92$ nm on a single wavelengthλ and four lasers at wavelength $\lambda_1 = 1550.92$, $\lambda_2 = 1550.12$, $\lambda_3 = 1549.32$ and $\lambda_4 = 1548.52$ nm multiplexed by arrayed waveguide grating on WDM (wavelength division multiplexing) experiment while dithering is set to on to remove the Brillouin effect. The DC bias voltage of the MZM should be optimized to obtain the maximum linearity of the transfer function of the MZM, biased at the quadrature point (3 dB point of the electro-optics transfer characteristics)[17]. The instantaneous optical signal from the MZM is amplified by Erbium Doped Fiber Amplifier (EDFA), to obtain an average launched optical power output ($P_F(t)$) of +9 dBm[18]. This power is in line with in the framework of today's NG-PON2 power level standardization. The EDFA in this experiment is used to counteract the loss incorporated by the external MZM. The optical signal output from the transmitter is launched into 37 km of standard single mode fiber (SSMF) and cascaded into VOA that is used to span several attenuation values for the emulation of high optical distribution network (ODN) loss in PON link.

At the receiver side, the optical bandpass filter with 10 GHz bandwidth is used to filter the out-of- band noise generated by EDFA at the transmitter. The filtered optical signal is directly detected using 10 $Gbps$ APD (an APD suitable for 10 $Gbps$ NRZ transmission) + TIA (Trans Impedance Amplifier), that is used to convert the received optical power into electrical current. The detected signal is stored in real time oscillator (RTO) characterized by a sampling rate of 40 Gsa/s, 10 GHz analogue bandwidth and a vertical resolution of 8 bits. The RTO is used as an analogue-to-digital converter and stores the digitized samples for off-line post

processing by the receiver DSP [74].

Expermental optimization of transmitter parameters

In Section 5.2, it is verified that the optical segment should give very low EVM_F. For example, the aforementioned EVM_F< 3.6% target on 64 QAM after the optical transmission corresponds to a BER «10^{-4} (almost error free). Such a low EVM requirement is thus a specific characterization of the system under consideration, which would then be highly optimized in order to obtain these very demanding EVM targets. The off-line generation of 24, 48 and 96 20 MHz LTE OFDM signals with 64-QAM subcarrier modulation and using parameters k-point and M-point FFT/IFFT which were introduced in previous Chapters as k = 16-point and M-point FFT/IFFT, where M = 1024, 2048 and 4096 respectively. The bandwidth occupancy of the FDMA signal is $B_{FDMA} = n \cdot F_s$ where n is the number of aggregated waveforms and F_s is sampling frequency (center frequencies) of a single LTE waveform . The bandwidth occupied by aggregation of n-20 MHz LTE waveforms including frequency gap $f_{DC} \approx 100MHz$ inserted to confront the low frequency (where most spurious back reflection are falling); side effects on the first channels, that can be introduced either from dithering of the laser frequency needed to shift the Brillouin threshold or from the control tones of MZM, with $F_s = 30.72MHz$ is therefore $24 \cdot 30.72\ MHz \approx 750MHz$, $48 \cdot 30.72\ MHz \approx 1500MHz$ and $96 \cdot 30.72\ MHz \approx 3000MHz$. The received signal spectrum (after the photodetection) for the three cases without applying pre-emphasis (pre-compensation) and transmitter parameters optimization are shown in Fig.5.3, 5.4 and 5.5 for 24, 48 and 96 channels respectively.

In the single λ wavelength experiment shown in Fig.5.2, a wide experimental campaign is performed to optimized the DAC clipping factor and the modulator (MZM) driving voltage so that the maximum possible performances can be achieved. These parameters are optimized at 29 dB of ODN loss (class N1 of XG-PON [55]), meaning that the parameters are optimized in order to get the best possible EVM at 29 dB regardless of what happens at lower losses. The average launched optical power (P_F) is set to +9 dBm. The contour plots of EVM_F as a function of DAC clipping factor and MZM driving voltage for the cases of 24, 48 and 96 FDMA aggregated $20MHz$ LTE radio waveforms is shown in Fig.5.6a, Fig.5.6b, and Fig.5.6c respectively.

From the contour plots, we can infer that the optimal MZM driving voltage should be very close to the V_π of the MZM in all the three cases, while the best DAC clipping is reduces from 13 to 9 dB when increasing the number of channels from 24 to 96. It is evident that, at 29 dB with transmitted power P_F = +9 dBm, an EVM_F (measured as an average over all the channels) close to the target 3.6 % is achieved with 24 radio waveforms, while for 48 radio waveforms we have $EVM_F < 6\%$ and $EVM_F < 8\%$ for 96 radio waveforms. Table 5.2 resumes the

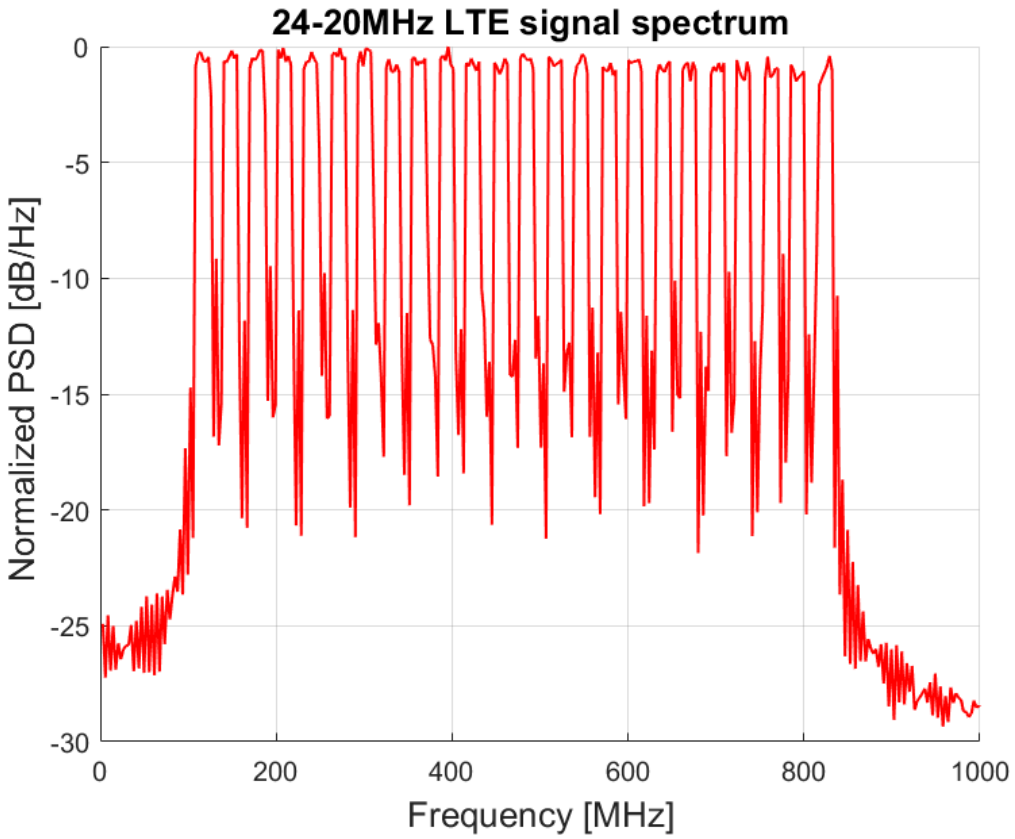

Figure 5.3: Electrical signal spectrum of FDMA DSP-aggregated 24-20MHz LTE waveforms after photodetection.

Table 5.2: Characteristics of n-DSP aggregation.

Number of channels	M-point FFT	Electrical spectrum	Optimum DAC clipping	Optimum MZM driving voltage
24	1024	0−750 MHz	13 dB	3.00 V_{pp}
48	2048	0−1500 MHz	12 dB	3.3 V_{pp}
96	4096	0−3000 MHz	9 dB	3.15V_{pp}

characteristics and the working conditions optimized for ODN loss of 29 dB.

Result discussion on FDMA DSP-aggregation

Fixing the optimum working points, the performance of 24, 48 and 96 20 MHz aggregated LTE waveform combs are evaluated on different ODN loss. Fig5.7 shows the EVM_F as a function of the ODN loss for the three cases, showing that the

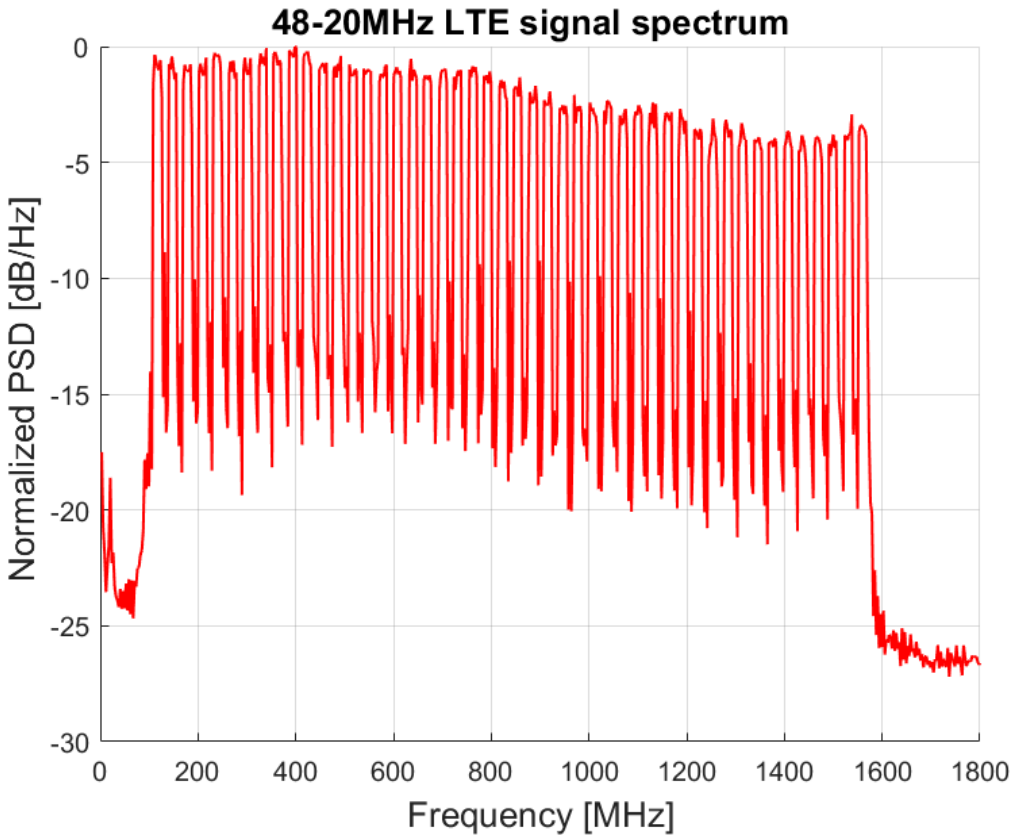

Figure 5.4: Electrical signal spectrum of FDMA DSP-aggregated 48-20MHz LTE waveforms after photodetection.

$EVM_F < 3.6\%$ requirement can not be reached for 96 channels and about 22 dB ODN loss appear to be affordable for 48 channels. If $EVM_F = 8\%$ is acceptable, these system can sustain up to 34 dB (class E1) for the case of 24 channel aggregation.

The power P_F launched into the ODN is increased up to 17 dBm (levels foreseen by video overlay over PON) to achieve the $EVM_F < 3.6\%$. Fig.5.8a reports EVM_F as a function of ODN loss and launch power evaluated on 48 20 MHz LTE waveforms. The resulting contour plot shows approximately a 1 dB in achievable ODN loss (for a given EVM_F target level) for each 1 dB increase in P_F, demonstrating that it is still below any significant nonlinear threshold. The only requirement was to apply a dithering tone on the transmitting laser to avoid Brillouin effect. Moreover, Fig.5.8 shows that at 29 dB ODN loss, the target $EVM_F < 3.6\%$ as required by $K_{Pen,dB} = 1$ dB can be reached for $P_F > 14$ dBm. If $EVM_F < 8\%$ is acceptable, the fronthaul system can sustain up to 35 dB ODN loss (class E2) for $P_F > 13$ dBm.

The EVM_F performance as a function of ODN loss and P_F is evaluated by

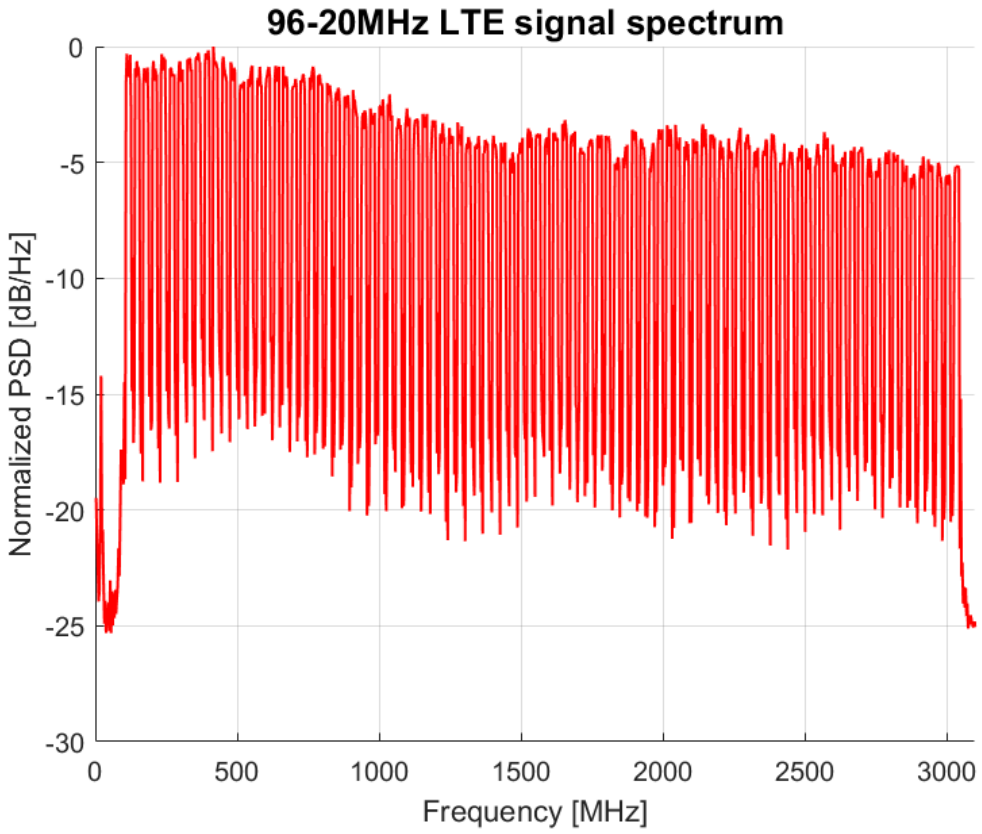

Figure 5.5: Electrical signal spectrum of FDMA DSP-aggregated 96-20MHz LTE waveforms after photodetection.

increasing the fronthaul capacity to 96 radio waveforms on a single wavelength λ. From the result shown in Fig.5.8b, the $EVM_F = 8\%$ target can be reached over 35 dB of ODN loss with the launched optical power increased to $P_F = 16$ dBm. Furthermore, the implementation on the WDM experiment, that is modulating over 4 wavelengths (100 GHz spacing) as in Fig.5.2 to emulate the transport of 4×96 radio waveforms. Fig.5.9 shows that there is no penalties encountered with WDM experiment.

Result discussion on TDMA DSP-aggregation

The received signal (after photodetection) spectrum of 48 and 96 TDMA aggregated LTE waveforms are shown on Fig. 5.10 and 5.11 respectively. The spectral bandwidth of TDMA signal is $B_{TDMA} = n \cdot w_{ch}$ where n is the number of TDMA aggregated channels and w_{ch} is the bandwidth occupied by a single waveform.; For example, the spectral bandwidth occupied by 48 and 96 TDMA aggregated 20 MHz LTE waveforms including DC subcarrier (intentionally inserted to prevent the

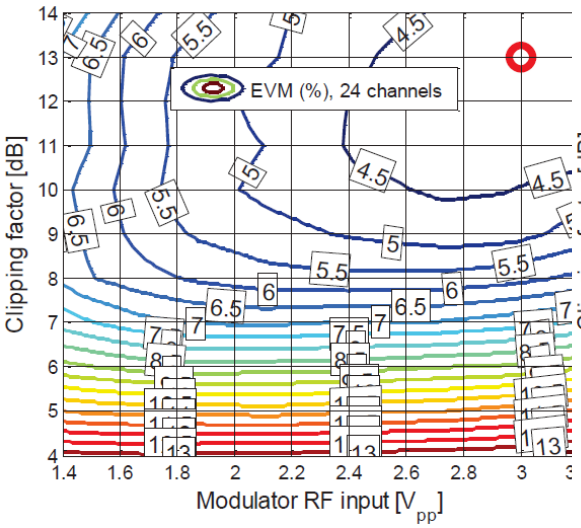

(a) 24-20 MHz LTE waveforms.

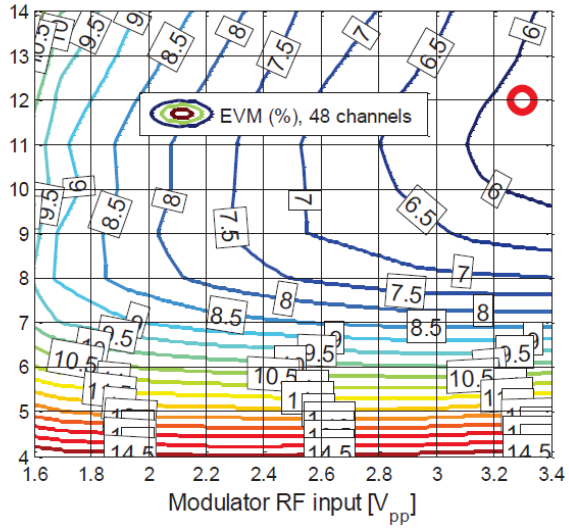

(b) 48-20 MHz LTE waveforms.

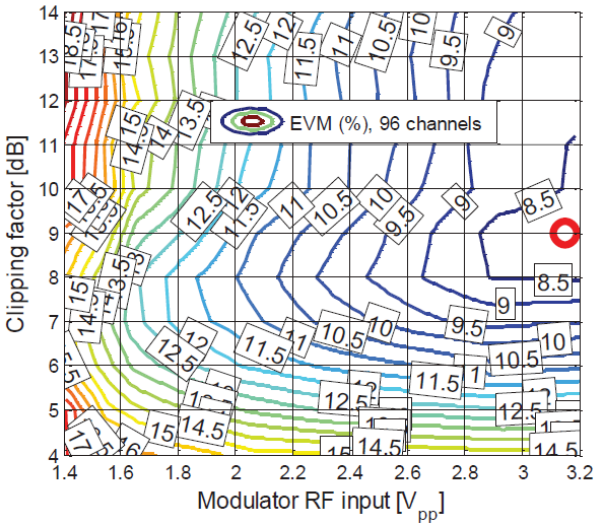

(c) 96-20 MHz LTE waveforms.

Figure 5.6: EVM_F vs. DAC clipping factor and MZM peak-to-peak driving voltage at 29 ODN losses.

effect back reflection on the first channels) is approximately 1000 and 2000 MHz respectively.

Targeting $EVM_F = 8\%$ on 64-QAM modulated LTE waveform, the DAC clipping factor optimization while considering V_π of the MZM driving voltage, for 48 and 96 LTE waveforms is performed at 31 and 29 dB ODN loss respectively. As shown in Fig.5.12 , the optimum clipping factor for 48 and 96 channels are obtained

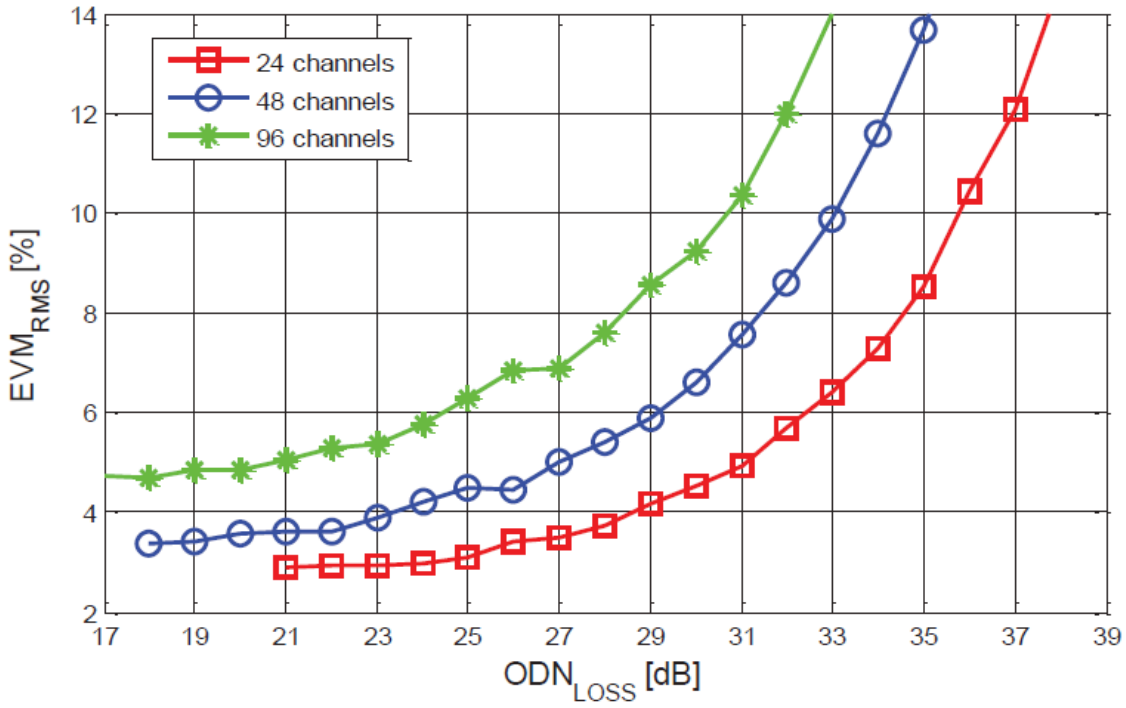

Figure 5.7: EVM_F vs. ODN loss using optimized Tx parameters.

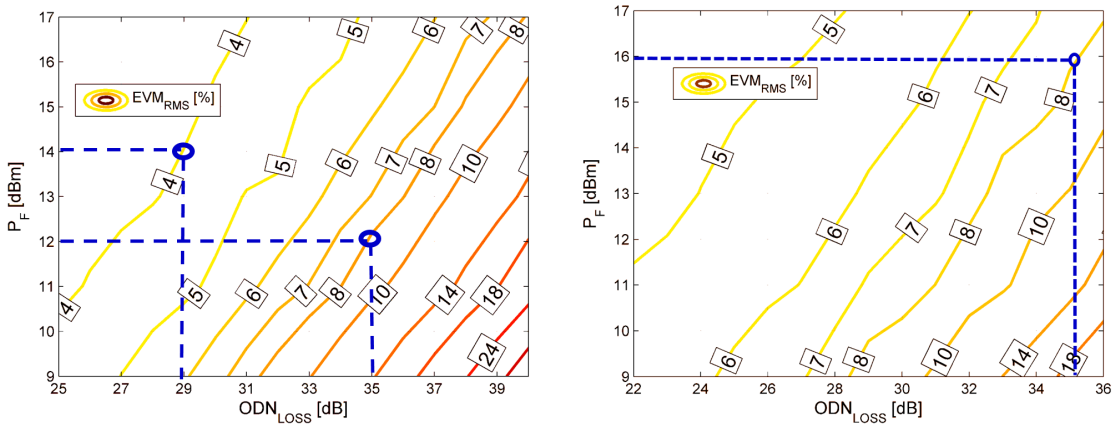

(a) 48-20 MHz LTE waveforms.

(b) 96-20 MHz LTE waveforms.

Figure 5.8: EVM_F vs. ODN loss and launched power P_F.

at 14 dB and 13 dB respectively. The performance of the 48 and 96 TDMA aggregated LTE waveforms on different ODN losses are evaluated by using the optimized working conditions. From the results shown in Fig.5.13, the target $EVM_F = 8\%$

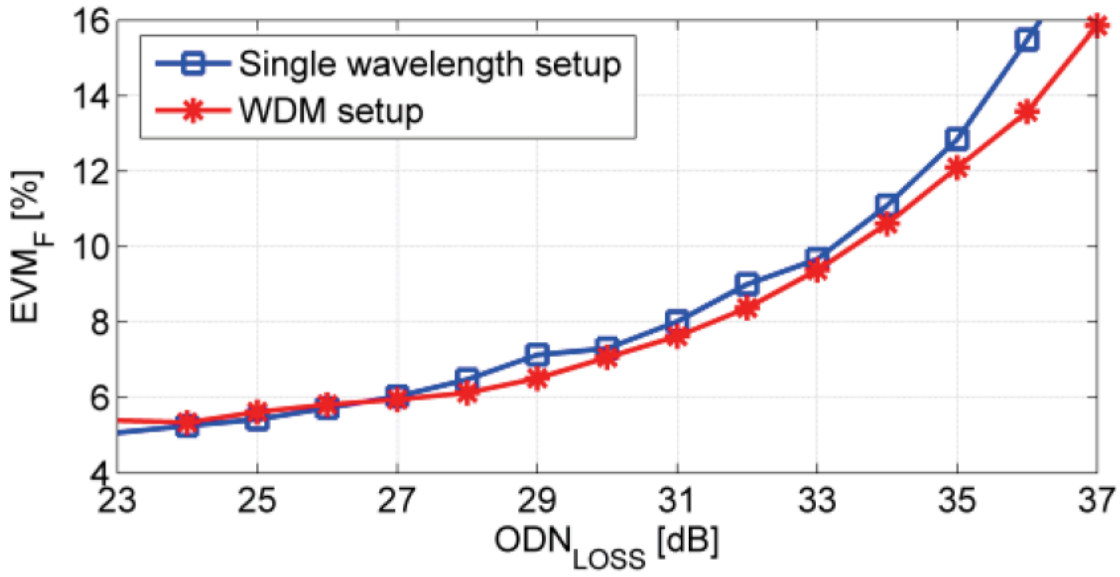

Figure 5.9: EVM_F vs. ODN loss for 96 radio waveforms at $P_F = 11$ dBm per wavelength with single wavelength or 4 wavelengths WDM setup.

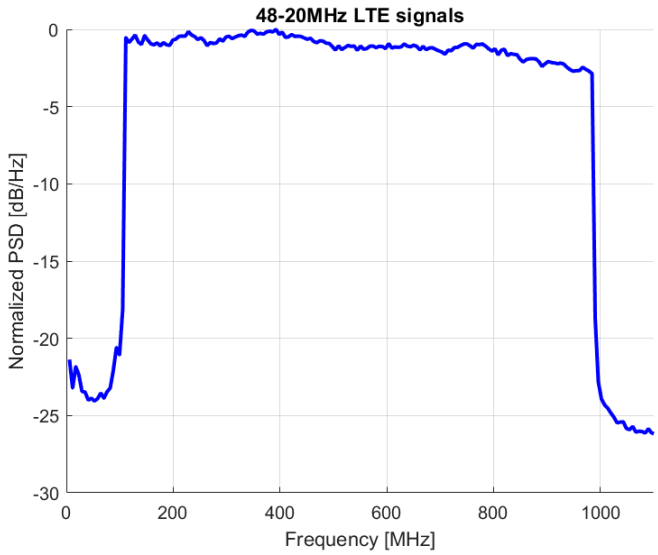

Figure 5.10: Electrical signal spectrum of 48-20MHz LTE TDMA DSP-aggregated waveforms after photodetection.

for 48 and 96 channels is reached at ODN loss of 33 dB and 30 dB respectively.

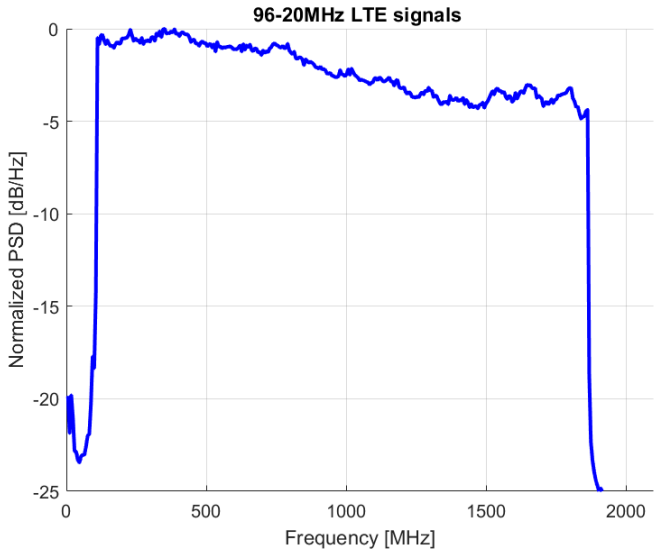

Figure 5.11: Electrical signal spectrum of 96-20MHz LTE TDMA DSP-aggregated waveforms after photodetection.

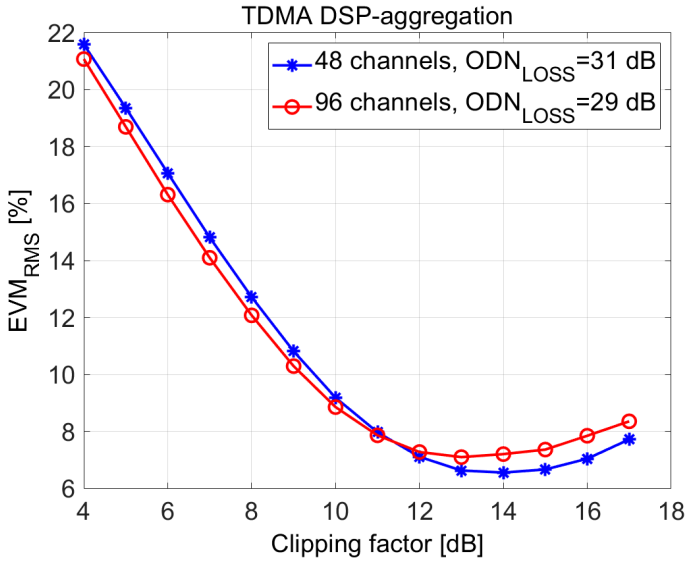

Figure 5.12: Clipping factor optimization for 48 and 96 waveforms at 31 and 29 dB ODN loss respectively.

Comparison of TDMA and FDMA DSP aggregation of LTE waveforms

The probability density function(pdf) of the aggregated outputs of 96(taken as an example) TDMA and FDMA waveforms is shown in Fig.5.14. The Gaussian pdf with the same variance is superimposed on the two pdf. The three curves

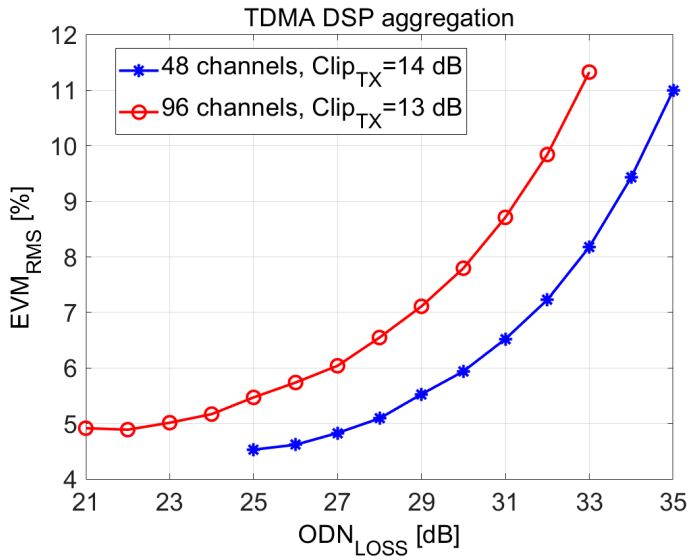

Figure 5.13: EVM_F vs. ODN loss using optimized clipping for 48 and 96 channels.

are almost identical, showing that both FDMA and TDMA aggregated signal are well approximated by a Gaussian distribution (validates the assumptions made so far), a result that arises from the central limit theorem (which are n statistically independent OFDM signal, each of which is Gaussian-like).

However, the spectral bandwidth occupation of FDMA is greater than the TDMA for the same number of channel aggregation. This is due to the fact that the overall signal aggregated in FDMA is based on the sampling frequency of a single LTE waveform whereas the signal aggregated in TDMA is based on the bandwidth of a single LTE waveform. For example, the bandwidth occupied by aggregation of 96 20 MHz LTE waveforms in FDMA shown in Fig.5.5 and in TDMA shown in Fig. 5.11 is $B_{FDMA} = 96 \cdot 30.72MHz \approx 3000$ MHz and $B_FTDMA = 96 \cdot 20MHz \approx 2000$ MHz respectively. This shows that there is ≈ 1 GHz spectral gain by using TDMA for the same number of 96 channel aggregation.

The EVM_F performance on each of the 96 LTE waveforms aggregated by TDMA and FDMA approach, at 29 dB ODN loss and the corresponding optimum clipping factor is shown in Fig.5.15. From the black curve (FDMA without pre-emph), it can be verified that the system frequency response that arises due the bandwidth roll-off behavior of the MZM, APD, AWG, RTO and optical fiber, severely degraded the performance of the FDMA aggregated waveforms towards higher frequency. Therefore, pre-emphasis technique described in Section 4.3 at the transmitter side is required to equalized (distribute) the EVM performance along the entire frequency. The pre-emphasis method is based on the multiplication of each waveform at the transmitter side (before channel aggregation) by an

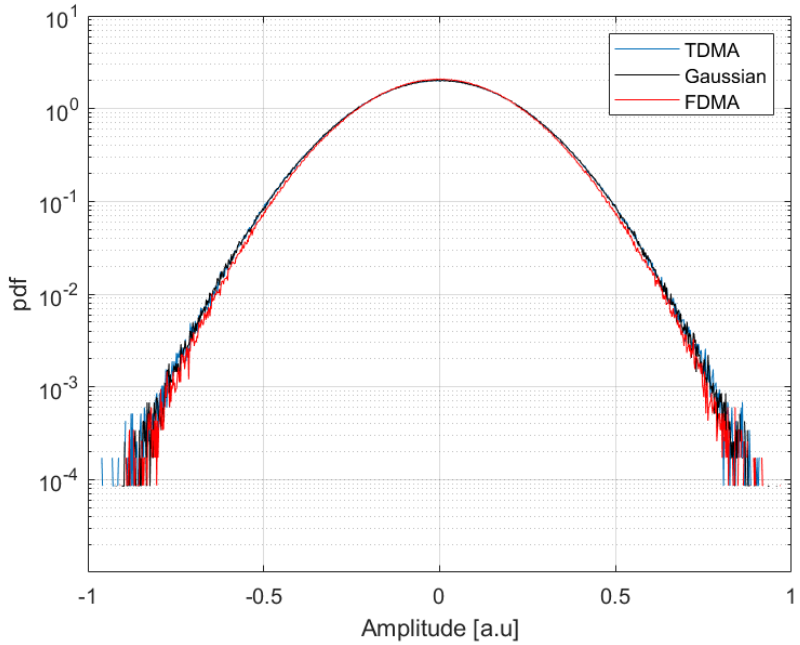

Figure 5.14: PDF of aggregated output of the TDMA and FDMA signal superimposed with Gaussian distribution.

amplitude scaling factor such that channels with higher frequency gain are multiplied by a scaling factor $k < 1$ (de-emphasis) and channels with lower frequency gain are multiplied by a scaling factor $k > 1$. This procedure is repeated iteratively off-line until no more EVM or power change occur along the channels as shown by the red curve (FDMA with pre-emph) in Fig.5.15. In contrast to FDMA, in TDMA aggregation the frequency response of the system affects the entire aggregated waveforms (channels) uniformly as shown by the blue curve (TDMA without pre-emph), hence pre-emphasis is not required in TDMA which is due to the fact that the waveforms aggregated in time is not altered by the system frequency response. The decoded signal constellation of the 96^{th} LTE for the three cases is shown in Fig.5.16. Fig.5.16a depicts the received constellation with FDMA without pre-emphasis at $EVM_F = 12\%$, Fig.5.16b shows the FDMA channel equalized with pre-emphasis (pre-compensated) at $EVM_F = 8\%$ and Fig.5.16c show the TDMA received constellation at $EVM_F = 7\%$.

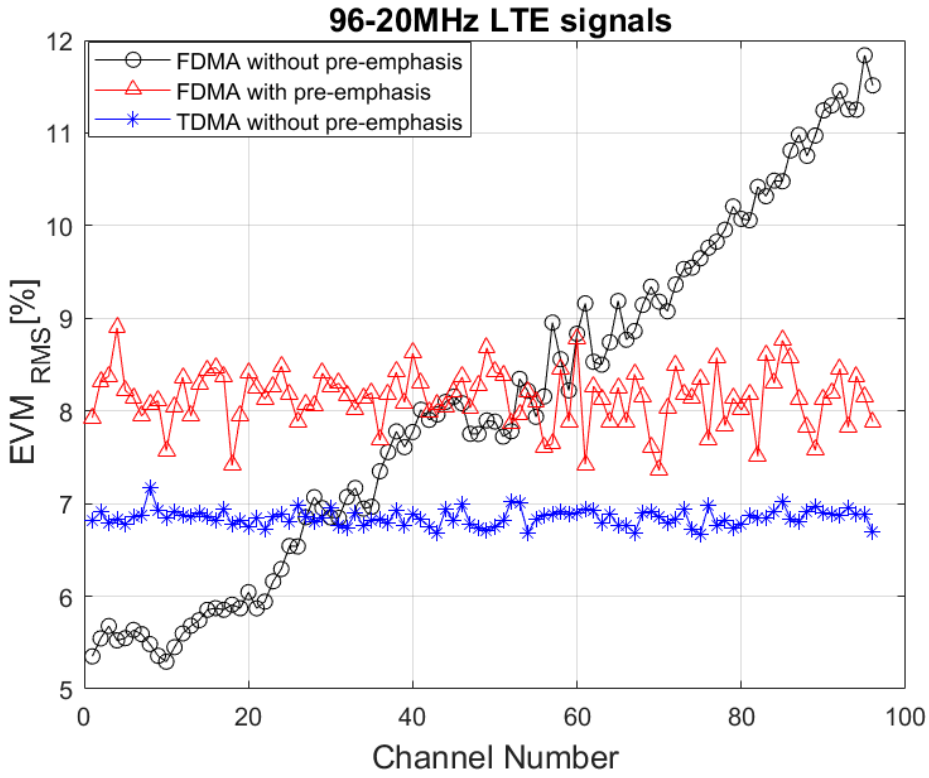

Figure 5.15: Per channel EVM_F TDMA/FDMA aggregated 96 LTE waveforms obtained at 29 dB ODN loss and optimum clipping factor.

5.4 Chapter summary

This Chapter discuses about the experimental demonstration of the fronthaul solution transporting up to 4×96 LTE waveforms assisted by DSP aggregation/de-aggregation using FDMA and TDMA approach at the transceiver side. The first section outlines on dimensioning the correct EVM requirements for the optical path (fronthaul) with the consideration of the radio link (wireless part). Based on the analysis of the fronthaul dimensioning which requires very high fronthaul performance, the optimization of optical parameters at the transmitter side is performed on a wide set of experimental campaign. The frontahul performance with the optimized transmitter parameters is evaluated by transporting up to 96 LTE waveforms on a single wavelength λ and 4×96 LTE waveforms over 4 wavelength on WDM using FDMA approach. The set of experiment using TDMA DSP aggregation is demonstrated on the same experimental set up used for FDMA. Finally, the results obtained by both FDMA and TDMA approaches are compared to verify which of the two give better performance , less DSP complex and better spectral efficiency. It reveals that TDMA approach on aggregation of 96 LTE channels give slightly

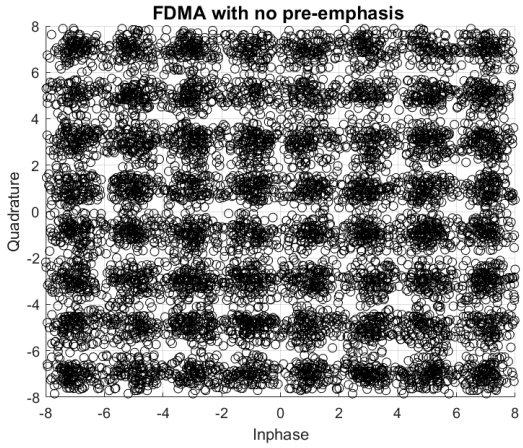

(a) FDMA without pre-emphasis

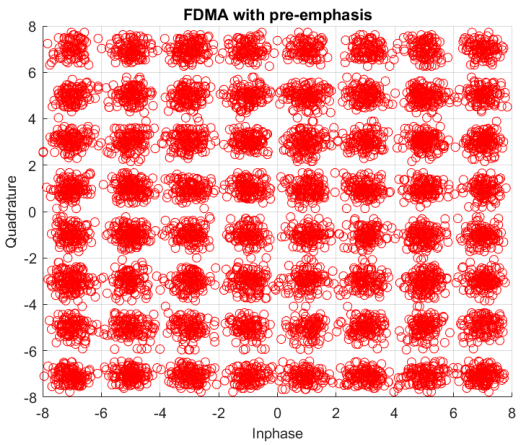

(b) FDMA with pre-emphasis.

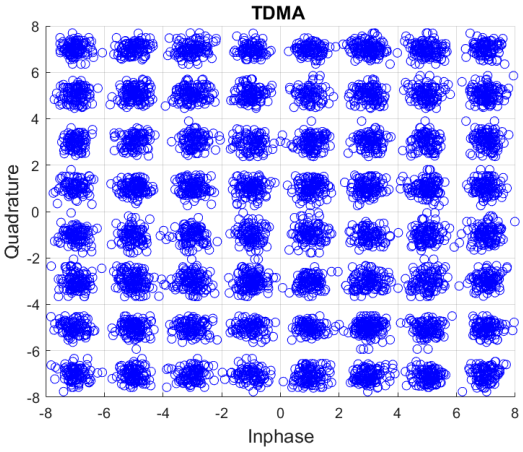

(c) TDMA without pre-emphasis.

Figure 5.16: Decoded signal constellation of the 96^{th} LTE waveform modulated with 64-QAM.

better performance, less DSP complexity since no pre-emphasis is used and compact spectral bandwidth with respect to FDMA.

Chapter 6

Analysis of 5G NR uplink on A-RoF fronthaul based on DSP-assisted channel aggregation

6.1 Motivation

New technologies such as automated intelligence, the Internet of Things, and high speed data communications, among others requires faster, high capacity, and reliable devices. To fulfill such demand, the 5^{th} generation (5G) mobile communication system is underway to provide unparalleled connected mobile devices by the year 2020. This new mobile paradigm will thus require significant technology advancement in both wireless and optical access networks. The key goal of this chapter is to analyze the transmission of 5G NR uplink physical channels (using multiple numerologies), such as Physical Uplink Shared Channel (PUSCH) and Physical Uplink Control Channel (PUCCH), dedicated for the data and control channels respectively, using DSP-assisted FDMA and TDMA channel aggregation techniques realized on simulated A-RoF system architecture. Furthermore, this Chapter aims to compare the link performance in terms of EVM_F, spectral efficiency and DSP complexity between the two aggregation schemes.

6.2 Simulation setup

The simulation setup that is used to emulate the realistic A-RoF fronthaul architecture based on IM-DD optical model is shown in Fig.6.1. The model assumptions which are inherited from experimental setup described in Section 5.3 and the methods used in the realization of the simulation model [73] are described below.

At transmitter side, the DAC is simulated by a vertical resolution of 10 bits. A

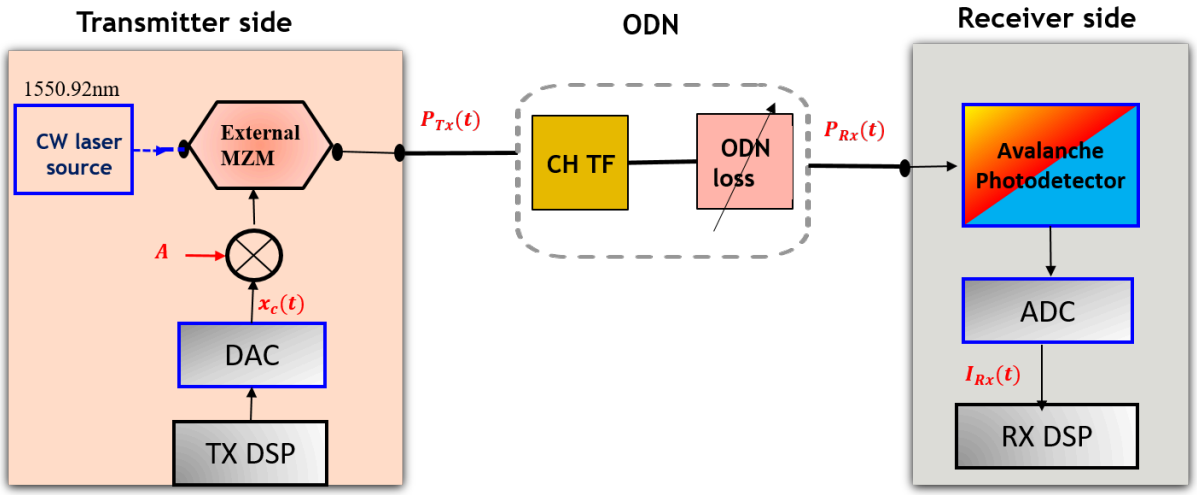

Figure 6.1: Simulation setup.

classical nonlinear external MZM model is implemented by assuming the following parameters : static extinction ratio (ER) = 27.8 dB, insertion loss (IL) = 1.8 dB, V_π RF electrode voltage = 3.0 V, DC bias voltage $(A) = \frac{V_\pi}{2}$ where V_π is the half wave switching voltage and the modulation index, a parameter used to quantify the degree of MZM is defined as $M = \frac{A}{V_\pi} \cdot \pi$. The optimum MZM performance which gives low EVM is obtained experimentally when it is biased at its quadrature point (modulation index $M = 100\%$) is taken from the previous Chapter experiment result. The CW laser source is assumed to be ideal and operating at wavelength 1550.92 nm. The optical channel is emulated by considering the transmitter side optical signal output is propagated into standard single mode fiber (SSMF) characterized by chromatic dispersion (CD) coefficient = 17 $\frac{ps}{nm \cdot km}$ and span length L = 25 km. Moreover, the optoelectronics bandwidth limitation is simulated by using the 4^{th} order Bessel filter having a 3-dB bandwidth of 3.5 GHz, which was the best-effort fitting of the end-to-end electrical to electrical transfer function measured on the experimental test bench. This bandwidth together with the receiver noise are the main limitation of the considered system.

At the receiver side, the APD is modelled by assuming that its noise contribution arises from the Gaussian amplified shot noise, electrical thermal noise in the electrical circuitry and dark current noise, which are independent and identically distributed [43]. The amplified shot noise is usually considered as the most relevant, and it is assumed to be flat on the entire system bandwidth, so that its variance on a channel bandwidth w_{ch} can be estimated in $[A^2]$ as

$$\delta_{sh}^2 = 2qMF_{APD}\rho P_{Rx} w_{ch}, \tag{6.1}$$

where q is the charge of an electron, M is the maximum APD gain, F_{APD} excess

Table 6.1: Summarized 5G NR parameters based on subcarrier spacings (SCs) type.

SCs Type	SCs Type [kHz]	Maximum bandwidth [MHz]	Sampling rate [Msa/s]
0	15	50	61.44
1	30	100	122.88
2	60	200	245.56
3	120	400	491.52

noise factor, ρ is the responsibility at wavelength 1550.92 nm and P_{Rx} is the received optical power. The electrical thermal noise variance can be described as

$$\delta_{\tau}^2 = S_{th}^2 \cdot w_{ch}, \tag{6.2}$$

where S_{th} is input-referred thermal current in $[A^2]$. Parameters used to model the APD are taken from the APD used in experiment set up described on the previous Chapter (LabBuddy model from Discovery semiconductors) specified as : $S_{th} = 11\frac{pA}{\sqrt{Hz}}$, $F_{APD} = 5.5$, $M = 7$ and $\rho = 0.875[\frac{A}{W}]$. ADC is realized by 8 quantization bits. The transmitter (TX) and receiver (RX) side DSP functionalities of FDMA and TDMA are described in Chapter 4 in Fig.4.14 and Fig.4.1 respectively.

6.3 Results and discussion

The performance of the 5G NR uplink channels (PUSCH and PUCCH) with the maximum bandwidth, are analyzed based on the numerologies resumed from Table 3.4 and summarized as in Table 6.1. A single NR uplink channel in the simulation analysis is realized by PUCCH with format # 0 using quadrature phase shift keying (QPSK) modulation and having a length of two consecutive OFDM symbols per slot for the uplink control information (UCI), and PUSCH data part is modulated using 64−QAM.

SC Type 0

The aggregation of SC type 0 72−50 MHz NR channels in FDMA is realized by setting K-point= 16 FFT/IFFT size on the DSP setup shown in Fig.4.14. The electrical spectrum of 72−50 MHz NR channels at the RX DSP input obtained by FDMA and TDMA is shown in Fig.6.2. The red and the blue line curve is used for indication of the FDMA and TDMA aggregation respectively. The total bandwidth occupied by FDMA is $BW_{FDMA} = n \times 61.44MHz \approx 4700MHz$ (including 300 MHz guard from DC), where 61.44 is the sampling rate of each

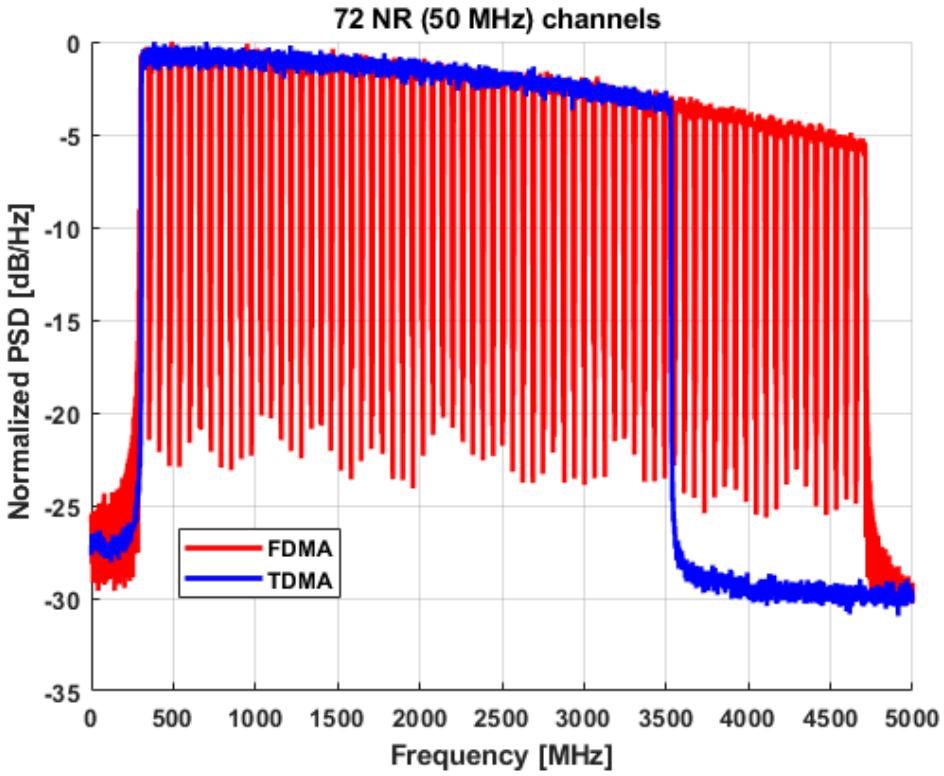

Figure 6.2: Electrical signal spectrum of 72 50-MHz NR SC Type 0 channels.

NR channel. Conversely, the total bandwidth occupied by TDMA aggregation is $BW_{TDMA} = n \times 50MHz \approx 3500MHz$, where 50 MHz is the bandwidth of each NR channel. For the same number of channel aggregation, TDMA aggregation saves $\approx$ 1 GHz bandwidth as compared to the FDMA. The spectral roll of towards higher frequency channel is due to the system frequency response. In the case of FDMA, the performance degradation of higher channel is pre-compensated by Pre-emphasis technique described in Chapter 4.

The transmitter parameter optimization while fixing the V_π of the MZM is evaluated on the DAC clipping ratio. The EVM_F (computed as a mean valued for all the channels) vs. clipping ratio performed on PUCCH and PUSCH at 29 dB ODN loss is shown in Fig.6.3a and 6.3b respectively. The optimum clipping ratio for both signal types and DSP-aggregation technique is obtained at 12 dB.

The EVM_F (mean) as a function of the ODN loss, evaluated at the optimum clipping (12 dB) for PUCCH and PUSCH is reported in Fig.6.4a and 6.4b respectively. The EVM_F performance of TDMA is slightly better for both signal types (PUCCH and PUSCH). This is associated with TDMA's spectral compactness when compared with FDMA, which is less affected by the optical channel response towards the higher channels.

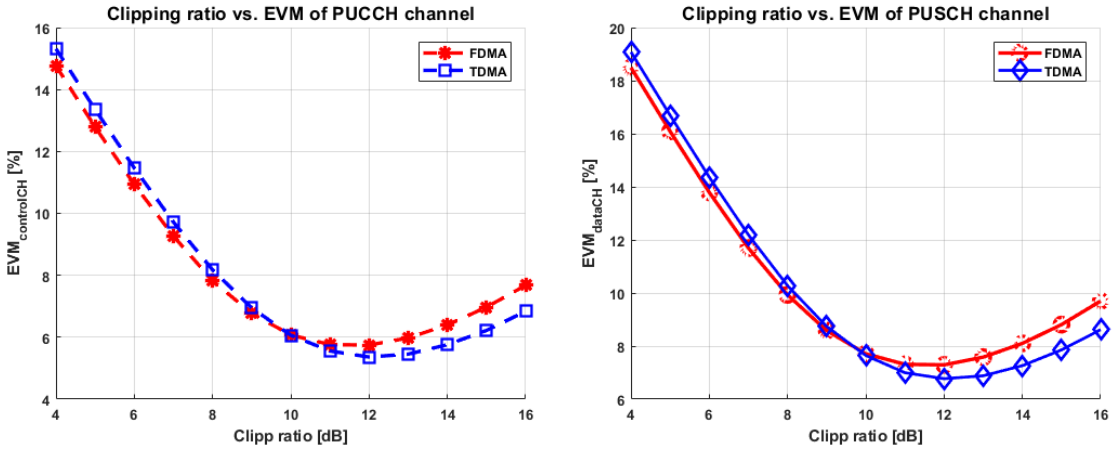

(a) PUCCH. (b) PUSCH.

Figure 6.3: Clipping optimization for 72-50 MHz NR channels at 29 dB ODN loss.

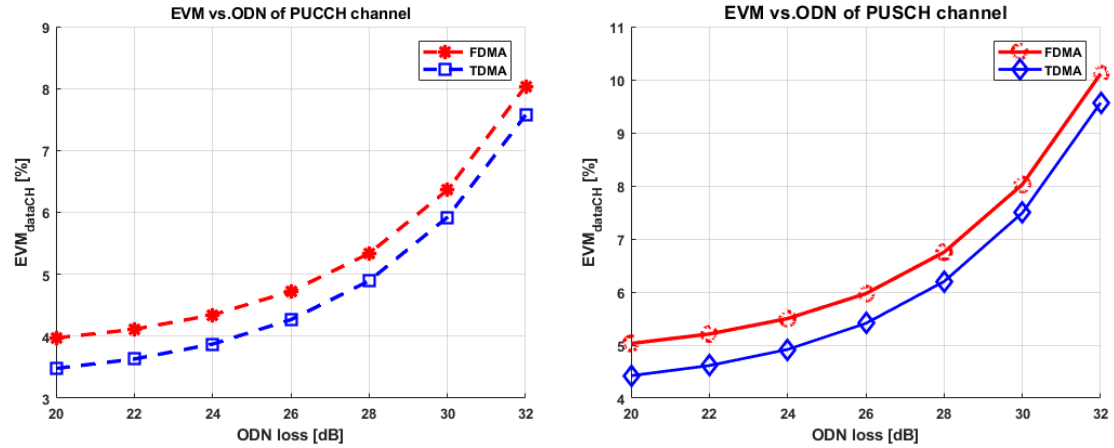

(a) PUCCH. (b) PUSCH.

Figure 6.4: Mean EVM_F vs. ODN loss for 72-50MHz NR channels at 12 dB clipping ratio.

SC Type 1,2 and 3

The same procedure reported in Section 6.3 was repeated for different SC Types, the analysis is repeated while changing the number of channels for the desired SC Type such that the Nyquist criterion is full filled on a DAC sampling rate of 12 Gsa/s. The parameters and obtained results are summarized in Table 6.2.

The electrical signal spectrum of SC Type 1 for number of channel $n = 36$, for SC Type 2 for $n = 18$ and SC Type 3 for $n = 9$ aggregated NR channels at the RX

Table 6.2: Summary of parameters and results for different types of SCs,BW bandwidth; Fs sampling rate.

Parameters	Type 0	Type 1	Type 2	Type 3
n	72	36	18	9
BW per NR channel [MHz]	50	100	200	400
Fs per NR channel [Msa/s]	61.44	122.88	245.76	491.52
Total BW TDMA [GHz]	3.6	3.6	3.6	3.6
Total BW FDMA [GHz]	4.6	4.6	4.6	4.6
FDMA - TDMA BW [GHz]	≈ 1.1	≈ 1.1	≈ 1.1	≈ 1.1
Optimum clipping ratio	12 dB	12 dB	12 dB	12 dB

DSP input is shown in Fig.6.5, 6.6 and 6.7 respectively. The red line curve is for the FDMA and the blue line is used for TDMA. The total bandwidth occupied by FDMA is $BW_{FDMA} = n \times Fs \approx 4700MHz$ (including 300 MHz from DC) for all SC Types, where Fs is the sampling frequency per NR channel. Instead, the total bandwidth occupied by TDMA is $BW_{TDMA} = n \times BW \approx 3600MHz$ for all SC Types, where BW is the bandwidth of each NR channel. Hence, TDMA saves $\approx$ 1.1 GHz bandwidth compared with FDMA for the same number n of channel and SC Type, as described in Table 6.2.

The clipping ratio optimization for SC Type 1 for number of channel $n = 36$, for SC Type 2 for $n = 18$ and SC Type 3 for $n = 9$ NR channels on both signal types (PUCCH and PUSCH) at 29 dB ODN loss is shown in Fig. 6.8, 6.9 and 6.10 respectively. The optimum clipping ratio for both signal types, DSP aggregation techniques and for all SCs Types are obtained at 12 dB as described in Table 6.2.

The EVM_F (mean) as a function of the ODN loss for SC Type 1 for number of channel $n = 36$, for SC Type 2 for $n = 18$ and SC Type 3 for $n = 9$ NR channels evaluated at the optimum clipping ratio of 12 dB for PUCCH and PUSCH is reported in Fig. 6.11, 6.12 and 6.13 respectively. The mean EVM_F performance is slightly better at higher ODN loss for both signal types (PUUCH and PUSCH). The spectral compactness associated with TDMA as compared to FDMA gives an advantage to be less affected by the optical channel response towards the higher channels.

The decoded symbol constellation after channel equalization on the ninth 400 MHz (SC Type 3) NR channel is shown in Fig.6.14. Fig.6.14a and 6.14b shows the PUCCH and PUSCH symbol constellation at $EVM_F = 6$ % and $EVM_F = 7.5$ % respectively using FDMA. Fig.6.14c and 6.14d shows that the PUCCH and PUSCH symbol constellation at $EVM_F = 5.5$ % and $EVM_F = 6.5$ % respectively using TDMA at 29 dB ODN loss.

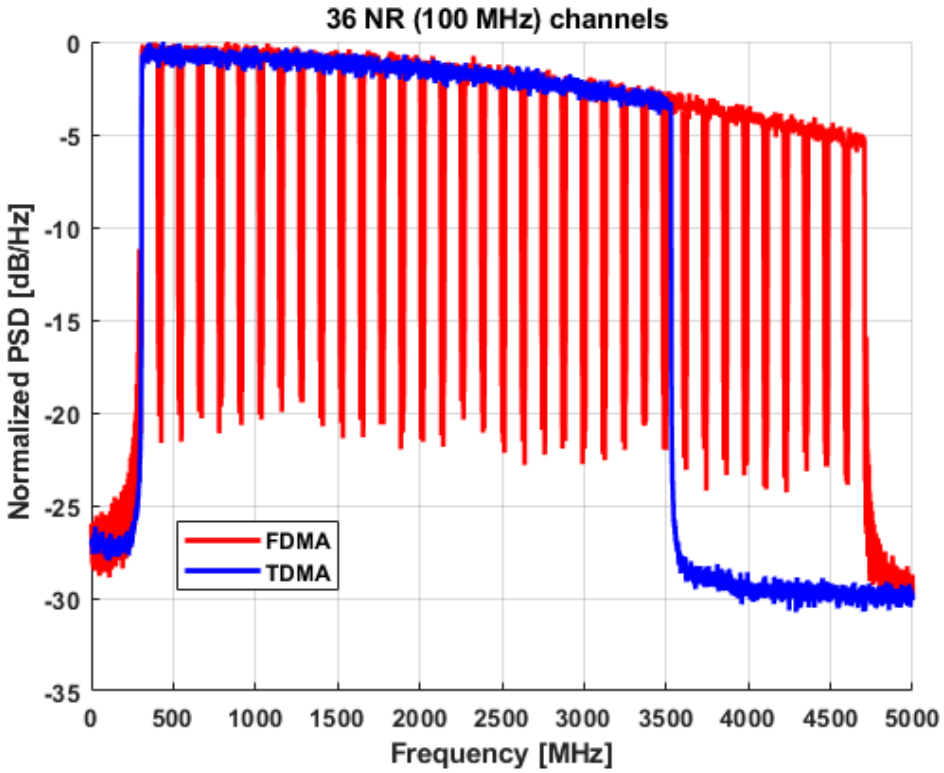

Figure 6.5: Electrical signal spectrum of 36-100MHz NR SC Type 1 channels.

6.4 Chapter summary

This chapter explains about the procedure followed on the emulation of the A-RoF fronthaul architecture based on IM-DD optical model. Moreover, the performance analysis of the for the aggregation of uplink 5G NR channels on different scalable subcarrier spacing (SCs) Types are studied on the IM-DD optical mode based on TDMA and FDMA based DSP-aggregation. It is verified that the TDMA approach saves ≈ 1 GHz bandwidth occupation when compared with FDMA, which also leads to a slight EVM_F performance improvement.

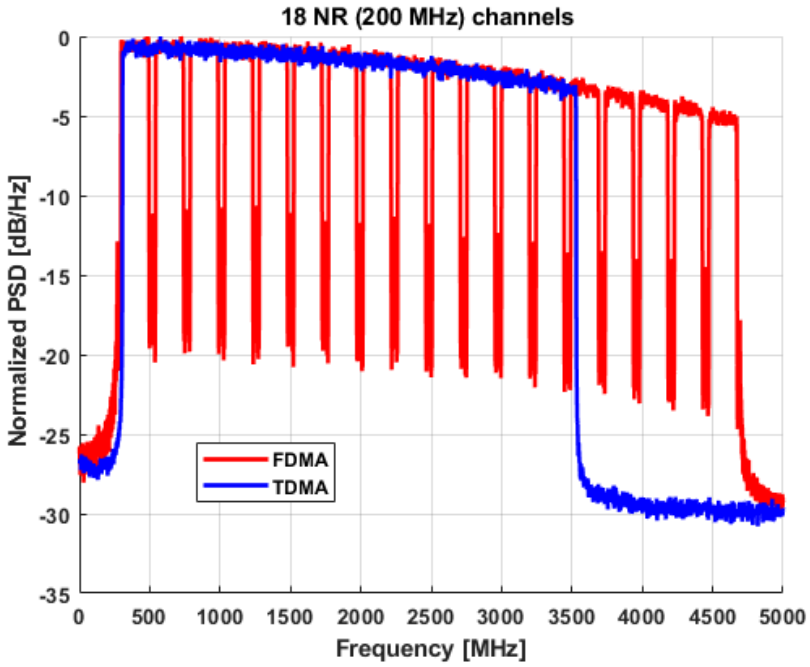

Figure 6.6: Electrical signal spectrum of 18-200MHz NR SC Type 2 channels.

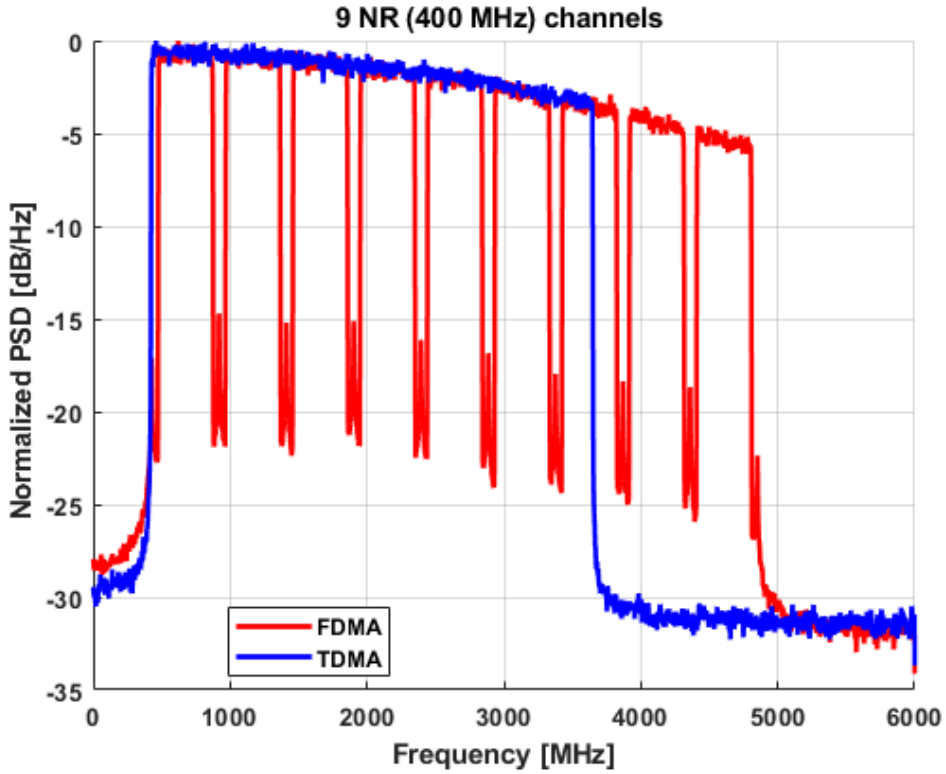

Figure 6.7: Electrical signal spectrum of 9-400MHz NR SC Type 3 channels.

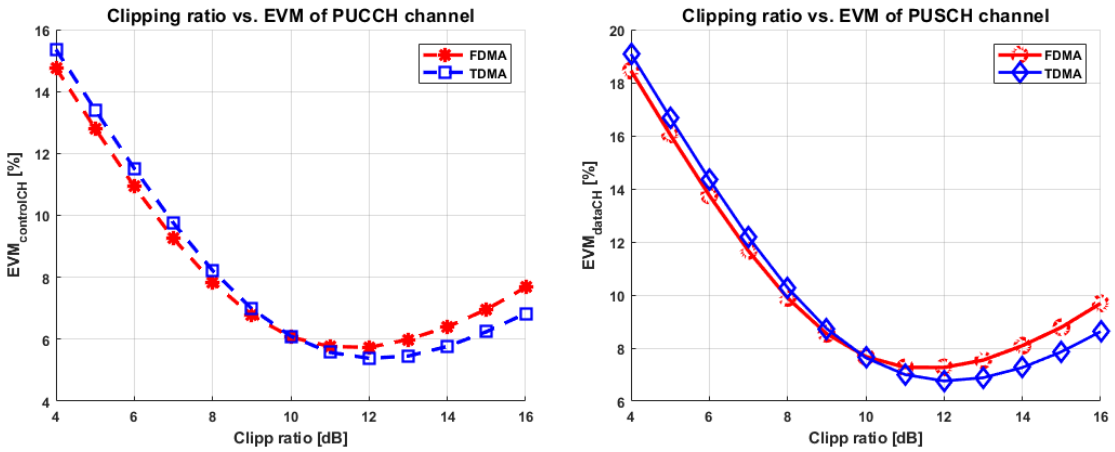

(a) PUCCH (b) PUSCH

Figure 6.8: Clipping optimization for 36-100 MHz NR channels at 29 dB ODN loss.

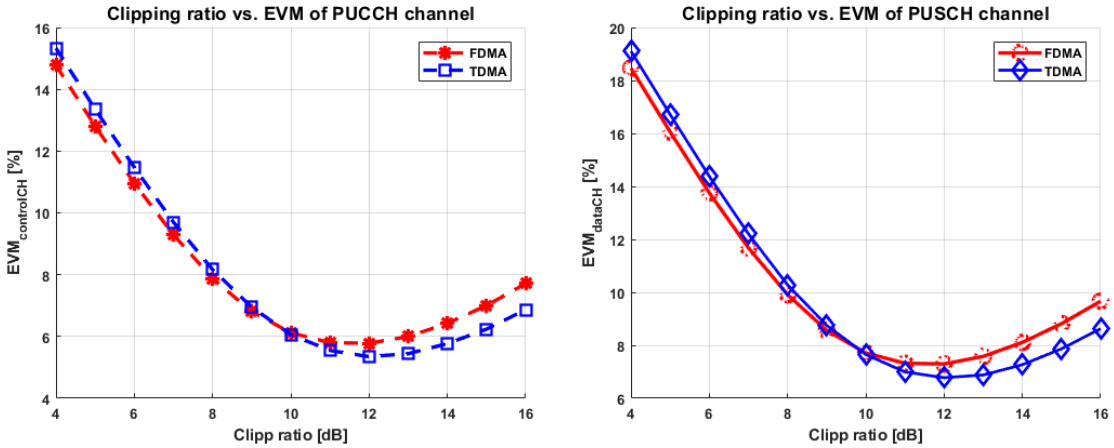

(a) PUCCH (b) PUSCH

Figure 6.9: Clipping optimization for 18-200 MHz NR channels at 29 dB ODN loss.

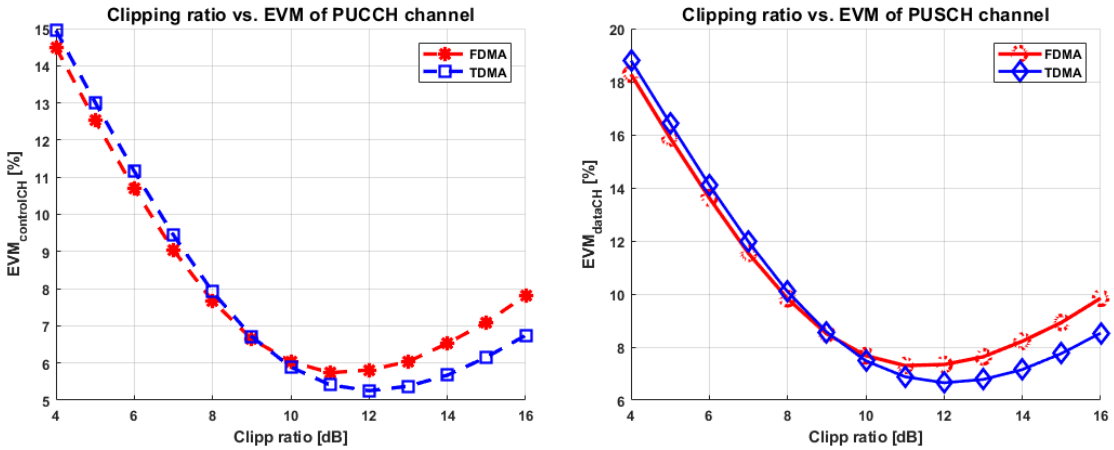

(a) PUCCH. (b) PUSCH.

Figure 6.10: Clipping optimization for 9-400 MHz NR channels at 29 dB ODN loss.

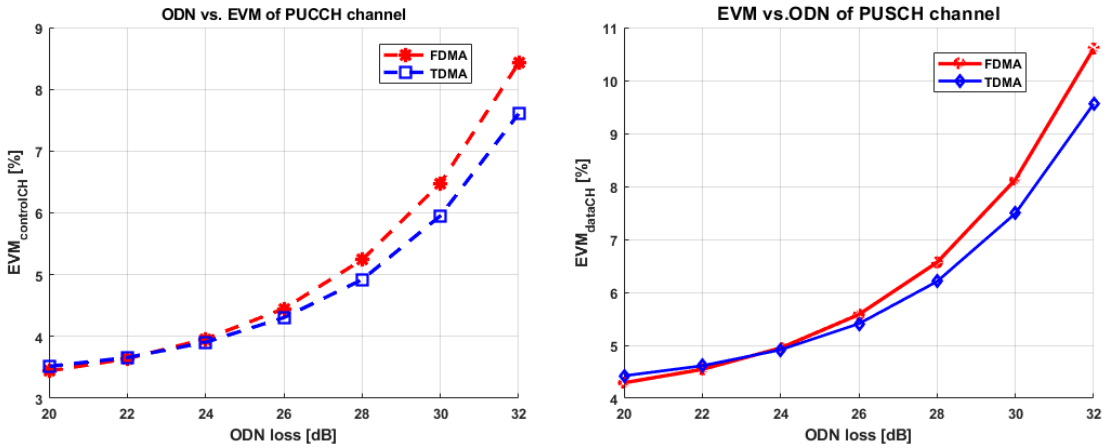

(a) PUCCH. (b) PUSCH.

Figure 6.11: Mean EVM_F vs. ODN loss for 36 100-MHz NR channels at 12 dB clipping ratio.

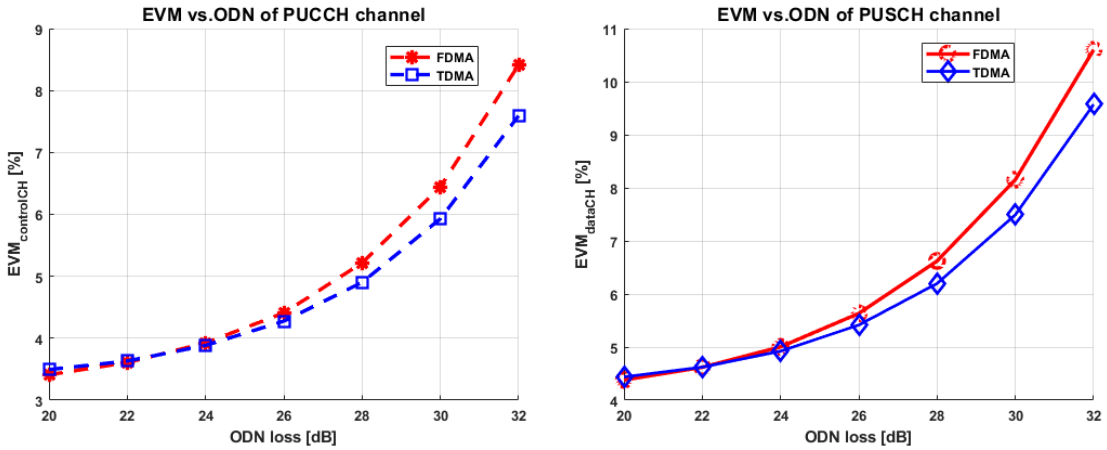

(a) PUCCH (b) PUSCH.

Figure 6.12: Mean EVM_F vs. ODN loss for 18 200-MHz NR channels at 12 dB clipping ratio.

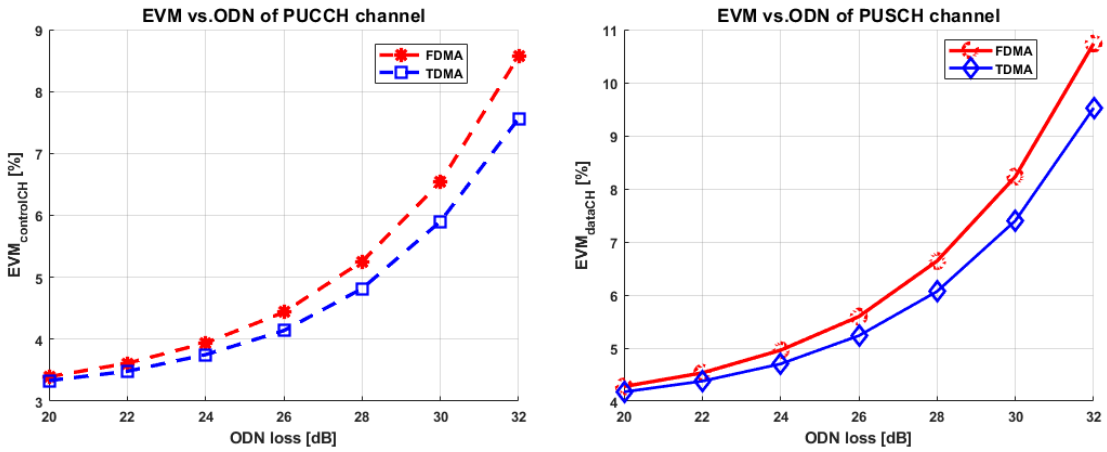

(a) PUCCH (b) PUSCH

Figure 6.13: Mean EVM_F vs. ODN loss for 9 400-MHz NR channels at 12 dB clipping ratio.

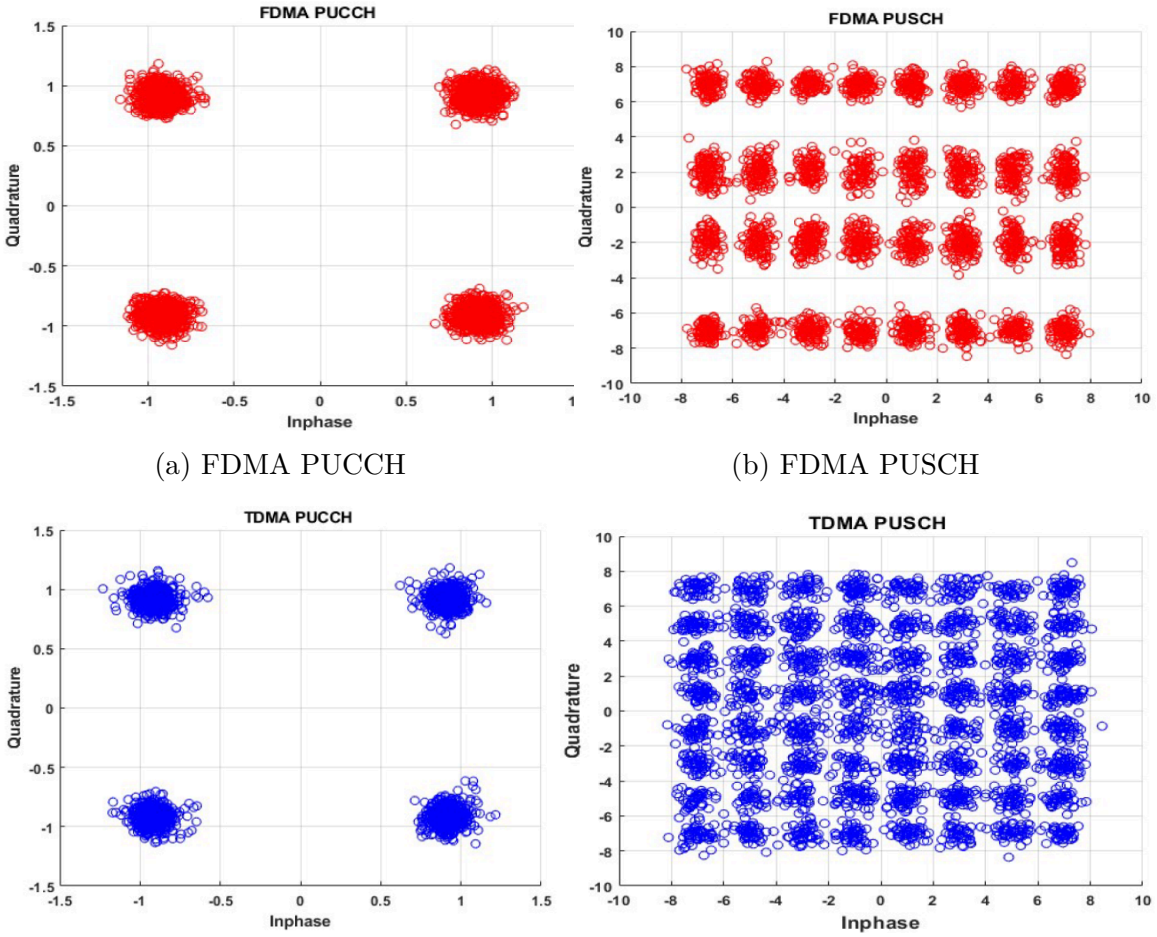

(a) FDMA PUCCH

(b) FDMA PUSCH

(c) TDMA PUCCH

(d) TDMA PUSCH

Figure 6.14: Decoded signal constellation on the ninth (last) 400 MHz-NR channel at 29 dB ODN loss .

Appendix A

Publications by the candidate

Journals

- **Befekadu D. Mengesha**, Pablo Torres-Ferrera and Roberto Gaudino, "Analysis of 5G New Radio Uplink Signals on an Analogue-RoF System Based on DSP-Assisted Channel Aggregation", In: *Appl. Sci.* 47 (Dec 2018), pp. 1-13.

  This paper is presented in Chapter 4 and 5.

- **Befekadu Mengesha**, Stefano Straullu, Pablo Torres-Ferrera and Roberto Gaudino, "Comparison of DSP-based TDMA and FDMA channel aggregation techniques in mobile fronthauling", In: *Optical Fiber Technology* 46 (Sep 2018), pp. 15-23.

  This paper is presented in Chapter 4 and 6.

Conference Proceedings

- **Befekadu D. Mengesha**, Pablo Torres-Ferrera and Roberto Gaudino, "DSP-assisted channel aggregation options for Next-Generation Mobile Fronthauling," In: *ICTON 2018; 20th International Conference on Transparent.* July 2018. pp. 1-4.

- S. Straullu, **M. Befekadu**, S. Abrate and R. Gaudino, "Optimization of DSP-based channel aggregation parameters for front-hauling over PON infrastructure", In: *2016 IEEE Photonics Conference (IPC).* Oct. 2016. pp. 1-3.

- **M. Befekadu**, S. Straullu, S. Abrate and Roberto Gaudino "Experimental Optimization of DSP-Aggregated Fronthauling Transmission for up to 4x96 LTE radio waveforms". In: *ECOC 2016; 42nd European Conference on Optical Communication.* Sept. 2016. pp. 929–931.

- **M. Befekadu**, S. Straullu, S. Abrate and Roberto Gaudino "Dimensioning the Physical Layer of DSP-Based Radio Waveforms Aggregation for Fronthauling". In: *18th Italian National Conferenceon Photonic Technologies (Fotonica 2016).*

Bibliography

[1] 3GPP. *3GPP TR 36.819 V11.1.0 - Coordinated multi-point operation for LTE physical layer aspects*. Tech. rep. Dec. 2011.

[2] 3GPP. *3GPP TS 36.104 V15.4.0: Technical Specification Group Radio Access Network; Evolved Universal Terrestrial Radio Access (E-UTRA); Base Station (BS) radio transmission and reception*. Tech. rep. Sept. 2018.

[3] 3GPP. *3GPP TS 36.201 V15.1.0 : Evolved Universal Terrestrial Radio Access Network (E-UTRAN); LTE physical layer; General description (Release 15)*. Tech. rep. June 2018.

[4] 3GPP. *3GPP TS 36.211 : Evolved Universal Terrestrial Radio Access Network (E-UTRAN); Physical channels and modulation (Release 15)*. Tech. rep. Sept. 2018.

[5] 3GPP. *3GPP TS 36.212 V15.3.0 : Evolved Universal Terrestrial Radio Access Network (E-UTRAN); Multiplexing and channel coding (Release 15)*. Tech. rep. Sept. 2018.

[6] 3GPP. *3GPP TS 36.213 V15.3.0 : Evolved Universal Terrestrial Radio Access Network (E-UTRAN); Physical layer procedures (Release 15)*. Tech. rep. Sept. 2018.

[7] 3GPP. *3GPP TS 36.420 version 15.0.0 : Evolved Universal Terrestrial Radio Access Network (E-UTRAN); X2 general aspects and principles (Release 15)*. Tech. rep. July 2018.

[8] 3GPP. *3GPP TS 36.420 version 15.0.0 :LTE; Evolved Universal Terrestrial Radio Access Network (E-UTRAN); S1 general aspects and principless (Release 15)*. Tech. rep. July 2018.

[9] 3GPP. *3GPP TS 38.101-1 V15.3.0 : 3rd Generation Partnership Project; Technical Specification Group Radio Access Network; NR; User Equipment (UE) radio transmission and reception; Part 1: Range 1 Standalone (Release 15))*. Tech. rep. Sept. 2018.

[10] 3GPP. *3GPP TS 38.104 V15.3.0 : 3rd Generation Partnership Project; Technical Specification Group Radio Access Network; NR; Base Station (BS) radio transmission and reception (Release 15)*. Tech. rep. Sept. 2018.

[11] 3GPP. *3GPP TS 38.211 V15.3.0 : 3rd Generation Partnership Project; Technical Specification Group Radio Access Network; NR; Physical channels and modulation (Release 15*. Tech. rep. Sept. 2018.

[12] 3GPP. *3GPP TS 38.212 V15.3.0 : 3rd Generation Partnership Project; Technical Specification Group Radio Access Network; NR; Multiplexing and channel coding (Release 15)*. Tech. rep. Sept. 2018.

[13] Govind P. Agrawal. "Lightwave technology: components and devices". In: *Wiley*. 2004.

[14] I. A. Alimi, A. L. Teixeira, and P. P. Monteiro. "Toward an Efficient C-RAN Optical Fronthaul for the Future Networks: A Tutorial on Technologies, Requirements, Challenges, and Solutions". In: *IEEE Communications Surveys Tutorials* 20.1 (2018), pp. 708–769. ISSN: 1553-877X. DOI: 10.1109/COMST.2017.2773462.

[15] IEEE Standard Association. *IEEE std 802.3 : IEEE Standard for Ethernet*. Tech. rep. Dec. 2012.

[16] G. Giannoulis ; N. Argyris ; N. Iliadis ; G. Poulopoulos ; K. Kanta ; D. Apostolopoulos ; H. Avramopoulos. "Analog Radio-over-Fiber Solutions for 5G Communications in the Beyond-CPRI Era". In: *2018 20th International Conference on Transparent Optical Networks (ICTON)*. 2018, pp. 1–5.

[17] M. Befekadu et al. "Dimensioning the Physical Layer of DSP-Based Radio Waveforms Aggregation for Fronthauling". In: *18th Italian National Conference on Photonic Technologies (Fotonica 2016)*. July 2016.

[18] M. Befekadu et al. "Experimental Optimization of DSP-Aggregated FronthaulingTransmission for up to 4x96 LTE radio waveforms". In: *ECOC 2016; 42nd European Conference on Optical Communication*. Sept. 2016, pp. 929–931.

[19] Federico Boccardi et al. "Five Disruptive Technology Directions for 5G". In: *IEEE Communications Magazine* 52.02 (Feb. 2014), pp. 74–80. ISSN: 0163-6804.

[20] J.-R. Burie et al. "Ultra high power, ultra low RIN up to 20 GHz 1.55 mum DFB AlGaInAsP laser for analog applications". In: *in Proceedings of SPIE - The International Society for Optical Engineering*. Feb. 2010.

[21] Andrew Che On Chan and Malin Premaratne. "Dispersion-Compensating Fiber Raman Amplifiers with Step, Parabolic, and Triangular Refractive Index Profiles". In: *Journal of Light Wave Technology* 25.05 (May 2007), pp. 1190–1197. ISSN: 0733-8724.

[22] Malhar Chauhan, Saurabh patel, and Hardik patel. "Different Techniques to Reduce the PAPR in OFDM System". In: *International Journal of Engineering Research and Applications (IJERA)* 02.03 (Mar. 2013), pp. 1292–1294. ISSN: 2248-9622.

[23] A. Checko et al. "Cloud RAN for Mobile Networks—A Technology Overview". In: *IEEE Communications Surveys Tutorials* 17.1 (Oct. 2015), pp. 405–426.

[24] T.R. Chen et al. "High power operation of InGaAsP/InP multiquantum well DFB lasers at 1.55 /spl mu/m wavelength". In: *Electronics Letters* 32.10 (May 1996), p. 898.

[25] Jung-Fu Cheng et al. "Analysis of Circular Buffer Rate Matching for LTE Turbo Code". In: *2008 IEEE 68th Vehicular Technology Conference*. Sept. 2008, pp. 1–5.

[26] Stanley Cheung, Stevan S. Djordjevic, and K. Okamoto. "Low-loss and High Contrast Silicon-on-Insulator (SOI) Arrayed Waveguide Grating". In: *Conference on Lasers and Electro-Optics*. May 2012.

[27] Stanley Cheung, Tiehui Su, and Katsunari Okamoto. "Ultra-Compact Silicon Photonic 512 × 512 25 GHz Arrayed Waveguide Grating Router". In: *IEEE Journal of selected tipics in Quantum Electronics* 20.04 (Aug. 2014). ISSN: 8202207.

[28] *Common Public Radio Interface (CPRI);Interface Specification 7.0, Oct. 2015*. http://www.cpri.info/downloads/CPRI_v_7_0_2015-10-09.pdf.

[29] Erik Dahlman, Stefan Parkvall, and Johan Sköld. "4G LTE/LTE-Advanced for Mobile Broadband". In: *AP publishing*. 2011.

[30] Erik Dahlman, Stefan Parkvall, and Johan Sköld. "5G NR: The Next Generation Wireless Access Technology". In: *AP publishing*. 2018.

[31] Dahlman et al. "3G Radio Access Evolution—HSPA and LTE for Mobile Broadband". In: *IEICE transactions on communications* 92.5 (2009), pp. 1432–1440.

[32] T. A. Diallo et al. "Jitter impact on mobile fronthaul links". In: *Optical Society of America*. 2014, W2A.41.

[33] Uwe Dötsch et al. "Quantitative Analysis of Split Base Station Processing and Determination of Advantageous Architectures for LTE". In: *Nokia Bell Labs Journal* 18.1 (2013), pp. 105–128.

[34] Uwe Dötsch et al. "Quantitative analysis of split base station processing and determination of advantageous architectures for LTE". In: *Journal of Lightwave Technology* 18.1 (June 2013), pp. 105–128. ISSN: 1538-7305.

[35] Vincenzo Eramo et al. "Dimensioning Models of Optical WDM Rings in Xhaul Access Architectures for the Transport of Ethernet/CPRI Traffic". In: *applied sciences* 8.612 (Apr. 2018), pp. 1–16. ISSN: app8040612.

[36] Vincenzo Eramo et al. "Performance Evaluation of Integrated OTN/WDM Metropolitan Networks in Static and Dynamic Traffic Scenarios". In: *Journal of Optical Communications and Networking* 7.8 (Aug. 2015), pp. 761–775. ISSN: Eramo et al.

[37] Mickaël Faugeron et al. "High-Power, Low RIN 1.55 mu/m Directly Modulated DFB Lasers for Analog Signal Transmission". In: *IEEE Photonics Technology Letters* 24.02 (Jan. 2012), pp. 116–118. ISSN: 1041–1135.

[38] FS.com. *Basics of Fiber Optic Attenuator*. https://www.fs.com/basics-of-fiber-optic-attenuator-aid-344.html.

[39] Robert G.Gallager. "Low-Density-Parity-Check-Codes". In: *M.I.T press* (July 1963).

[40] M. GEHL et al. "Active phase correction of high resolution silicon photonic arrayed waveguide gratings". In: *Optics Expess* 25.06 (Mar. 2017), pp. 6320–6334. ISSN: 130.7408.

[41] A. Ghosh and R. Ratasuk. "Essentials of LTE and LTE-A". In: *Cambridge University Press*. 2011.

[42] H.K.Shankarananda, Shreyas S S, and Guruprasad B. "External Modulators and Mathematical Modeling of MachZehnder Modulator". In: *International Journal of Innovative Science, Engineering and Technology* 03.12 (Dec. 2016), pp. 214–220. ISSN: 2348 – 7968.

[43] Nagib z. Hakim, Bahaa E. A. Saleh, and Malvin C. "Signal-to-Noise Ratio for Lightwave Systems Using Avalanche Photodiodes". In: *Journal of Light Wave Technology* 09.03 (Jan. 1991), pp. 318–320. ISSN: 0733-8724.

[44] Fatemeh Hamidi-Sepehr, Ajit Nimbalker, and Gregory Ermolaev. "Analysis of 5G LDPC Codes Rate-matching Design". In: *2018 IEEE 87th Vehicular Technology Conference (VTC Spring)*. Sept. 2018, pp. 1–5.

[45] J. Hoydis, S. ten Brink, and M. Debbah. "Massive MIMO in the UL/DL of Cellular Networks: How Many Antennas Do We Need?" In: *IEEE Journal on Selected Areas in Communications* 31.2 (Feb. 2013), pp. 160–171.

[46] Steve Hranilovic and Frank R. Kschischang. "Optical Intensity-Modulated Direct Detection Channels: Signal Space and Lattice Codes". In: *IEEE Transaction on INformation Theory* 49.6 (June 2003), pp. 1385–1399. ISSN: 0018-9448/03.

[47] Xiaofeng Hu, Chenhui Ye, and Kaibin Zhang. "Converged mobile fronthaul and passive optical network based on hybrid analog-digital transmission scheme". In: *2016 Optical Fiber Communications Conference and Exhibition (OFC)*. 2016, pp. 1–3.

[48] FiberLabs Inc. *Erbium-Doped Fiber Amplifier (EDFA)*. https://www.fiberlabs.com/glossary/erbium-doped-fiber-amplifier/.

[49] VOXTEL inc. *TECHNICAL NOTE: V803: Avalanche Photodiode Receiver Performance Metrics*. Tech. rep.

[50] China Mobile Research Institute. *c-RAN : The road towards green RAN*. Tech. rep. Oct. 2011.

[51] China Mobile Research Institute et al. *White Paper of Next Generation Fronthaul Interface*. Tech. rep. June 2015.

[52] ITU-R. *IMT Vision – Framework and overall objectives of the future development of IMT for 2020 and beyond*. Tech. rep. Sept. 2015.

[53] ITU-R. *Recommendation ITU-R M.2083-0 : IMT Vision – Framework and overall objectives of the future development of IMT for 2020 and beyond*. Tech. rep. Sept. 2015.

[54] ITU-T. *Characteristics of a single-mode optical fibre and cable : Recommendation ITU-T G.652*. Tech. rep. Nov. 2016.

[55] ITU-T. *G.987.2 : 10-Gigabit-capable passive optical networks (XG-PON): Physical media dependent (PMD) layer specification*. Tech. rep. Feb. 2016.

[56] Preetam Jain and Lochan Jolly. "Comparative Study of an Optical Link with PIN and APD as Photo-Detector". In: *International Journal of Application or Innovation in Engineering and Management (IJAIEM)* 03.08 (Aug. 2014), pp. 85–91. ISSN: 2319 - 4847.

[57] S. Janz et al. "Planar Waveguide Echelle Gratings in Silica-On-Silicon". In: *IEEE Photonics Technology Letters* 16.02 (Aug. 2014), pp. 503–505. ISSN: JANZ et al.,

[58] Jeongho Jeon. "NR Wide Bandwidth Operations". In: *IEEE Communications Magazine* 56.3 (Mar. 2018), pp. 42–46. ISSN: 0163-6804.

[59] Jeongho Jeon. "NR Wide Bandwidth Operations". In: *IEEE Communications Magazine* 56.03 (Mar. 2018), pp. 42–46. ISSN: 1558-1896.

[60] Douglas L. Jones. *Fronthaul transport for virtualized small cells*. http://scf.io/en/documents/169_-_Fronthaul_transport_for_virtualized_small_cells.php.

[61] Douglas L. Jones. *Multirate Signal Processing*. file:///C:/Users/befekadum/Downloads/multirate-signal-processing-1.4.pdf.

[62] G. Kardaras and C. Lanzani. "Advanced multimode radio for wireless and mobile broadband communication". In: *2009 European Wireless Technology Conference*. Sept. 2009, pp. 132–135.

[63] G. Kardaras et al. "Fiber to the antenna: A step towards multimode radio architectures for 4G mobile broadband communications". In: *2010 IEEE 4th International Symposium on Advanced Networks and Telecommunication Systems*. Dec. 2010, pp. 85–87.

[64] L.Hanzo et al. "OFDMA and MC-CDMA for Broadband Multi-User Communications, WLANs and Broadcasting". In: *John Wiley and Sons, Ltd.* 2003.

[65] Shangyuan Li et al. "Highly Linear Radio-Over-Fiber System Incorporating a Single-Drive Dual-Parallel Mach–Zehnder Modulator". In: *IEEE Photonics Technology Letters* 22.24 (Dec. 2010), pp. 503–505. ISSN: 1775-1777.

[66] Xiaodong Li and L.J. Cimini. "Effects of clipping and filtering on the performance of OFDM". In: *IEEE Communications Letters* 02.05 (May 1998), pp. 1634–1638. ISSN: 1558-255.

[67] Y. Lin et al. "Wireless network cloud: Architecture and system requirements". In: *IBM Journal of Research and Development* 54.1 (Jan. 2010), 4:1–4:12. ISSN: 0018-8646.

[68] Xiang Liu et al. "CPRI-compatible efficient mobile fronthaul transmission via equalized TDMA achieving 256 Gb/s CPRI-equivalent data rate in a single 10-GHz-bandwidth IM-DD channel". In: *2016 Optical Fiber Communications Conference and Exhibition (OFC)*. Aug. 2016, pp. 1–5.

[69] Xiang Liu et al. "Efficient Mobile Fronthaul via DSP-Based Channel Aggregation". In: *Journal of Lightwave Technology* 34.06 (Mar. 2016), pp. 1556–1564. ISSN: 0733-8724.

[70] Garima Malik and Amandeep Singh Sappal. "Adaptive Equalization Algorithms:An Overview". In: *International Journal of Advanced Computer Science and Applications(IJACSA)* 02.03 (Mar. 2011), pp. 62–67.

[71] Andrea Matera and Umberto Spagnolini. "On the Optimal Space-Frequency to Frequency Mapping in Indoor Single-Pair RoC Fronthaul". In: *2017 European Conference on Networks and Communications (EuCNC)*. July 2017.

[72] R.J. Mears et al. "Low-noise erbium-doped fibre amplifier operating at 1.54mum". In: *Electronics Letters* 23.10 (Sept. 1987), pp. 1026–1028. ISSN: 0013-5194.

[73] Befekadu Mengesha, Pablo Torres-Ferreraa, and Roberto Gaudinoa. "Analysis of 5G New Radio Uplink Signals on an Analogue-RoF System Based on DSP-Assisted Channel Aggregation". In: *Appl. Sci.* 47 (2019), pp. 1–13.

[74] Befekadu Mengesha et al. “Comparison of DSP-based TDMA and FDMA channel aggregation techniques in mobile fronthauling”. In: *Optical Fiber Technology* 46 (Sept. 2018), pp. 15–23. ISSN: B. Mengesha et al.

[75] Paulo Monteiro and Atilio Gameiro. “Chapter : Convergence of Optical and Wireless Technologies for 5G: A Research and Development Perspective”. In: *Opportunities in 5G Networks*. Apr. 2016, pp. 179–215.

[76] M. Nahas et al. “Base stations evolution: Toward 4G technology”. In: *2012 19th International Conference on Telecommunications (ICT)*. Apr. 2012, pp. 1–6.

[77] Yrjo Newo, Dong Cheng-Yu, and Sanjit K. Mitra. “Interpolated Finite Impulse Response Filters”. In: *IEEE Transaction on Acoustic, Speech, and signal processing* ASSP-32.03 (June 1984), pp. 563–570. ISSN: 0096-3518.

[78] Greed Octken, Thomas W. Parks, and Hans W. Schussler. “New Results in the Design of Digital Interpolators”. In: *IEEE Transaction on Acoustic, Speech, and signal processing* ASSP-23.03 (June 1975), pp. 301–309.

[79] Antonio de la Oliva ; Jose Alberto Hernandez ; David Larrabeiti ; Arturo Azcorra. “An overview of the CPRI specification and its application to C-RAN-based LTE scenarios”. In: *IEEE Communications Magazine* 54.2 (Feb. 2016), pp. 152–159. ISSN: 1558-1896.

[80] O Omomukuyo, M P Thakurand, and J E Mitchell. “Experimental Demonstration of the Impact of MZM Non-Linearity on Direct-Detection Optical OFDM”. In: *Workshop on Hybrid Optical Wireless Access Networks*. 2012.

[81] *Open Base Statio Architecture Initiative (OBSAI) BTS system reference document Version 2.0,2006*. http://www.obsai.com/specs/OBSAI_System_Spec_V2.0.pdf.

[82] *Open Radio equipment Interface (ORI); ORI Interface Specification;Part 1: Low Layers (Release 1)*. https://www.etsi.org/deliver/etsi_gs/ORI/001_099/00201/04.01.01_60/gs_ORI00201v040101p.pdf.

[83] OMEGA optical. *Optical filter design : Application note*. http://www.glenspectra.co.uk/glen/filters/product/oem_guide.pdf.

[84] J. Palicot, H. Zhang, and C. Moy. “On the road towards green radio”. In: *URSI Radio Science Bulletin* 2013.347 (Dec. 2013), pp. 40–56. ISSN: 1024-4530.

[85] Qi Pan and R.J. Green. “Bit-error-rate performance of lightwave hybrid AM/OFDM systems with comparison with AM/QAM systems in the presence of clipping impulse noise”. In: *IEEE Photonics Technology Letters* 08.02 (Dec. 1996), pp. 278–280.

[86] A. Pizzinat et al. “Things You Should Know About Fronthaul”. In: *Journal of Lightwave Technology* 33.5 (Mar. 2015), pp. 1077–1083.

[87] Chathurika Ranaweera et al. “5G C-RAN architecture: A comparison of multiple optical fronthaul networks”. In: *2017 International Conference on Optical Network Design and Modeling (ONDM)*. 2017, pp. 1–6.

[88] Tom Richardson and Shrinivas Kudekar. “Design of Low-Density Parity Check Codes for 5G New Radio”. In: *IEEE Communications Magazine* 56.3 (Mar. 2018), pp. 28–34. ISSN: 0163-6804.

[89] Christian B. Schlegel and Lance C. Pe´rez. “TRELLIS AND TURBO CODING”. In: *IEEE PRESS*. 2004.

[90] Timothy M. Schmidl and Donald C. Cox. “Robust Frequency and Timing Synchronization for OFDM”. In: *IEEE Transaction on Communications* 45.12 (Dec. 1997), pp. 1613–1621. ISSN: 0090–6778.

[91] Rene Schmogrow et al. “Error Vector Magnitude as a Performance Measure for Advanced Modulation Formats”. In: *IEEE Photonocs Technology Letters* 24.1 (Jan. 2012), pp. 61–63. ISSN: SCHMOGROWetal.

[92] Rishad Ahmed Shafik, Md. Shahriar Rahman, and AHM Razibul Islam. “On the Extended Relationships Among EVM, BER and SNR as Performance Metrics”. In: *4th International Conference on Electrical and Computer Engineering(ICECE)*. Dec. 2006, pp. 408–411.

[93] Saumil S. Shah and Atit R. Patel. *LTE- single carrier frequency division multiple acess DIVISION MULTIPLE ACCESS*. https://cdn.eeweb.com/projects/member-projects/LTE_SCFDMA-1-1299882900_180111_090526.pdf.

[94] William Shieh and Ivam Djordsevic. “Orthogonal Frequency Division Multiplexing for Optical Communications”. In: *AP publishing*. 2010, pp. 978-0-12-374879–9.

[95] Bernard Sklar. “Digital Communications Fundamentals and Applications Second Edition”. In: *Prentice Hall P T R*.

[96] F. M. Soares et al. “Monolithically Integrated InP Wafer-Scale 100-Channel × 10-GHz AWG and Michelson Interferometers for 1-THz-Bandwidth Optical Arbitrary Waveform Generation”. In: *Optical Fiber Communication Conference/National Fiber Optic Engineers Conference*. May 2010.

[97] Shayan G. Srinivasa and Anthony Weathers. “An Efficient On-the-Fly Encoding Algorithm for Binary and Finite Field LDPC Codes”. In: *IEEE Communications Letters* 13.11 (Nov. 2009), pp. 853–855. ISSN: 1558-2558.

[98] Wipro Technologies. *Software-Defined Radio White Paper*. Tech. rep. Aug. 2002.

[99] Pablo Torres-Ferrera et al. "Upstream and Downstream Analysis of an Optical Fronthaul System Based on DSP-Assisted Channel Aggregation". In: *J. Opt. Commun.Netw.* 09.12 (Dec. 2017), pp. 1191–1201. ISSN: Torres-Ferrera et al.

[100] International Telecommunication Union-ITU. *Series G: Transmissin and media, digital systems and networks-Radio-over-fiber(RoF) technologies and their applications*. Tech. rep. June 2015.

[101] Mikko Valkama. *Complex-valued signals and systems-Basic principles and application to radio communications and radio signal processing*. http://www.cs.tut.fi/kurssit/TLT-9707/presentations/Complex-Signals-and-Radios-short-2pp.pdf.

[102] Herbert Venghaus. "Wavelength Filters in Fibre Optics". In: *Springer*. 2006.

[103] David Wake, Anthony Nkansah, and Nathan J. Gomes. "Radio Over Fiber Link Design for Next Generation Wireless Systems". In: *Journal of Lightwave Technology* 28.16 (Aug. 2010), pp. 108–113. ISSN: 2456-2464.

[104] Jing Wang et al. "Digital Mobile Fronthaul Based on Delta–Sigma Modulation for 32 LTE Carrier Aggregation and FBMC Signals". In: *IEEE Communications and Networking* 09.2 (Feb. 2017), A233–A244. ISSN: Wang et al.

[105] SuHyun Wang. *Cisco Visual Networking Index (VNI) and VNI Service Adoption - Global Forecast Update, 2016–2021*. Tech. rep. June 2012.

[106] Wei-Chih Wang. *Optical sources*. http://depts.washington.edu/mictech/optics/sensors/light_source.pdf.

[107] Yuanquan Wang, Jianjun Yu, and Nan Chi. "Demonstration of 4 X128-Gb/s DFT-S OFDM Signal Transmission over 320-km SMF With IM/DD". In: *IEEE Photonics Journal* 8.2 (Apr. 2016). ISSN: 1943-0655.

[108] S. Weinstein and P. Ebert. "Data Transmission by Frequency-Division Multiplexing Using the Discrete Fourier Transform". In: *IEEE Transactions on Communication Technology* 19.05 (Oct. 1971), pp. 628–634. ISSN: Weinstein and Ebert.

[109] Chenhui Ye et al. "A DSP-Assisted Symbol-Cascade Mobile Fronthaul Solution with Large Capacity and Neat RRHsl". In: *2015 European Conference on Optical Communication (ECOC)*. 2016, pp. 1–3.

[110] Houman Zarrinkoub. "Understanding LTE with MATLAB : fom mathematical modeling to simulation and prototyping". In: *John Wiley and Sons, Ltd.* 2014.

[111] Shidong Zhou et al. “Distributed Wireless Communication System: A New Architecture for Future Public Wireless Access”. In: *IEEE Communications Magazine* 41.3 (Mar. 2003), pp. 108–113. ISSN: 1558-1896.

[112] Siyu Zhou et al. “Low-Latency High-Efficiency Mobile Fronthaul With TDM-PON (Mobile-PON)”. In: *IEEE Communications and Networking* 10.1 (Jan. 2018), A10–A26. ISSN: Zhou et al.

This Ph.D. thesis has been typeset by means of the TEX-system facilities. The typesetting engine was pdfLATEX. The document class was `toptesi`, by Claudio Beccari, with option `tipotesi=scudo`. This class is available in every up-to-date and complete TEX-system installation.